Ph.D. Dissertation:

Flow Patterns Causing Saddle Instability in the Performance Curve of a Centrifugal Pump with Vaned Diffuser

By

YANG Jun

Supervised by

Prof. PAVESI Giorgio Prof. YUAN Shouqi

Doctoral course: Energetic

Dept. of Industrial Engineering, University of Padua, Italy

National Research Center of Pumps, Jiangsu University, China

February 2015

Abstract

In the present study, a reduced scale model of a low-pressure stage of a two-stage pump turbine was investigated when it operates in pump mode, which is as a centrifugal pump with vaned diffuser. An instability region was found in its *Q-H* curve. This instability region, centered into the flow rate interval between 0.45 to 0.7 Q_{Des}, restricts the stable operating range of the test pump.

The object of this study was to analyze the origins and development of the unsteadiness inner pump during this saddle instability region, and to find the causes of this saddle, which could guide the design, and optimization of the test pump.

Experimental and numerical approaches have been adopted to contribute the understanding on the highly complex flow interactions inside the test pump. The analyses pointed out that the instability of *Q-H* curve during this flow rate interval was mainly affected by the flow field unsteadiness into the diffuser. Severe flow separation occurred into the diffuser, affecting and/or affected by the unsteadiness from the impeller and return channel remarkably.

Both at full and part load, due to the U shape stay vanes in the return system, a 3-dimentional complex flow was found on the suction side of stay vane near the U turn corner. This flow caused a periodic unforced pressure disturbance with frequency St=0.6625 in the diffuser. A rotating stall with 5 cells into the diffuser was also highlighted by the experimental analyses and the numerical results validated that this disturbance was mainly due to the unsteady flow patterns in the return channel.

With the reduction of flow rate, the location of this unsteadiness in return channel move closer to the outlet of diffuser, and the unsteadiness made the flow separation near the stay vane leading edge on the suction side more severe and it impacted the flow in diffuser flow field in a more severe way.

At the same time, two types of unsteadiness were detected in the impeller in the saddle instability region. They were the flow separation with the frequency St=0.6625 at the impeller blade suction side and the wake-jet near the trailing edge of impeller blade with the frequency St=0.335, respectively. The wake-jet caused a periodic disturbance with a frequency of St=0.335 in diffuser as well. The experimental results indicated that it propagate circumferentially with 2 cells.

At the beginning of this saddle instability, in diffuser, the intensity of the fluctuations at St=0.335 and St=0.6625 both increase with the falling flow rate. With the development of these unsteady patterns, they mixed and caused a blockage in the gap between impeller and diffuser. This blockage caused the increase of the amplitude at BPF, which has been detected both by experimental and numerical results. At the same time, the further development of the blockage weakened the intensity of the two disturbances with frequency of St=0.335 and St=0.6625 in the blockage region. The blockage fully developed near the critical flow rate of 0.6 Q_{Des}. At this condition, the intensity of rotor and stator interaction increased and energy loss also increased which caused the drop of head and mean pressure at the exit of impeller. Furthermore, the disturbance in diffuser which caused by wake-jet of impeller lost the periodic character with frequency of St=0.335 at this condition. This is the reason why the non-linear component St=0.335 disappeared in diffuser around 0.6 Q_{Des}.

Key words: Centrifugal pump with vaned diffuser, saddle instability, unforced unsteadiness, numerical simulation, experiment

摘要

对于目前常用的水泵水轮机，在水轮机工作模式及泵工作模式下稳定高效安全的运行范围是制约其发展的关键技术之一。在泵工作模式下，水泵水轮机可视作为一带导叶的离心泵，小流量非定常流动和大流量空化是制约其稳定运行范围的主要因素。

本文以一等比例缩小的两级水泵水轮机低压级为模型，通过试验性能曲线分析表明：在小于设计点流量运行时，模型泵的性能曲线分别在两个流量区间出现驼峰现象：0.45 到 0.70 倍设计流量和小于 0.4 倍设计流量。其中，0.45 到 0.70 倍设计流量区间内的驼峰直接制约了模型泵的稳定运行范围。因此，为了优化泵的稳定运行范围，本文通过试验和数值模拟方法研究该流量区间内非定常流动的发生、发展规律及其对模型泵特性曲线驼峰的影响。

研究中首次采用频域分析法、连续小波变换分析法及高阶谱分析法相结合的方法，对离心泵内部动态压力信号进行分析，实现了基于动态压力信号诊断泵内非定常流动特征的目的。同时，考虑前后泵腔流动对流场的影响，将基于实验测得的不同流量下前后泵腔的泄漏量作为数值模拟的边界条件。研究表明，该数值模拟方法对离心泵内不稳定流场的预测具有较高的准确性，其结果能为该驼峰流量范围内的不稳定扰动发生、发展规律提供有价值的信息。并基于所提出的分析及研究方法，发现了引起 0.45 到 0.70 倍设计流量区间内驼峰的主要非定常流动结构，为优化泵的稳定运行范围提供有力的理论基础。

本文试验研究主要包括：改造开式水泵水轮机试验台，使其适用于带导叶离心泵内部非定常流动的试验研究，并基于Labview和Matlab编写完成带导叶离心泵性能和瞬态压力特性的测量及后处理分析系统。该系统用于泵性能参数与压力信号的同步采集及时域、频域分析。同时，本文采用高压气泡作为流道内部非定常流动的示踪媒介，通过高速摄影仪拍摄示踪气泡在导叶流道内的非定常流动轨迹，定性分析了不同流量下导叶流道内的非定常流动特征。

此外，本文借助数值模拟方法对模型泵该驼峰流量区间的流动进行了分析，对流场和流动诱导产生的声场开展数值预测。在采用高质量结构化网格进行计算的同时，加载前后泵腔泄漏量作为边界条件，在ANSYS-CFX中对流场进行计算，

并基于Lighthill声比拟理论，应用ANSYS-CFX与LMS Virtual. Lab Acoustics混合求解法，计算了流场中偶极子声源在各特征频率下的强度分布。

通过试验及数值模拟结果的对比分析，本文发现所研究的带导叶离心泵内部非定常流动具有以下发生、发展规律：

（1）由于所研究模型泵采用了固定导叶的U型结构，即使在设计流量下，固定导叶前半部分的吸力面附近也会出现复杂的三维非定常流动，并包含多种不同周期的扰动。除了由动静干涉引起的周期性受迫扰动，该非定常流动中特征频率为St=0.6625，非受迫周期性扰动的作用也较为明显。

（2）随着流量进入所研究的驼峰流量区，叶轮各流道内部开始出现相似的非定常流动结构，包括：各叶片吸力面喉部附近出现的周期频率为St=0.6625的流动分离，各叶片尾缘的射流尾迹作用（周期频率为St=0.335），以及叶轮进口前缘在靠近前盖板附近出现的周期性非定常流动。

（3）对于带二级反导叶模型泵性能曲线在0.45到0.7倍设计流量区间内出现的驼峰主要是由可调导叶进口及叶轮与可调导叶间隙内的非定常流动引起的。0.70倍设计流量到驼峰拐点0.6倍设计流量附近，可调导叶内流动除了动静干涉引起的受迫扰动外，还有另外两个显著的周期性不稳定扰动（St=0.6625和St=0.335）。其中，特征频率为St=0.335的压力扰动源于叶轮尾缘的射流尾迹作用，主要引起导叶进口的流动分离，沿周向传播有2个核；周期频率为St=0.6625的压力扰动沿周向传播有5个核，主要源于固定导叶前半部分吸力面附近的非定常流动结构，随着流量的减小，其作用加剧，与动静干涉的共同作用引起可调导叶后吸力面尾缘附近的旋转失速。以上两种非定常流动皆在近前泵腔附近的作用最强。

（4）这两种流动在可调导叶吸力面喉部附近出现混合相互作用，并在近前盖板附近的径向截面上叶轮导叶间隙出现局部堵塞现象。当流量继续减小，在驼峰拐点流量附近（0.584倍设计流量），叶轮与导叶的间隙及流道内局部堵塞加剧，引起St=0.335突然消失，St=0.6625开始逐渐减弱。

关键词：带导叶离心泵，驼峰，非受迫扰动，数值模拟，试验

Riassunto

Il campo di moto all'interno di uno stadio a bassa pressione di una macchina reversibile pompa-turbina bistadio è stato analizzato in dettaglio nel funzionamento da pompa. E' stato identificata una regione di instabilità funzionale centrata in un intervallo di portata comprese fra 0,45-,7 Q_{Des}, che limita il campo di funzionamento della turbomacchina sotto test.

Le origini, lo sviluppo e la dinamica delle instabilità che si ingenerano all'interno di questo campo di esercizio sono state analizzate per cercare di identificare le cause della caduta di prevalenza e poter guidare successivamente la progettazione e l'ottimizzazione della pompa di prova.

Approcci sperimentali e numerici sono state adottati per contribuire alla comprensione delle interazioni di flusso estremamente complessi all'interno della pompa di prova. Le analisi hanno evidenziato che l'instabilità della curva *Q-H* in questo intervallo di portate è principalmente conseguente all'instabilità campo di flusso nel diffusore. Separazioni marcate si verificano nel diffusore, conseguenza o amplificate dalla instabilità della girante o dei canale di ritorno.

Nei canali di ritorno, sia a pieno carico che ai carichi parziali, è stato riscontrato una zona di ricircolo in prossimità del gomito e vicino alla superficie in depressione. Questo ricircolo causa un disturbo con frequenza St = 0,6625 nel diffusore. Nella zona di instabilità alla stessa frequenza è stato individuato uno stallo rotante con 5 celle nel diffusore sia dalle analisi sperimentali che dai risultati numerici.

Al ridursi della portata, la posizione di questa instabilità nel canale di ritorno trasla verso la sezione di uscita del diffusore rendendo il campo di moto nel diffusore più instabile.

Per queste portate sono state identificate due sorgenti di instabilità nella girante. La prima con la frequenza St = 0,6625 sul lato in depressione delle pale e il secondo nella zona di jet vicino alla sezione di uscita della girante con la frequenza St = 0,335. La zona di jet causa anche un disturbo periodico con una frequenza di St = 0,335 nel diffusore. I risultati sperimentali hanno evidenziato che questa instabilità genera una pulsazione di pressione con 2 cellule.

In corrispondenza della zona di instabilità, l'intensità delle fluttuazioni a St = 0,335 e St = 0,6625 aumenta al diminuire della portata. Contemporaneamente ampie zone del traferro tra girante e diffusore risultano bloccate. Questo blocco causa un'amplificazione delle pulsazioni alla frequenza di passaggio delle pale BPF rilevato sia da risultati sperimentali che numerici. Allo stesso tempo, l'ulteriore sviluppo del blocco indebolito l'intensità delle due fluttuazioni

di pressioni a frequenza di St = 0,335 e St = 0,6625. Tale sviluppo raggiunge l'apice per una portata di circa 0,6 Q_{Des}. A questa condizione, l'intensità dell'interazione rotore e statore aumentata e la perdita di energia aumentata causando la caduta di prevalenza all'uscita della girante. Inoltre, l'instabilità nel diffusore perde il suo carattere periodico con frequenza di St = 0,335.

Parole chiave: Pompa Centrifuga, Diffusore Palettato, Instabilità Funzionale, Pulsazioni di Pressione, Simulazione numerica, esperimento

Contents

I Introduction

Chapter 1 Introduction

1.1 Pumped-Storage Hydroelectricity

Pumped storage hydroelectricity (PSH) as a type of Hydro power generation is widely used by many power plants for load balancing. It is the only economic and flexible means of storing grid scale amounts of excess energy, which allows power plants dispatchers to successfully manage that balancing act(Yang , et al. 2001, He , et al.2006).

The advantage of PSH is that it can come online very quickly, making it a useful tool to balance the varying electricity demand from consumers or unplanned outages from other power plants. Fig. 1.1 shows the power distribution over a day of a PSH facility, the compensation is achieved by storing energy during base-load phases (green region) while making this energy available to the grid for peaking supply needs and system regulation (red region).

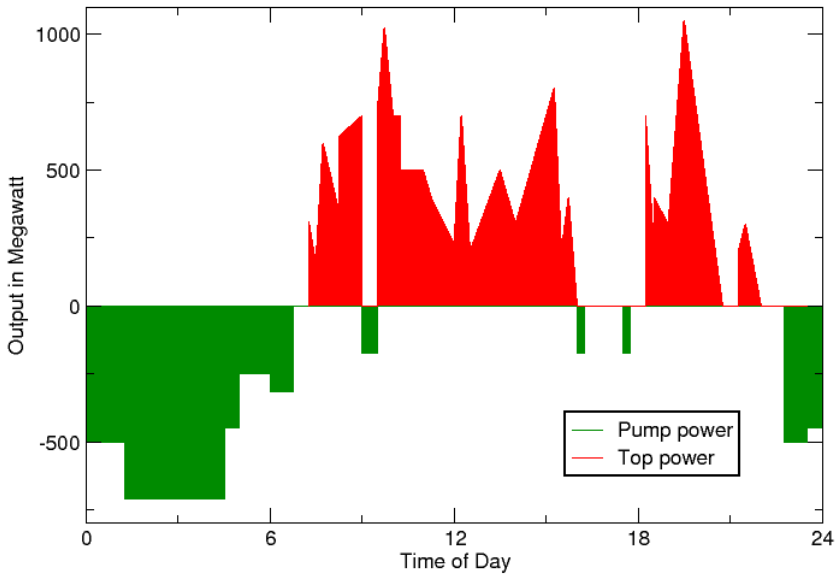

Fig. 1.1 Power spectrum of pump-storage hydroelectricity

The principle behind the operation of PSH is shown in Fig. 1.2. When there is a surplus of power in the network, the pumped storage power station switches to pumping mode (see Fig. 1.2(a)): the power grid input power to the electric motor to

drive a pump or pump turbine, which pumps water from a lower reservoir to a higher storage basin. While the demand for electricity in the grid rises, the water is released from the upper basin via a pressure pipeline (see Fig. 1.2(b)). The water causes the turbine or pump turbine to move. The pump now operates in turbine mode and is used in turn to drive the generators. Within seconds, electricity is generated and fed into the electricity network.

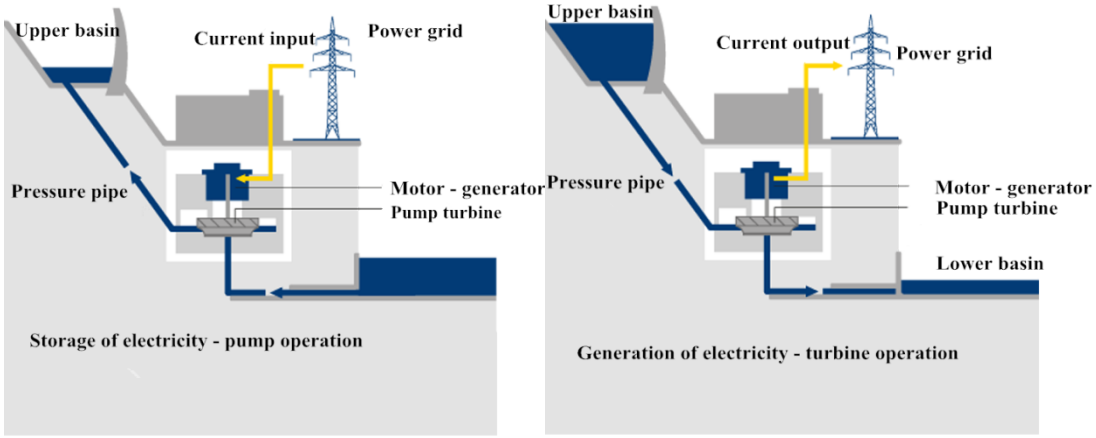

(a) Pump operation (b) Turbine operation

Fig. 1.2 Storage and generation of electricity by pumped storage hydroelectricity

The world's oldest pump-storage scheme is the Lettern Station of the Zurich electricity works, which dates from 1890. Today, the pumped storage, as one of the most important energy storages, is the largest-capacity form of grid energy storage available. Until March 2012, the Electric Power Research Institute of U.S. (EPRI) reported that PSH accounts for more than 99% of bulk storage capacity worldwide, representing around 127,000 MW(Mar 3rd 2012). The energy efficiency of PSH varies in practice between 70% and 80%(Levine 2007, Yang 2012, Jacob 2013, Economist Mar 3rd 2012) with some claiming up to 87%.

For the requirements of environmental sustainability, more and more countries around the globe are ramping up their power generation from new renewable energy sources such as wind and solar power, which start to become a larger piece of the national energy mixture.

For wind and solar, although the generation of power is very huge, it is subject to the strong natural fluctuations. They cannot always provide electricity in the required amounts or at the desired time. Excess energy thus needs to be stored so that it can be made available at any time. Therefore, managing the balance between new renewable energy production and consumption has become an issue of growing importance in order to guarantee the stability of electrical networks. With the current state of technology, there is only one possibility for achieving this goal in an economically

viable, large-scale way: with the help of pumped storage plants. This means that the demand for pumped storage power plants will continue to grow worldwide.

1.2 Reversible Pump Turbine

For the pumped storage technology, it can be realized by a reversible pump-turbine, or a turbine and pump combination. Reversible pump turbine can, depending on reservoir size, deliver long term energy storage, and is able to boost production (turbine) or consumption (pump) in peak power situations. As a typical kind of pumped storage plants equipment, it is widely applied, which is regarded as the most cost effective solution, even if there are also other technical arrangements such as the combinations Francis turbine/pump or Pelton turbine/pump.

For the variable requirements of energy production and consumption, a wide head range is desired for modern pump turbine operation. The reversible pump turbine in pump mode could be seen as a centrifugal pump with vaned diffuser. In order to get a wider stable head range, the performance curve instabilities or sudden deviation from the expected smooth performance curves should be avoided. Figure 1.3 shows a typical performance curve of a centrifugal pump with vaned diffuser, the commonly requirements for the range is that Hmax/Hmin>1.5. It is indicated that the low head cavitations and high head instabilities curb the stable range of operation. OP1 is working on the stable head range. With the reduction of flow rate, the head becomes unstable at OP2, and a saddle shape with hysteresis appears in this region. With the growing specific speed, the risk of a saddle-shaped instability increases. The flow rate, where the *Q-H*-curve becomes instable, moves much closer to the design point. Typically a type of instability occurs at Q/Q_{Des} = 0.6 to 0.9. Therefore, this type of instability is also sometimes called “full load instability”. These instabilities seriously restrict the wider stable operating range of pump (Hergt and Starke 1985, Gülich 2010).

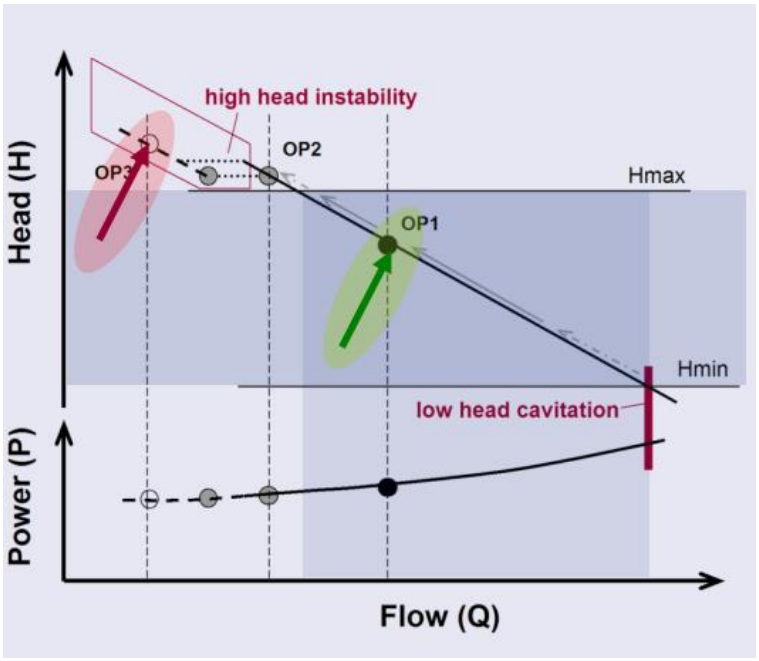

Fig. 1.3 The performance curve of a centrifugal pump with vaned diffuser

1.3 Instabilities in the Performance Curves at Partload Operation

A pump, which is working significantly below the best efficiency flow rate is said to operate at part load. For low specific speeds this can be roughly assumed at $Q/Q_{Des}<0.8$ and $Q/Q_{Des}<0.9$ for high specific speeds. The flow becomes highly 3-demensional separates in the impeller and diffuser since the blade inlet angles and channel cross sections are too large for the reduced flow rate at part load. With the development of unstable disturbance, some complex flow structures with low-frequency high-energy would be generated; resulting instability on the performance curves, and sometimes even makes high cycle fatigue failures (Guo and Maruta 2005).

Some recirculations are observed at impeller inlet at sufficiently low flow, which can lead to performance instabilities for centrifugal pump at flow rates smaller than about 65 percent of the impeller inlet design flow rate (Murakami and Heya 1966, Sen 1978, Barrand, Caignaert et al. 1984).

The topic instabilities of the performance curve of pump turbine shall be explained with the help of Fig. 1.4, which contains the head and efficiency curve of a pump turbine (Sen 1978). For a centrifugal pump with $n_q = 35\text{min}^{-1}$, there is not only instability at small flow rate but also a distinct instability in the *Q-H* curve at more than 80 percent of the design flow rate, together with a local reduction of efficiency.

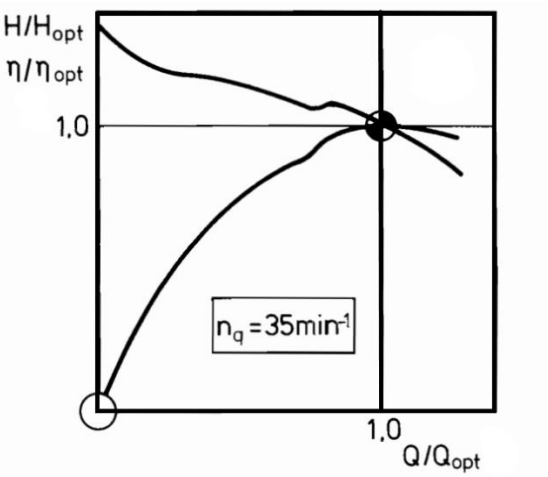

Fig. 1.4 The performance curve of pump turbine (Sen 1978)

The instability at small flow rate occurs very often in a centrifugal pump, which is due to a flow separation and a backflow region in impeller channels near the front disk. The effects of this instability on the performance characteristics are shown in a centrifugal volute pump with a specific speed of 85 min^{-1} in Fig. 1.5, which is shown in the literature (Sen 1978). The flow rate at which the backflow region appears in the impeller inlet section near front disk is about 65 percent of the design flow rate. With the further flow rate reduction, the back flow region grows in the upstream direction as well as inward from the pipe walls. It has a strong whirling motion, and its blockage effect shifts the through flow to a small zone around the pipe/pump axis. It is also called ‘part load whirl’ (PLW) due to this flow pattern.

The PLW also influences the incipient cavitation quantified by net positive suction head ($NPSH_i$) as shown in Fig. 1.5. At the onset of PLW, there is a maximum of $NPSH_i$. The value of $NPSH_i$ appears a steep decrease with the further flow reduction due to the abrupt change in the flow pattern. Accompanying the PLW, the cavitation bubbles show up near the hub. Considerable research work has been dedicated to the PLW (Murakami and Heya 1966, Sen 1978, Barrand, Caignaert et al. 1984).

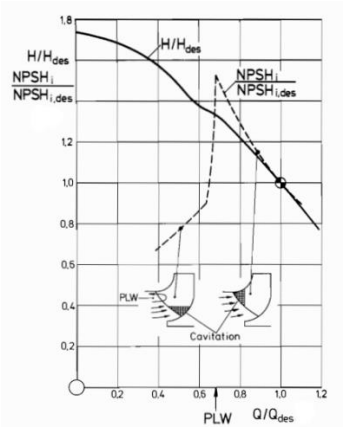

Fig. 1.5 The performance curve and incipient cavitation of a centrifugal volute pump with the specific speed 85 min^{-1} (Sen 1978)

The instability, which appears at greater flow rate than PLW, is called ‘full load instability’ (FLI) due to the onset point near the design flow rate. There is much evidence that the origin of this type of FLI of performance curves exists in a strong and very complicated backflow from the centrifugal pump with vaned diffuser and specific speed of greater than 30, thus this instability occurs very often in pump turbine on pump mode. With the growing of the specific speed, the risk of this instability increases, and the flow rate, where the *Q-H* curve becomes instable, moves much closer to the deign point. This type of instability is called ‘Type S’ or ‘saddle type’ due to the shape of the performance curve which looks like a saddle when the instability appears. A saddle-type instability is sometimes connected with a hysteresis (Fig. 1.6): with falling flow rate the sudden change of the head occurs at a lower flow rate than upon opening of the throttle valve. Typically this type of instability occurs at 60 to 90 percent of design flow rate, it not only limit the operating range but also can lead to a reduction of efficiency, high dynamic load, and cavitation up to the destruction of the pump.

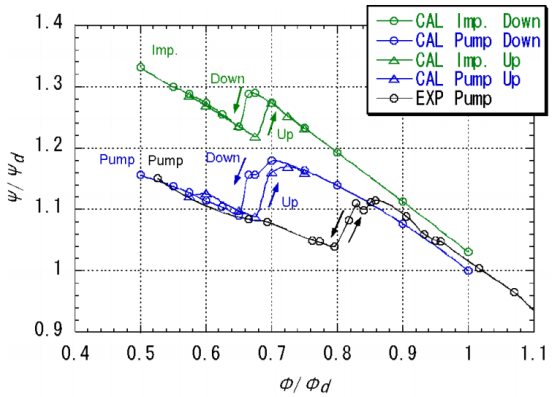

Fig. 1.6 The hysteresis effect in a centrifugal pump(Iino, Tanaka et al. 2003)

Thus, in order to get a safer and wider stable operating range of the pump turbine on pump mode, it is a very significant work to study the FLW. The aim of this investigation is to analyse the characteristics of the full load instabilities of the first stage of a two stages pump-turbine operating in pump-mode, and investigate the development of the unsteady phenomena.

1.4 The Flow Patterns in Impeller and Diffuser at Partload

For a centrifugal pump with a vaned diffuser at a low specific speed, the dents in curve near full load are often attributed to the flow instabilities in the vaned diffuser.

1.4.1 Flow Separation in Diffuser

The examples of the flow observation in a diffuser can be found in the literature (Gülich 2010). Observations of tufts in the diffuser of a pump with specific speed of 22 via different flow rates are shown in Fig. 1.7.

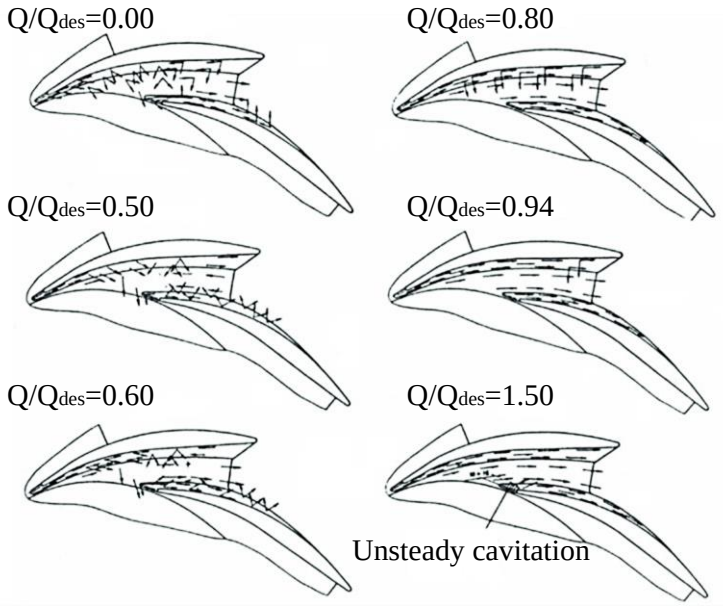

Fig. 1.7 Flow observations in a diffuser (Gülich 2010)

While the flow is at Q/Q_{des}= 1.5, an unsteady cavitation appears in the pressure side of the diffuser vane near the leading edge. An initial separations appear at Q/Q_{Des} = 0.94 near the diffuser outlet. At Q/Q_{Des} = 0.8, the stall spreads over the greatest part of the vane suction surface. At Q/Q_{Des} = 0.6, additional separations occur on the vane pressure surface, and the recirculation in the direction of the impeller is visible on the rear shroud just in front of the diffuser vane leading edge. The recirculation zone grows with the reduction of flow rate. Depending on the approach flow and the choice of the diffuser opening angle, the described phenomena occurs in different pumps at

different Q/Q_{Des}, but qualitatively they are typical for the flow through radial diffusers. In particular, the recirculation in all experiments occurred upstream of the diffuser vane leading edges or just before the volute cutwater (never in the middle between two vanes or near the vane suction surfaces). This recirculation from the diffuser into the impeller occurs at the impeller outlet. Consequently, there is a strong interaction between both components.

When these flow disturbances propagate in the circumferential direction, since the structure of the pump (a rotor, diffuser or volute) limits, would cause strong rotor and stator interaction and non-uniform flows. One of the main forms is stall (Sinha, Pinarbasi et al. 2001).

Several types of stall have been found in turbo machinery, such as alternate blade stall (A.B.S), rotating stall and so on. For 'alternate blade flow instabilities', they are firstly found in the impeller with an even number of blades, such as alternate blade cavitation in a inducer (Acosta 1958) and in a propeller turbine (Ishii 1962) or alternate blade stall in a centrifugal impeller (Wei, Yunchao et al. 2010). For the low specific speed centrifugal pumps with a vaned diffuser, the stall is also one of the main instabilities in vaned diffuser, the alternate stall and rotating stall has been both found in vane diffuser (Sano, Nakamura et al. 2000). By an experimental investigation, Takeshhi SANO et al (Sano, Nakamura et al. 2002) found that for narrow clearance with the strong rotor and stator interaction, the alternate blade stall and backward rotating stall mainly occurred. With increasing of the clearance, the forward rotating stall also occurred, and the onset of rotating stall shifted toward to the higher flow rate corresponding to the pressure performance in the vaned diffuser.

1.4.2 Flow Patterns in Impeller

Due to the Rotor-Stator Interaction (RSI) between diffuser and impeller, the flow patterns in impeller are also needed to be taken into account. With the variation of flow rate in centrifugal impeller, flow separation and secondary flow tend to generate loss mechanisms that are considerably more complicated than axial units. Normally, the flow in a centrifugal pump separates from the suction surface near the leading edge, and produces a substantial wake on the suction surfaces of each of the blades. Fischer and Thoma (Fischer and Thoma 1932) first identified this phenomenon, and observed that the wake can occur even at design flow.

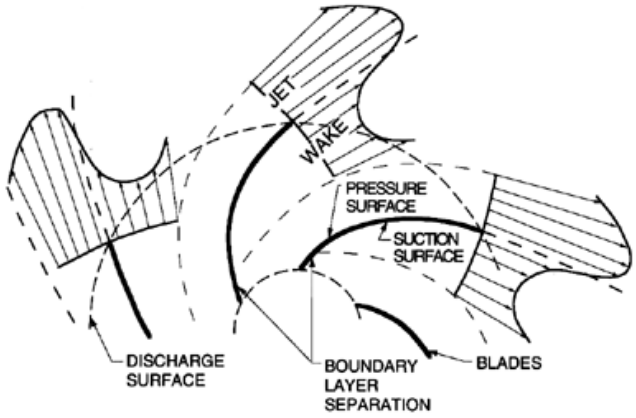

Fig. 1.8 The structure of ‘jet-wake’ in impeller

Normally, the wake extends all the way to the impeller discharge surface. Consequently, the discharge flow consists of a low velocity zone or wake next to the suction surface, and, necessarily, a flow of higher velocity in the rest of the blade passage. This ‘jet-wake structure’ of the discharge is sketched in Fig.1.8. Sturge and Cumpsty (Sturge and Cumpsty 1975) calculated the shape of the wake in a typical two-dimensional radial cascade, and used numerical methods to solve a free streamline problem. The velocity measurements, acquired with hot-wire anemometers by McLaughlin and Choi (Choi, McLaughlin et al. 2003), highlighted the structure of ‘jet-wake’. It is characterized by a high velocity zone (jet) near the pressure side of blade and a low velocity zone (wake) near the suction side of blade.

The work of Cavazzini (Cavazzini 2013) indicated several reasons for the creation of the wake zone near suction side. Firstly, a secondary flow in the blade passages carries the hub and shroud boundary layers to the blade suction side, which creates a region of low velocity. Secondly, the fluid particles are carried from the pressure side to the suction side in the same impeller passage along the hub and shroud due to the pressure gradient. Besides these secondary flows, other factors also affect the position and the entity for the wake zone, such as the flow rate, the rotation velocity and impeller geometry et al.

At design flow rate, the wake or boundary layer on the suction surface may be quite thin, but as the flow rate is decreased, the increased incidence leads to larger wakes (D 1932, Johnston and Dean 1966). The appearance of ‘jet-wake’ structure destabilizes the flow not only at impeller outlet but also in the upstream of diffuser. When the jet passes from one passage to the adjacent, it affects the flow around the trailing edge and goes upstream along the suction side. At the same time, the upstream of the diffuser is also influenced by the non-uniform flow from the outlet of impeller.

Additional, with the further reducing of flow rate, in the centrifugal pump with vaned diffuser, not only the instability in the vaned diffuser attributed the instability

of performance curve, but also the unsteady disturbance which appears at inlet of the impeller plays an increasingly important role (Hergt and Starke 1985). And the rotating cavitation was found in a wide range of part load operating points which incept at the leading edge of impeller suction side and it also easy to cause a 'sudden' head drop (Tsujimoto 2001, Friedrichs and Kosyna 2002, Iga, Nohml et al. 2004).

1.5 Overview of the Current Work

1.5.1 Situation of the Research

Reversible centrifugal unit is one of the most common and typical forms with 60m to 700m head of pumped storage hydroelectricity. For the requirement of the head of higher than 700m, the multistage pump turbine are needed in order to ensure good hydraulic efficiency and minimize stress and vibrations caused by the turbine components. In contrast with single stage centrifugal turbine pump, the internal flow of high head instabilities has more complicated features in multistage centrifugal pump turbine.

This research is conducted on a low-pressure stage of a two stages pump-turbine on pump mode, which could be seen as a centrifugal pump with multistage diffuser. Compared with other vaned centrifugal pumps, this pump model has a return system with continuous stay vanes which could guide the water to the next stage and make strong and complex rotor and stator interaction. Meanwhile, the mechanism of the flow structures in full load instabilities is very complicated.

Among all the phenomena, the unsteady flow-dynamics in full load instabilities is still an open question, and challenge fluid mechanical committee. During the past several decades, some experiments and numerical simulations have been carried out to study the effects of impeller/diffuser geometries and operating conditions on the unsteady interactions, for instance, Gonzalez et al. (González, Fernández et al. 2002), Hong and Kang (Hong and Kang 2004), Guo and Maruta (Guo and Maruta 2005), Majidi (Majidi 2005), Rodriguez et al.(Rodriguez, Egusquiza et al. 2007), Pavesi et al.(Pavesi, Cavazzini et al. 2008), Cavazzini et al.(Cavazzini, Pavesi et al. 2009), and Feng et al.(Feng, Benra et al. 2011).

The analysis on the unsteady pressure signal is an effective method to understand the characteristics and origin of the interactions. Several techniques (auto and cross spectra, coherence function, wavelets, etc.) have been frequently used to analyze in the frequency and time-frequency domain and to identify the flow structures and the propagation of the unsteadiness (Akin and Rockwell 1994, Ferrara, Ferrari et al. 2004, Horodko 2006, Horodko 2007).

Besides, several flow visualization technologies were also used to evidence and

describe the flow instabilities qualitatively in centrifugal pump such as Particle Image Velocimetry (PIV) , Laser Doppler Velocimetry (LDV) and High-Speed Visualization and so on (Wuibaut, Bois et al. 2002, Pedersen, Larsen et al. 2003, Feng, Benra et al. 2009).

Even though previous studies advanced the understanding on the unsteady phenomena in pumps, because of the scarce knowledge of the full-load instabilities and its effect in this kind of pump, a further investigation of the characteristics and flow mechanisms of full load instabilities is valuable for the safer and wider stable operating range of multistage pump turbine on pump mode.

1.5.2 Problems and Objective

In a previous study, the performance curve of the model pump has been acquired, evaluated in accordance with ISO standards, which shows a slightly saddle-type instabilities behaviour between Q/Q_{Des} ≈0.45 to 0.70 (Fig.1.9). Below Q/Q_{Des} ≈0.40 the characteristic is raised due to the effect of fully developed inlet recirculation (Yang, Pavesi et al. 2013).

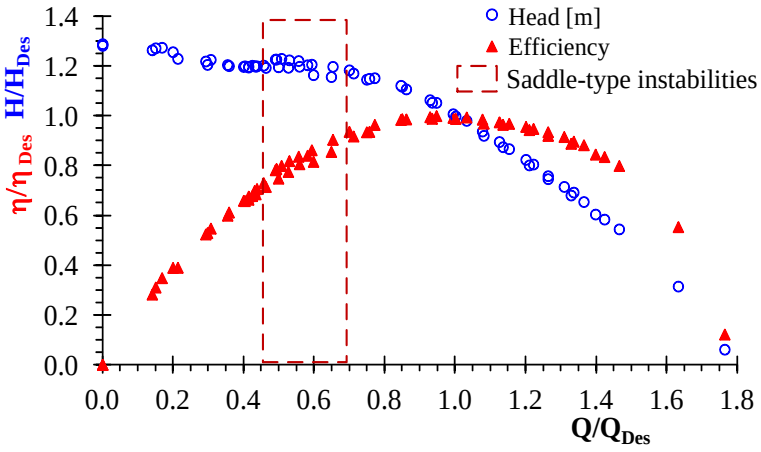

Fig. 1.9 Experimental pump characteristics and saddle-type instabilities region

The mean pressure variation at the impeller outlet was shown versus the flow rate in Fig.1.10. The diagram shows a slight but steady increase in the pressure fluctuation of the flow rate not far from the design flow rate and a sharp increase of the pressure variation when the flow rate decreases to below the critical value Q/Q_{Des} ≈0.7, which is the same flow rate value when the head characteristic was observed unstable. During the saddle instability region, there is a sharp decline in the mean pressure at impeller outlet near the Q/Q_{Des} ≈ 0.6.

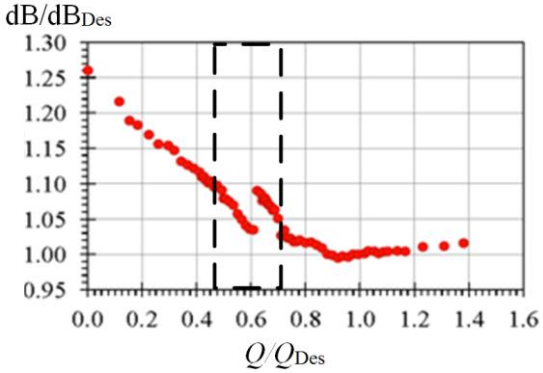

Fig. 1.10 Mean pressure variation at the exit of the impeller versus the flow

The aim of this investigation was to analyze the characteristics of the full load instabilities of a low-pressure stage of a two stages pump-turbine operating in pump-mode, study the development of the unsteady phenomena in this flow rate interval, and find the reasons of the drop of the mean pressure at the exit of the impeller in saddle instability region.

1.5.3 Document Organization

The thesis has been structured into four parts, as follows:

Part I offered an introduction about the background of the research topic in this thesis. It includes the brief introduction of pumped-storage technology and the role pump turbine plays in this technology. In addition, the factors limited the stable operating region of a pump turbine in pump mode was introduced to make readers familiar with the reversible pump turbine technical challenges along with the objective of the current study.

Part II concerned the experimental investigation, including the investigation methodology and the measurements results. The Open Turbine Facility used for the experimental investigation was detailed. It contains the pump model, global performance measurement, pressure instrumentation in diffuser and High-Speed Visualization techniques. The pressure variations in diffuser vanes both in time and frequency domains were analysed. The flow field in the instability region from 0.45 to 0.70 Q_{Des} was investigated as well.

Part III presented the discussion about the investigation metrology about the numerical simulation both in flow field and in the intensity of dipole sources. Furthermore, the numerical simulation results were analyzed. The types and development of unsteady disturbance inner pump were captured combined with the experimental results. The reasons of the slop of head and mean pressure at exit of impeller were found in the saddle instability region which closer to the design point.

Part IV drew the conclusions and suggested future investigation directions.

II Experimental Investigation

Chapter 2 Investigation Methodology of Experiment

2.1 Overview of the Open Turbomachinery Facility

The model pump turbine investigated in the present work is installed at the Waterpower laboratory in the Department of Industrial Engineering, University of Padua in Italy. Experimental measurements were carried out using the open loop water circuit configuration. Water from the basement was pumped to the overhead tank and flowed down to the pump inlet pipeline. A uniform level of the water head was maintained in the overhead tank at all operating. The outlet tube was connected to the downstream large basement, which was open to the air, and the water was released back to the overhead tank.

The experimental measurements, calibrations, and computations were performed using the procedure and guidelines given in IEC 60041, IEC 60193(Commission 1991, Commission 1999). The average pressure was measured through four circular taps located at the turbine outlet and the draft tube inlet. A calibrated nozzle flow meter was used to measure the flow rate. Data from the instruments were recorded using a computer with a LabView program developed in the laboratory.

Fig.2.1 Experimental validation facility in open loop serial pump configuration

2.1.1 Reversible Pump-Turbine Scale Model

The analyzed pump-turbine is a low-pressure stage of a two stages pump-turbine in the pump operating mode. The model, which consists of an impeller and refeeding channels, is shown in Fig. 2.2. Geometry and performance characteristics of the tested pump-turbine are listed in Table 2.1.

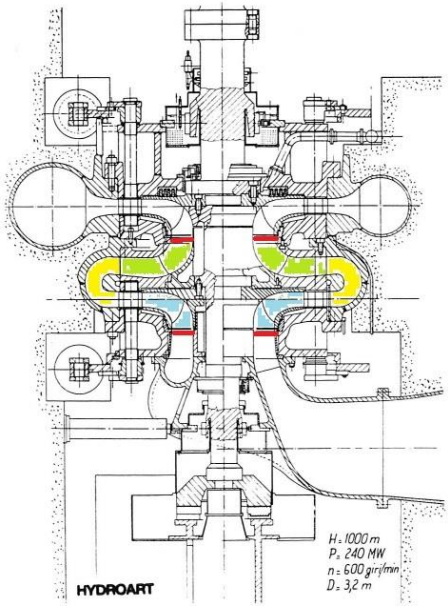

(a) Meridian plane

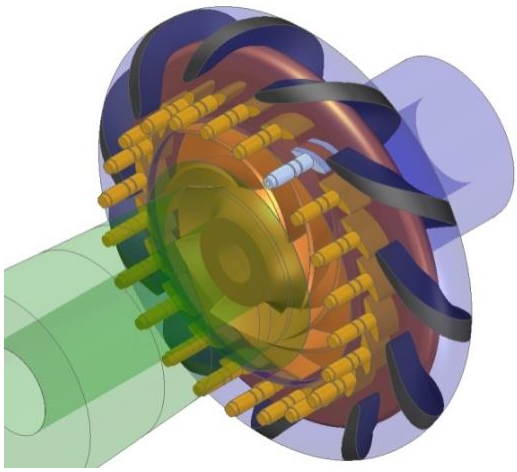

(b) 3-D schematic

Fig. 2.2 Experimental validation facilities in open loop serial pump configuration

Table 2.1 Geometry and performance parameters of the tested pump-turbine.

Impeller data				
D_2 (mm)	B_2 (mm)	n_{b2}	β_{2c}(°)	ϕ_{Des}
400	40	7	26.5	0.125
Diffuser vanes data				
D_3 (mm)	B_3 (mm)	n_{b3}	α_{3c} (°)	λ (°)
410	40	22	18	8
Return channel vanes data				
D_4 (mm)	B_4 (mm)	n_{b4}	α_{4c} (°)	
516	40	11	30	

The impeller is a radial, shrouded impeller with seven 3D backward swept blades with a discharge angle of 26.5 °referred to the tangent and a design specific speed n_p = 37.6 m0.75s$^{-1.5}$ (dimensionless design specific speed ω_s = 0.71). The impeller rotating frequency is f_{IR}=10Hz and the blade pass frequency is f_{BPF}=70Hz.

The Refeeding channels were used to guide the flow that leaves from impeller to the inlet of the subsequent. The channels are made up of twenty two adjustable guide-diffuser vanes and eleven continuous vanes. The guide-diffuser allows continuous and independent adjustment of the vane angle and the relative azimuthally position with the return channel vanes. The radial gap in the configuration under test between the impeller tip and the inlet edge of the stator vanes is 10.5 mm, which is 5.25% of the impeller radius.

2.2 Digital Data Acquisition

The facility contains the following instrumentation:

- Global performance measurements
- Dynamic pressure measurement
- High-speed flow visualization

The measurement data acquisition is conducted using LabView software and the data acquisition devices for global performance measurements and dynamic pressure measurement are mounted on the National Instruments workstation model NI PXI-1042 (see Fig. 2.3) with the parameters listed in Table 2.2.

Fig. 2.3 National Instruments workstation NI PXI-1042

Table 2.2 Main parameters of the workstation NI PXI-1042

Processor	1266 *MHz*
Hard-disk	20 *G bit*
RAM	$\pm 10V$
Operating system	Windows 7 professional
Software for data elaboration	National Instruments Labview 2012

2.2.1 Global Performance Measurements

The global performance characteristics are obtained using three measurements as below.

(1) Static Pressure measurement at the pump inlet and outlet

A relative transducer model WIKA (Fig 2.4(a)), type 891.12.500 is placed at the inlet of the pump with a working range of -1~+1bar, and an absolute transducer model PHILIPS (Fig.2.4 (b)), type 9404 215 60161 is installed at the outlet of the pump with the working range of 0~2.5bar.

These transducers are connected to the main pipe through little rubber pipes. Some junctions, which are shown in Fig. 2.5, were made in order to acquire the pressure signal in four different points placed around the pipe at circumferential distances of 90r. In order to eliminate possible air bubbles, T-shaped branches with

taps are inserted.

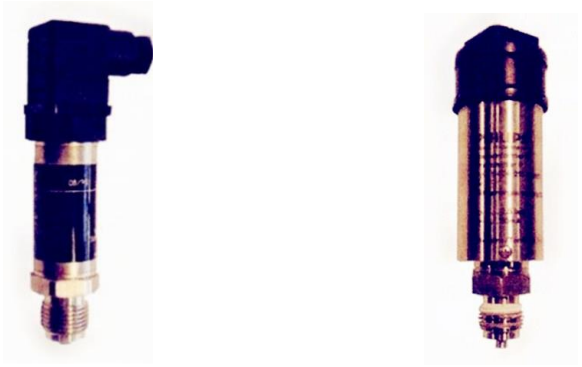

(a) Relative transducer (b) Absolute transducer

Fig.2.4 Pressure transducer

Fig.2.5 Connection between a pipe and transducers

(2) Nozzle flow measurement

Nozzle flow meter, as shown in Fig. 2.6 (a), is one of flow metering devices based on the Bernoulli Equation: the downstream pressure after an obstruction will be lower than the upstream pressure.

A Honeywell wet/wet differential transducer model FDW, which connected upstream and downstream of the nozzle, was used to measure the Δ p, and its order code is FDW1 MD 2G 5B 6A (Fig. 2.6 (b)), with the accuracy of 0.1 %, measurement range of 0.5 bar, output of 0 ~10 VDC, pressure ports of ¼-18 NPT male, Bendix connector PTIH-10-6P.

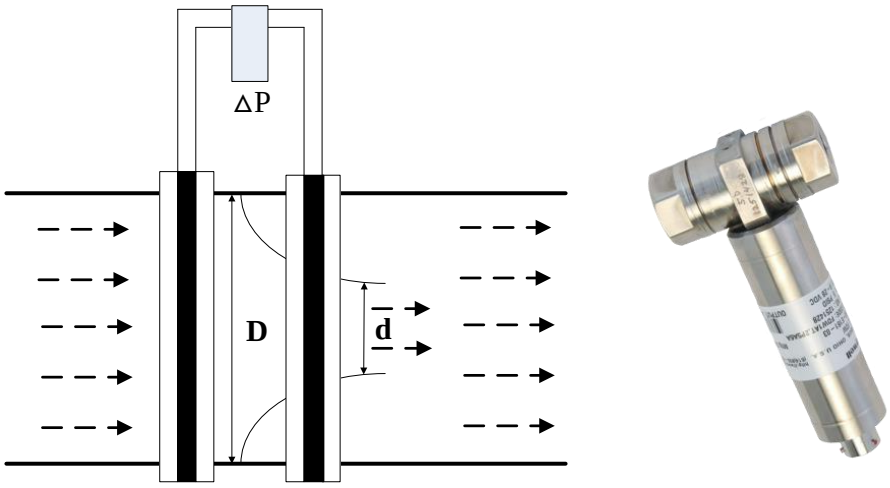

(a) (b)

Fig.2.6 Nozzle flow meter

The calculations for nozzles carrying a liquid as described in Eq. (2-1) according to ASME PTC 19.5-2004 (PTC19 2004)..

$$Q_m = \frac{CA_{throat}\sqrt{2\rho\Delta p}}{\sqrt{1-\beta^4}} \tag{2-1}$$

where

- D=the maximum diameter of the nozzle
- d=the minimum diameter of the nozzle
- $\beta = \frac{d}{D}$
- $A_{throat} = \frac{\pi}{4}d^2$
- ρ=the water density in the upstream of the nozzle
- C=the efflux coefficient of the nozzle

ISA 1932 nozzle issued in this test rig, and ISA 1932 Nozzle Discharge Coefficient Equation is listed as below:

$$C = 0.9900 - 0.2262(\beta)^{4.1} - \left[0.00175(\beta)^2 - 0.0033(\beta)^{4.15}\right]\left[10^6 / Re_D\right]^{1.15} \tag{2-2}$$

The Reynolds number Re_D is used for calculating the efflux coefficient which depends on its turn of the mass flow rate:

$$Re_D = \frac{4q_m}{\pi \mu_1 D} \tag{2-3}$$

where μ_1 is the dynamic viscosity and the value is $1.134 \cdot 10^{-3} Pa$. In order to solve the flow rate, an iterative calculation is necessary. For the first attempt, the initial value of the flow rate is estimated and is inserted in Eq. (2-3) to obtain Re_D. With the value of Re_D and pressure differences measured by the Honeywell wet/wet differential transducer, the new value for the mass flow rate could be calculated using the Eq. (2-4):

$$q_m = [0.9900 - 2.2262 \cdot \beta^{4.1} - (0.00175 \cdot \beta^{4.15})(\frac{10^6}{Re_D})^{1.15}] \cdot \frac{\pi}{4} d^2 \cdot \frac{\sqrt{2\Delta p \rho_1}}{\sqrt{1-\beta^4}} \tag{2-4}$$

where ρ_1 is the density of water under 20 degrees Celsius and the value is 998.43kg/m^3. In iterative process, the value is accepted if the difference with previous iteration is smaller than 0.1, otherwise the process is re-started until it is converged. LabView 2012 realized this computing process.

As for the power supply, a feeder of 28 V DC is used for feeding the pressure transducers in the static pressure measurement at the pump intake and delivery, and another one of 12 V DC is used for feeding the differential transducer in nozzle flow measurement.

The calibration of the pressure transducers and the uncertainty analysis of this flow rate measurement were introduced in detail in Giovanna Cavazzini's work (Cavazzini 2013).

(3) Shaft torque measurement

The shaft torque was measured using Kistler Model 4503A Torque Sensor. The torque sensor with built-in speed sensor, which is shown in Fig. 2.7, operates on the strain gage principle. It is suitable for use at rotational speeds of up to 7000 rev/min, and the maximum measured value is 200 N·m.

Fig. 2.7 Torque sensor

The data acquisition device National Instruments, model 6070E, of which the main characteristics were shown in Table 2.3, acquired the static pressure signals and the signal from torque sensor for the global performance measurements.

Table 2.3 Main parameters of the NI data acquisition device 6070E

Resolution	12 *bits*
Maximum sampling rate	1.25 *MS/s*
Input range	±0.5 to ±10*V*
Output range	10*V*

2.2.2 Dynamic Pressure Measurement

The dynamic pressure was measured with 12 pressure sensors "Kulite Semiconductor" (see Fig. 2.8), model XCL-072 transducers, with a declared sensitivity of about 29.3 mV/Bar, and a working field of 0~3.5Bar. The combined non-linearity, hysteresis, and repeatability of the sensors were better than ±0.1%. The sensors were placed aligning with the wall at the mid-height of one diffuser guide vane (as shown in Fig. 2.9) and the sensitivity of the sensors were listed in Table 2.4.

Fig.2.8 Pressure sensor Kulite semiconductor

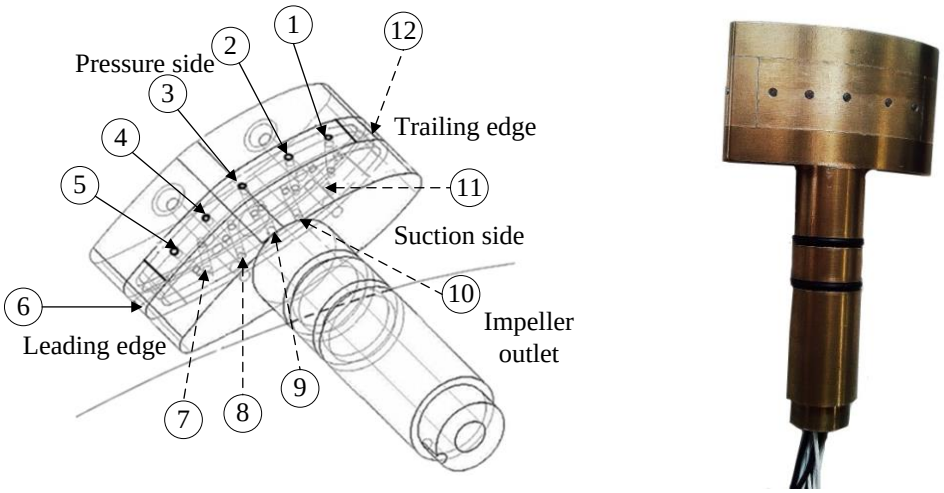

(a) (b)

Fig.2.9 The distribution of pressure sensors

Table 2.4 The sensitivity of XCL-072transducers

Point number	Sensor number	Sensitivity
Point 1	110	28.586 mV / bar
Point 2	7677-4-299	58.276 mV / bar
Point 3	117	28.491 mV / bar
Point 4	99	28.617 mV / bar
Point 5	116	28.420 mV / bar
Point 6	7677-4-297	50.088 mV / bar
Point 7	118	28.509 mV / bar
Point 8	46	26.150 mV / bar
Point 9	192	2857.639 mV / bar
Point 10	7677-4-307	58.276 mV / bar
Point 11	113	28.374 mV / bar
Point 12	44	26.194 mV / bar

The transducers were fed with a stabilized power supply of the Thurlby Thandar Instruments QL355T (see Fig. 2.10). XCL-072 transducers were fed with two different volt values, the sensors without amplifier were 10V DC, and 28V DC was for the sensors with amplifier.

Fig.2.10 “Thurlby Thandar Instruments” QL355T

For the dynamic pressure measurement, the data from the Kulite sensors were acquired by the data acquisition device National Instruments, model 4472 (see Table 2.5)

Table 2.5 Main parameters of the NI data acquisition device4472

Resolution	24 *bits*
Maximum sampling rate	1104.4 *KS/s*
Input range	$\pm 10V$

For these two measurements, the connection to the data acquisition device was made through a configurable connector “national instruments”, model CA-1000 (Fig. 2.11). In these connector the resistances of 1000 Ω and 5000 Ω were connected for converting the mV of the output of the sensors into a more convenient Volt scale according to the characteristics of the data acquisition device.

Fig. 2.11 The configurable connector CA-1000

2.2.3 Flow Visualization Techniques

To analyze and describe the movement of flow passage between vanes in diffuser and return channel qualitatively, high-speed flow visualizations were performed. Photron FASTCAM PCI digital camera (Fig. 2.12) was used, and the video camera recorded images at full resolution (512×512 pixels). Fps is the maximum frames-per-second at the maximum resolution; the results of high speed camera are with a frame rate 5000 fps and a shutter 1/5000.

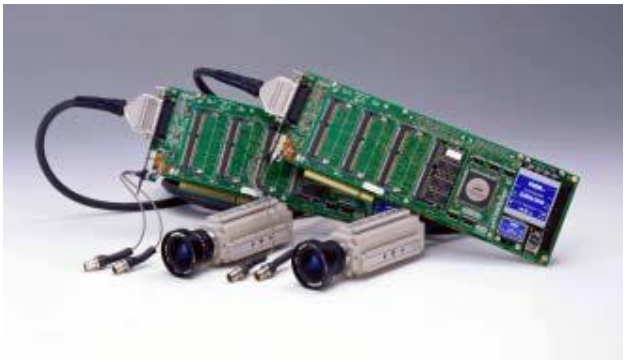

Fig. 2.12 Photron FASTCAM PCI digital camera

A needle valve was employed to control the amount of injected air throughout a hole of 0.5 mm diameter located in the mid span of the diffuser and return channel vanes. The distribution of holes in vane and return channel was shown in Fig. 2.13. The injection pressure was maintained at a value which is slightly above the mean pressure at the injection location. For this purpose, two tungsten halogen bulbs with 1000W were equipped to provide the light of the scene.

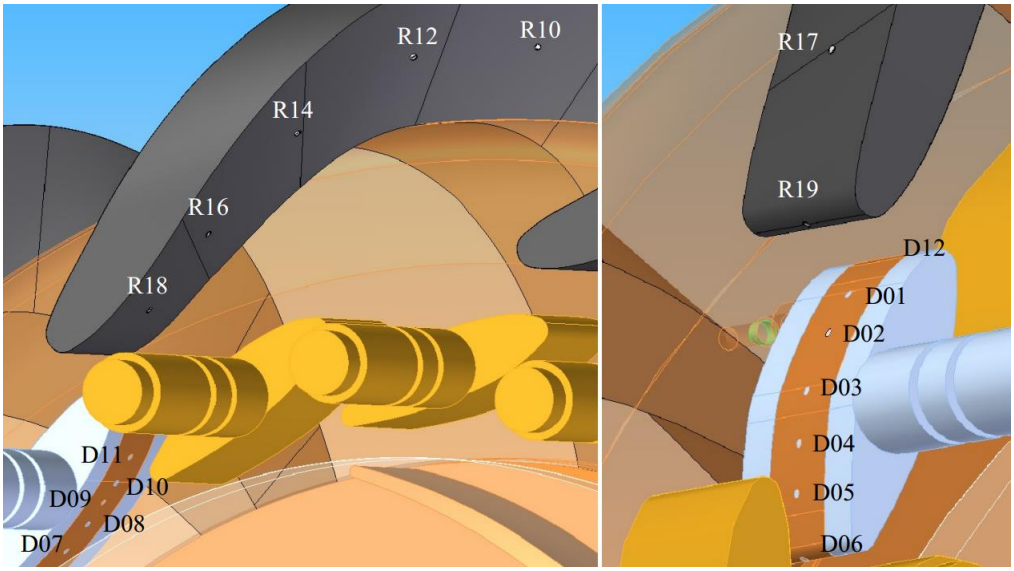

Fig.2.13 The distribution of holes in vane and return channel

2.3 Signal Analysis

Signal analysis is more and more widely used as an important research tool to extract information from signals, which is related to the real-world phenomena. As the Fig.2.14 shown, for this analysis, a time-domain graph shows how a signal changes over time, whereas a frequency-domain graph shows how much of the signal lies within each given frequency band over a range of frequencies. A frequency-domain representation can also include information on the phase shift that must be applied to each sinusoid in order to be able to recombine the frequency components to recover the original time signal.

In this study, the analysis of dynamic pressure signals is used to get more details on the unsteadiness including deterministic and non-deterministic phenomena in pump turbine.

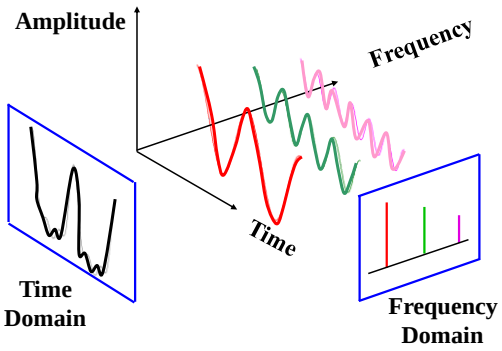

Fig. 2.14 Signal in time and frequency domain

2.3.1 Analog-to-digital Conversion

The signal acquired from transducers is a series of analog signal. Digital signal processing (DSP) is used to processing the signal form transducers in this study. DSP is one subfield of signal processing, and the goal of DSP is usually to measure, filter and/or compress continuous real-world analog signals.

The first step of DSP is usually to convert the signal from an analog to a digital form, this processing named analog-to-digital conversion (ADC).

An analog or analogue signal, as shown in Fig. 2.15(a), is any continuous signal for which the time varying feature (variable) of the signal is a representation of some other time varying quantity, i.e., analogous to another time varying signal.

A digital signal, as shown in Fig. 2.15(b), is a physical signal that is a representation of a sequence of discrete values (a quantified discrete-time signal), for example of an arbitrary bit stream, or of a digitized (sampled and analog-to-digital converted) analog signal.

Unlike a continuous-time signal, analog signal is discrete-time signal and not a function of a continuous argument. Therefore, ADC was adopted to make this signal to be converted to digital (discrete-valued discrete-time) signals which could be processed numerically in the data processing. This process mainly consists of two steps: sampling and quantizing.

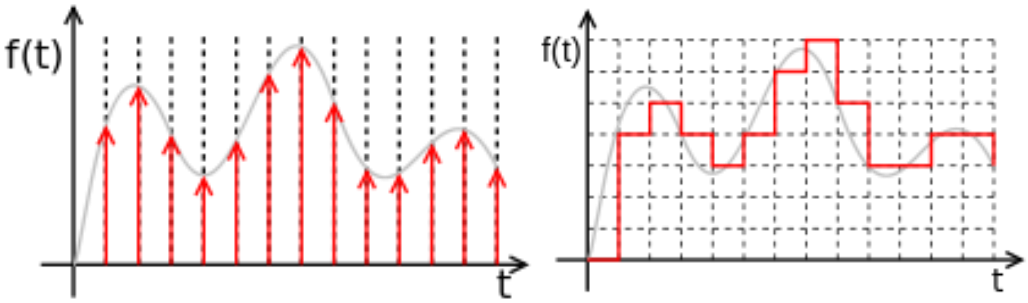

(a) Analog signal (b) Digital signal

Fig. 2.15 The analog and digital signal

Sampling is the reduction of a continuous signal to a discrete signal, and it can be done for functions varying in space, time, or any other dimension, and similar results are obtained in two or more dimensions. The analog signal has been obtained by sampling from a continuous-time signal, and then each value in the sequence is called a sample.

For sampling, $x(t)$ was defined to describe a continuous function (or "signal") to be sampled, and sampling would be performed by measuring the value of the continuous function every T seconds, which is called the sampling interval(Weik 1998). Then the sampled function is given by the sequence $x(n\mathrm{T})$, n is an integer value.

The sampling frequency or sampling rate, fs, is defined as the number of samples obtained in one second (samples per second), thus fs = 1/T.

Reconstructing $x(t)$ from samples is done by interpolation algorithms as shown in Fig. 2.16. The continuous-time signal $x(t)$ is represented with a green coloured line while the discrete sampled ware indicated by the blue vertical line.

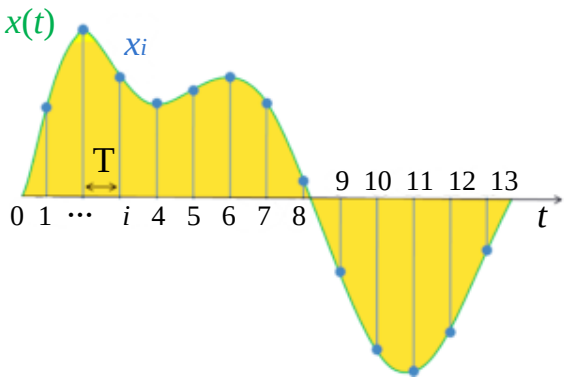

Fig 2.16 Reconstruction of the continuous-time signal

The appropriate selection of sampling rate is crucial for the sampling of signal. Take a sinusoid signal as an example; a set of samples with sampling interval equal to 1s was acquired. In the Fig. 2.17, the red line is the sampled signal. Based on the sample data (sampling frequency f_s=1), two different sinusoids that could have been produced. Nine cycles of the red sinusoid and one cycle of the blue sinusoid span an interval of 10 samples. The corresponding number of cycles per sample are f_{red}=0.9Hz and f_{blue}=0.1Hz. The resulting number of cycles per sample is f/f_s which is known as normalized frequency, and the samples are indistinguishable from those of another sinusoid (called an alias) whose normalized frequency differs from f/f_s by any integer (Mitchell and Netravali 1988). The frequency appears alias named $f_{alias,}$ and all the aliases of frequency could be expressed as

$$f_{alias}(N) \overset{def}{=} \left| f - Nf_s \right| \tag{2-5}$$

where N is an integer, and $f_{alias}(0) = f$, and N has units of cycles per sample. Therefore, the N = 1 alias of f_{red} is f_{blue}, and vice versa.

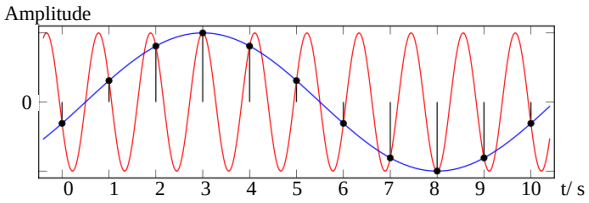

Fig 2.17An example of incorrect sampling frequency

The Nyquist–Shannon sampling theorem states that a signal can be exactly reconstructed from its samples if $f_s/2>f$. Any frequency component above $f_s/2$ is indistinguishable from a lower-frequency component. In addition, for the band-limited signal, if the Nyquist criterion is not satisfied, adjacent copies overlap as Fig 2.18 shown. The blue one is the original transforms, and the green images are the adjacent copies.

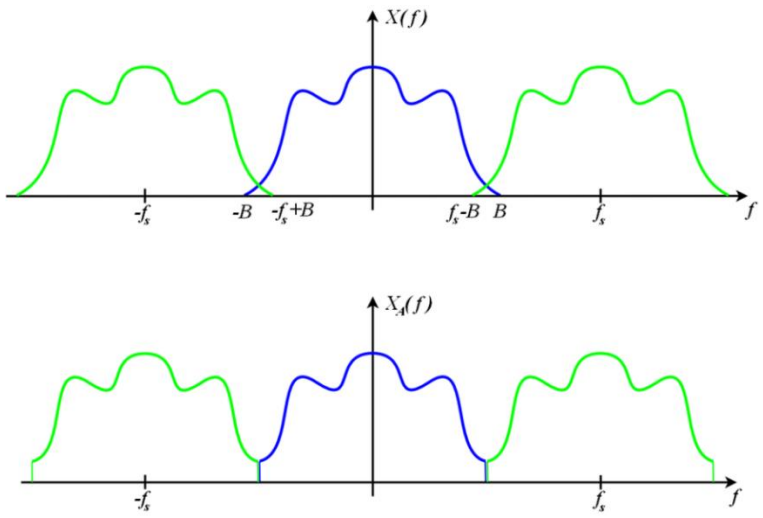

Fig 2.18The overlap of the adjacent copies

The bandwidth of the physical signals is not always completely known, it is wise to choose a sampling frequency much greater than the supposed maximum frequency. In this work, the concern is on the unsteady flow patterns at part load, which is supposed to have the frequencies near the blade pass frequency (BPF, 70Hz). Since the sampling rate of the pressure signal need to be chosen greater than 2BPF, 1024Hz was adopted in this experiment.

Then the signals usually proceed by replacing each original sample value by an approximation, which is selected from a given discrete set, i.e., this process is known as quantization. In this process, an analog-to-digital converter (ADC) is applied, which turns the analog signal into a stream of numbers.

As shown in Fig 2.19 (a), the blue line is the original signal and the red line is the quantized signal. The process loses some information, and the discrete-valued signals are only an approximation of the converted continuous-valued discrete-time signal, which approximates the original continuous-valued continuous-time signal. Therefore, there is a quantization error between the analog input voltage to the ADC and the output-digitized value. The blue line in Fig 2.19 (b) is the quantization error, which is "added" to the quantized signal. This is the source of noise.

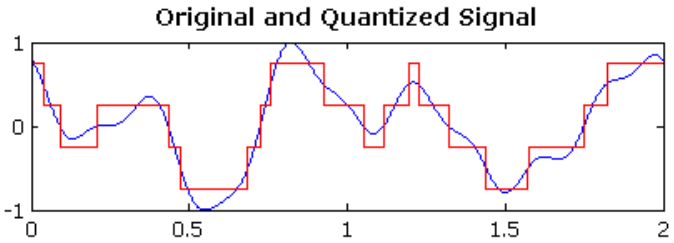

(a)

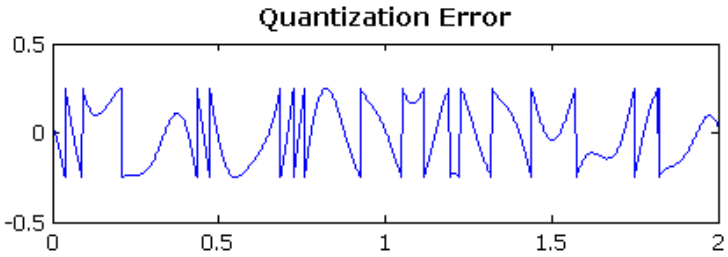

(b)

Fig 2.19 Analog, digitized signal and quantization error

2.3.2 Processing in Time Domain

In DSP, the digital signals were usually to be studied in one of the following domains: time domain (one-dimensional signals), spatial domain (multidimensional signals), frequency domain, and wavelet domains. The suitable domain was chosen to best represent the essential characteristics of the signal.

In this study, a sequence of samples from transducers measurement produces a time domain representation. It was processed in the time domain by filtering which could be enhancement of the input signal. A lowpass filter with infinite impulse response (IIR) was used to filter the pressure signal form XCL-072transducers. Fig 2.20 shows the effect of signal filtering.

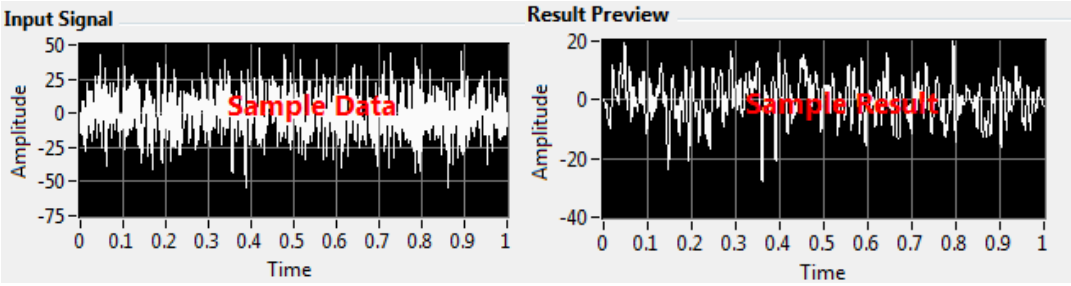

Fig 2.20 Effect of signal filtering

2.3.3 Processing in Frequency Domain

2.3.3.1 Frequency Analysis

In this work, the frequency domain analysis was carried out to identify and characterize the unsteady phenomena in the pump turbine. The pressure signal acquired from transducers can be converted from the time domain to frequency domain with a pair of mathematical operators called a transformation. In the pressure analysis, the phase information is also needed, and the method how the phase varies with frequency can be a significant consideration for the study of the unsteady pattern. The Fourier transformation was used to convert the signal information to a magnitude and phase component of each frequency in this study.

The discrete Fourier transform (DFT) is one kind of Fourier transform, which is used to converts a finite list of equally spaced samples into a list of coefficients of a finite combination of complex sinusoids ordered by their frequencies, that has those same sample values.

The definition of DFT is introduced as bellow. It is assumed that the signal $\{x[n]\}_{0\le n<N}$) to be analyzed is a sequence of N real or complex values which are a function of the integer variable n. The 'spectrum' of frequency components is the frequency domain representation of the signal. A spectrum analyzer is the tool commonly used to visualize real-world signals in the frequency domain. The DFT of $x[n]$, which is also called as the spectrum of $x[n]$, is a length N sequence of complex numbers denoted $\hat{x}(k)$ and defined by:

$$\hat{x}(k) = \sum_{n=0}^{N-1} e^{-i\frac{2\pi}{N}nk} x[n] \quad k = 0\,,\,1\text{;}\cdot,\ N- \tag{2-6}$$

where *e* is the base number of natural logarithm, *i* is the unit of imaginary number. Normally, the sign *F* is used to express this transform as bellow:

$$\hat{x}=\mathcal{F}x \tag{2-7}$$

The fast Fourier transform (FFT) is a method for computing the discrete Fourier transform of a sampled signal. In practice, nearly all software and electronic devices, which generate frequency spectra, apply a fast Fourier transform (FFT).

However, the transformation gives only a representation of the process but not a statistical description, which consider the randomness of the process. The signal from experiment test was inevitably corrupted by some random noise such as a measurement error, digitization error, and thermal noise, etc. Therefore, it is necessary to resort to a random signal processing theory.

For this purpose, spectral density estimation (SDE) is used to estimate the spectral density (also known as the power spectral density, PSD) of a random signal from a sequence of time samples of the pressure signal in this experiment. Intuitively speaking, the spectral density characterizes the frequency content of the signal.

The power spectrum of a time-series $x(t)$ describes how the variance of the data $x(t)$ is distributed over the frequency components into which $x(t)$ may be decomposed. This distribution of the variance may be described either by a measurement value, or by a statistical cumulative distribution function, which is equal to the power contributed by frequencies from 0 up to *f*.

For the signal processing in this study, the statistical cumulative distribution functions adopted to describe the distribution of the variance of signal. The auto-correlation function is defined as the following equation for the analysis.

$$r_x(\tau) = E[x(t+\tau)x^*(t)] \tag{2-8}$$

where $x^*(t)$ is the complex conjugate of $x(t)$, and τ is time-lag.

One may already guess that for a stationary random process, the power spectral density and the autocorrelation function of this signal should be a Fourier transform pair. If the mean value is not zero, the Fourier transform does not exist. Fortunately, the Wiener–Khinchine theorem makes sense of this formula for any wide-sense stationary process. The power spectrum density $G_{xx}(f)$ could be written as bellow:

$$G_{xx}(f) = \lim_{T\to\infty} E(\frac{1}{T}\left|X(f)_T\right|^2) \quad (2\text{-}9)$$

where $X(f)$ is the fast Fourier transform of the segment of the signal *x*.

Techniques for spectrum estimation can generally be divided into parametric and non-parametric methods. The parametric approaches assume that the underlying stationary stochastic process has a certain structure, which can be described using a small number of parameters (for example, using an auto-regressive or moving average model). In these approaches, the task is to estimate the parameters of the model that describes the stochastic process. By contrast, non-parametric approaches explicitly estimate the covariance or the spectrum of the process without assuming that the process has any particular structure.

There are many different spectral density estimation techniques. The periodogram is one of the most common techniques for the engineering applications. In practice, the periodogram is often computed from a finite-length digital sequence using the fast Fourier transform (FFT). The raw periodogram is not a good spectral estimate because of spectral bias and the fact that the variance at a given frequency does not decrease as the number of samples used in the computation increases.

The spectral bias problem arises from a sharp truncation of the sequence, and can be reduced by first multiplying the finite sequence by a window function, which truncates the sequence gradually rather than abruptly.

The variance problem can be reduced by smoothing the periodogram. Various techniques to reduce spectral bias and variance are adopted. One technique is Bartlett's method also known as the method of averaged periodograms(Engelberg 2008). It provides a way to reduce the variance of the periodogram in exchange for a reduction of resolution, compared to standard periodograms(Bartlett 1948, Bartlett 1950). The idea is to divide the set of N samples into L sets of M samples, compute the discrete Fourier transform (DFT) of each set, square it to get the power spectral density and compute the average of all of them. This leads to a reduction in the standard deviation as$1/\sqrt{L}$.

Welch's method is a windowed version of Bartlett's method, which uses overlapping segments. For Welch's method, the original data segment is split up into N data segments of length M, overlapping by D points. If D = M / 2, the overlap is said to be 50%, while the overlap is said to be 0% when D = 0.

The overlapping segments are then windowed: After the data are split up into overlapping segments, the individual N data segments have a window applied to them

(in the time domain). The windowing of the segments is what makes the Welch method a "modified" periodogram.

In this study, the Welch's method is used to estimate the power spectra of the pressure signal. It is computed by partitioning each time signal into 2^8 segments of 2^{13} samples with overlapping percent 50%, filtered with a Hanning window for avoiding aliasing and leakage errors. The frequency resolution is 0.125Hz. The auto-spectra and the cross-spectra are computed by the following equation(Farge 1992):

$$G_{xy}(f) = \frac{1}{NW_H} \sum_{k=1}^{N} [X_k^*(f) X_k(f)] \tag{2-10}$$

where N is the number of segments, W_H is weighting constant corresponding to the Hanning windows, $X_k(f)$ is the fast Fourier transform of the k^{th} data segment of the signal *e*xpand $X_k^*(f)$ is the complex conjugate of $X_k(f)$.

2.3.3.2 Time-frequency analysis

A time-frequency analysis is carried out by the wavelet transforms to provide information on the variation of pressure spectral frequencies components versus time. The continuous wavelet transform W(s, n) of the discrete sampled pressure signal x_n is computed via the FFT-based fast convolution:

$$W(s,n) = \sum_{k=0}^{N-1} X_k \left(\sqrt{\frac{2\pi s}{\delta t}} \psi_0^*(s\omega_k) e^{i\omega_k n \delta t} \right) \tag{2-11}$$

where s is the wavelet scale, n is the localized time index, k is frequency index, X_k is the discrete Fourier transform (DFT) of x_n, N is the data series length, and δt is the sample time interval. $\sqrt{2\pi s/\delta t}$ is a normalization factor which could obtain unit energy at each scale. $\psi_0^*(s\omega_k)$ is the complex conjugate of the Fourier transform of the scaled version of the "mother wavelet" $\psi(t)$ and ω_k is the angular frequency. The choice of the mother wavelet depends on several factors (Torrence and Compo 1998) and in this paper complex Morlet wavelets were used with $2\pi f_0 = 6$, since it could provide a good balance between time and frequency localization and it returned information about both amplitude and phase.

In order to determine the relation between two pressure signals in the time–frequency domains, the cross-wavelet spectrum is determined as the following equation.

$$W^{xy}(s,n) = W^x(s,n) W^{y*}(s,n) \tag{2-12}$$

2.3.3.3 Bispectrum analysis

The signal from experiment and simulation are analyzed in both the frequency domain and the time-frequency domains to identify and characterize the unsteady phenomena. Furthermore, every unsteady flow structure produces disturbances throughout a singular interval, so it is expected that the complete collection of unsteady features inside a turbo machine is a complex, highly interacted energy spectrum includes several force and unforced unsteadiness. This study is mainly focused on the so called "unforced unsteadiness" of the flow in a radial flow pump(Fernández Oro, Blanco Marigorta et al. 2009, Pavesi, Dazin et al. 2011), i.e. on the unsteady phenomena not connected with the blade passage frequency. The development of these instabilities insides turbomachines negatively affects their performance in terms of efficiency, vibrations, stability and noise emission.

In order to identify the frequency of the unforced unsteady features and the interacted parts in spectrum of the frequency domain, a bispectrum analysis is carried out in this paper.

Bispectral analysis is an advanced signal processing technique, which quantifies quadratic nonlinearities and deviations from normality. The bispectrum B(*f1, f2*)is a function of two frequency variable *f1* and *f2*, and it is computed as the following equation(Sigl and Chamoun 1994).

$$B(f_1, f_2) = \left| \sum_{k=1}^{N} X_k(f_1) X_k(f_2) X_k^*(f_1 + f_2) \right| \tag{2-13}$$

Chapter 3 Analysis of Experimental Results

3.1 Analysis of the Pressure Signals

In order to enhance the experimental repeatability, four series of tests were repeated to study the pressure characteristics in the saddle-instability region. The pressure analysis of two series of tests is outlined in this section. During the saddle-instability region, the *Q-H* curves of these four campaigns are drawn in Fig.3.1. It is found that there is a head hump near the critical flow rate 0.6 Q_{Des} which appears a drop of mean pressure variation at outlet of impeller. In this section, the dynamic characteristics of the pressure during this region are analyzed.

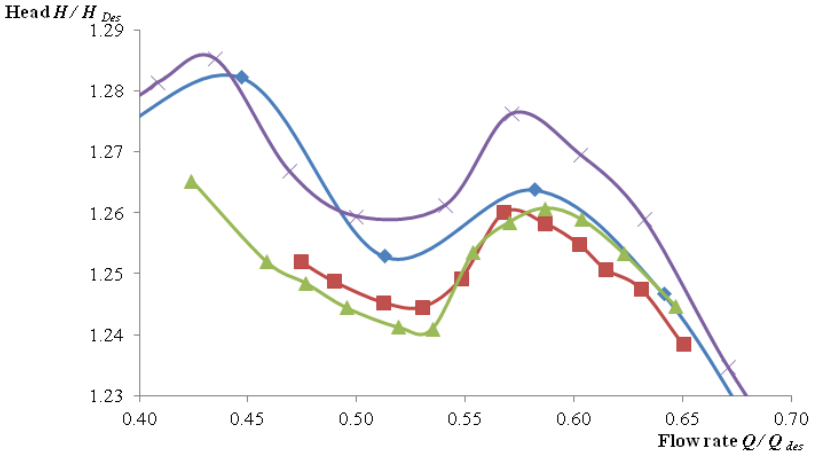

Fig. 3.1 *Q-H* curves by several test campaigns

Fig. 3.2 shows the detailed view of an arbitrary time sequence of pressure measurements on the mid span diffuser vane (as shown in Fig. 2.9) from full load to the part load. The signals in time domain are too complex to identify enough information on the unsteady flow patterns. Only at some flow rates during the flow rate interval of saddle-instability, the pressure pulsation corresponding to the impeller rotating frequency could be identified in this domain.

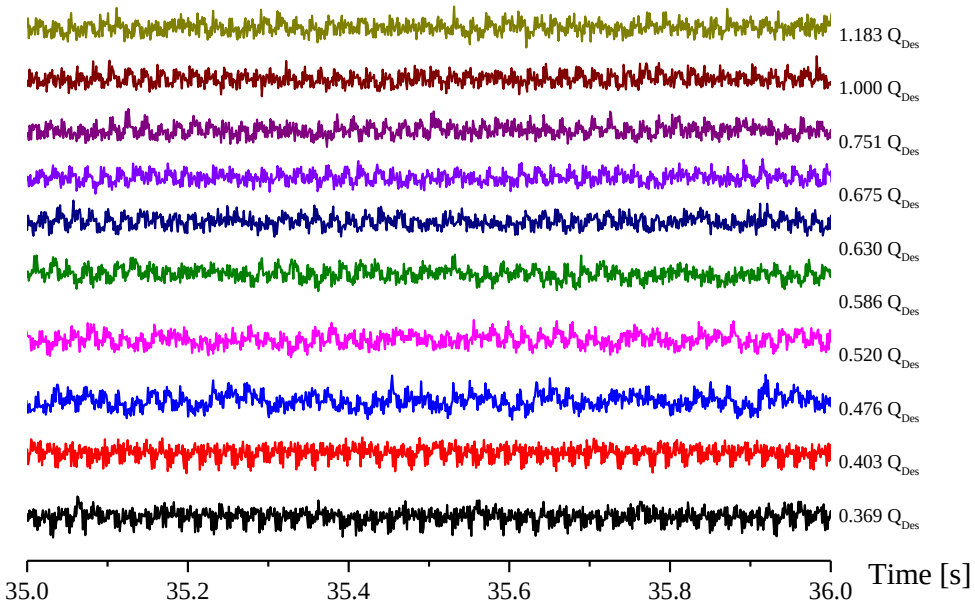

Fig.3.2 Pressure variation in the diffuser (transducer #6) versus the flow

Therefore, it is quite necessary to conduct the frequency analysis of the pressure signals, and the auto spectrums of one series tests of pressure via flow is shown in Fig.3.3. The spectra is mainly dominated by the blade passage frequency (BPF, St=1), the impeller frequency (St_{IPF} =0.143), and two other frequency peaks. The main one at St =0.6625 is observed in the flow interval Q/Q_{Des}= 0.369 to 1.183, the second one at St =0.335 is observed in the flow interval Q/Q_{Des}= 0.586 to 0.751.

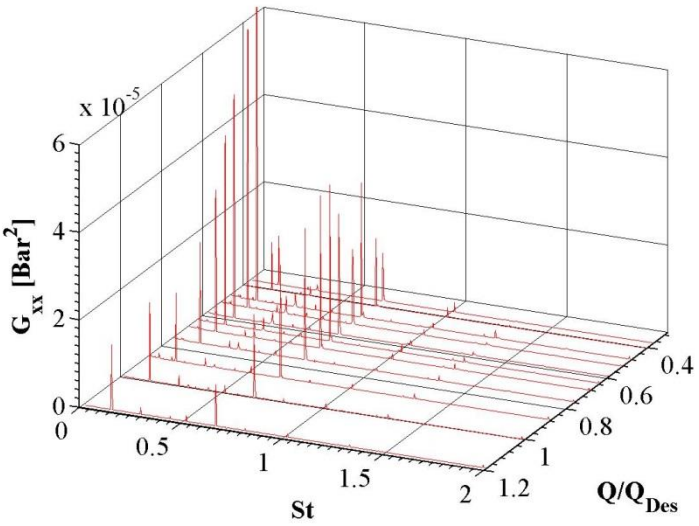

(a) Transducer # 5

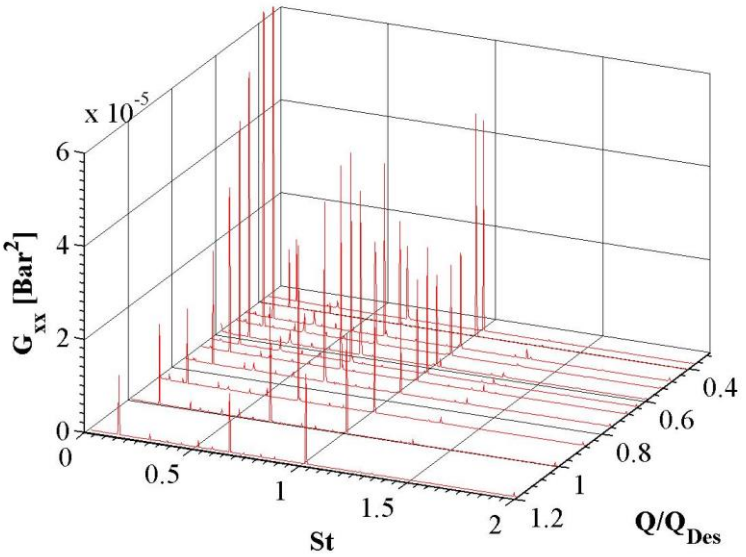

(b) Transducer # 6

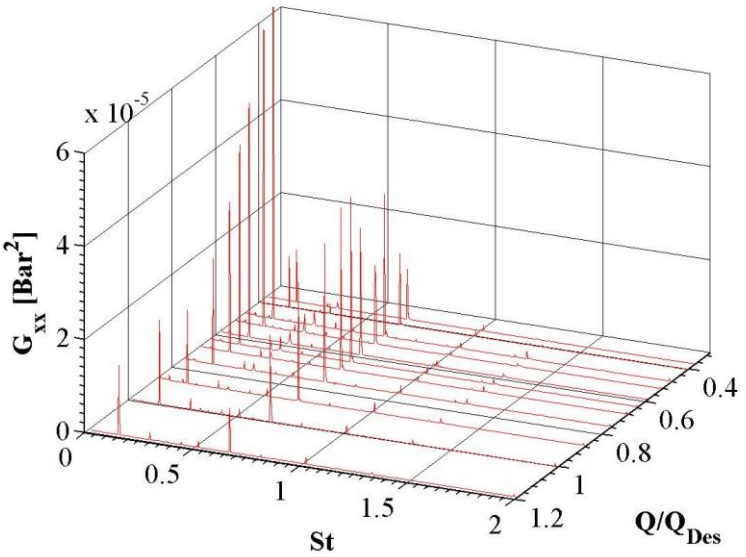

(c) Transducer # 11

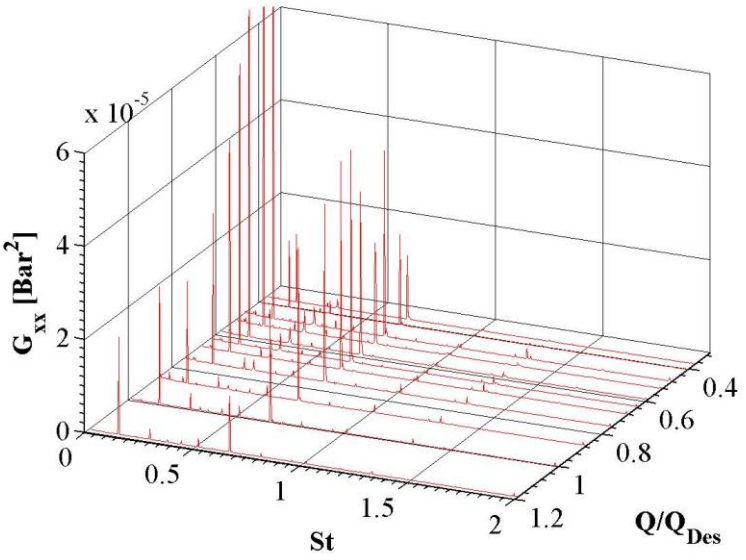

(d) Transducer # 12

Fig. 3.3 Power spectrum of pressure measured by the pressure transducers #5, 6, 11 and 12 in the diffuser vane

It could be found that the spectrum amplitude of pressure at St=0.143 and St=0.6625 both appear a decrease near $0.6Q_{Des.}$ This appearance is in agreement with the mean pressure variation at the exit of the impeller in the saddle-type instability region.

Moreover, in comparison to Fig.3.2, in the flow interval from 0.45 to $0.6Q_{Des}$, an obvious effect of impeller rotating frequency is both found in time and frequency domain: the periodic fluctuation of impeller rotating frequency could be identified in time sequence of pressure measurements in these flow rates, and the frequency amplitude increased most greatly.

As demonstrated by Akin and Rockwell (Akin and Rockwell 1994) the unsteady perturbations of the fluid in pump, generate non-linear interaction components in the power spectra. Therefore, how to identify the non-linear frequency components is essential to understand the unsteady perturbations inner pump.

In this study, the analysis of power spectrum of pressure reveals that near the BPF there are some unforced and forced unsteadiness. It includes deterministic forced unsteadiness related to impeller speed rotation and non-deterministic unforced unsteadiness, which is non-related to impeller speed rotation. There are two obviously frequency peaks at St=0.6625 and St=0.335, which are not the harmonic of BPF or the impeller rotating frequency. But it is not able to distinguish which one is the non-linear frequency component in the power spectrum. For this reason, the

bispectrum analysis was carried out the pressure measurements to identify the non-linear frequency components. Furthermore, in order to study the characteristics of the fluctuating pressures in time-frequency domain, the wavelet analysis was also performed.

3.1.1 First Series of Tests

3.1.1.1 Bispectrum of Pressure Signals

The power spectrums of first test campaign are shown in Fig. 3.3. Fig. 3.4 reveals the bispectrum of pressure signal form transducer #6 via indirect method. Table 3. 1 summarized the identified non-linear component frequencies by the topical transducers #3, 5 and 6 in diffuser vane at tested flow rates. It is indicated that the St= 0.6625 represents the pressure fluctuation of an unforced unsteadiness at both full and part load. The St= 0.335 as a fundamental frequency which only appears when the flow rate is nearly below critical value of saddle instability region Q/Q_{Des}= 0.7, and disappears when the flow rate is smaller than 0.5 Q_{Des}. The amplitude at St=0.335 in the other flow rates is a nonlinear interaction between the components BPF and St=0.6625.

The high order analysis highlights that in the saddle-instability zone, at the beginning of the unstable phenomenon, two kinds of unsteadiness (St=0.6625, St=0.335) exist and interact with each other. With the decreasing of flow rate, one unsteady structure (St= 0.335) disappeared.

Except these frequencies, also weak peaks were found in the power spectrum at some other frequencies, such as St= 0.335, 0.371, 0.518 and 0. 806.

The pressure peaks at these are caused by the interaction between impeller rotating frequency (St_R), blade pass frequency (St_{BPF}) and pressure pulsation's frequency (St_1=0.6625 or St_2=0.335). Table 3.2 reports some identified non-linear interaction components at full load condition.

In addition, a fundamental frequency around St= 0.005 was found at some flow rate. It may be associated with system fluctuations or a fundamental frequency of an unsteady structure. The reasons of this phenomenon will be analyzed in next section combining with the results of simulation.

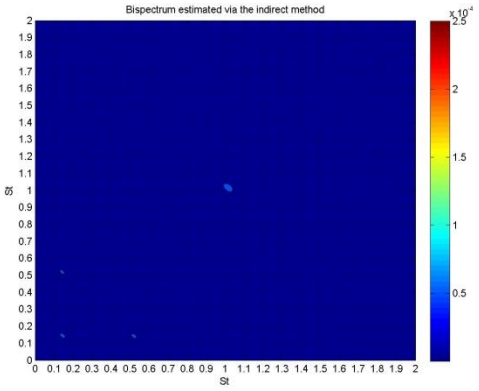

(a) 0.369 Q_{Des}

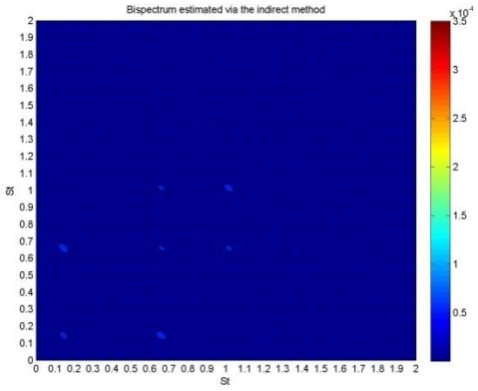

(b) 0.403 Q_{DES}

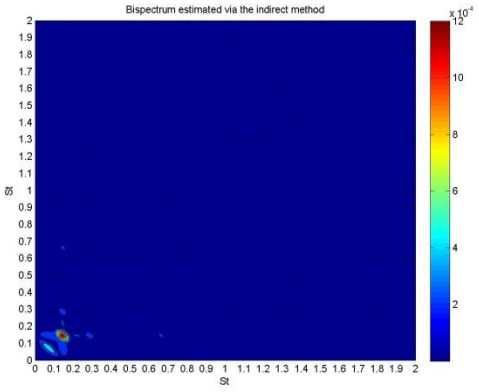

(c) 0.476 Q_{Des}

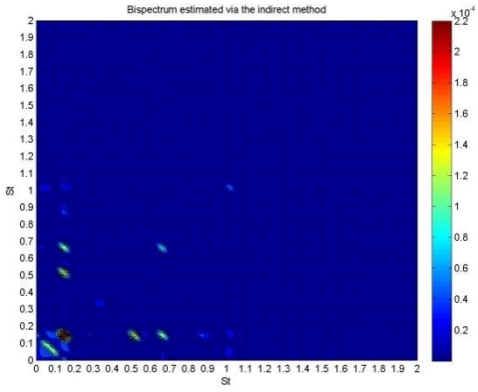

(d) 0.520 Q_{Des}

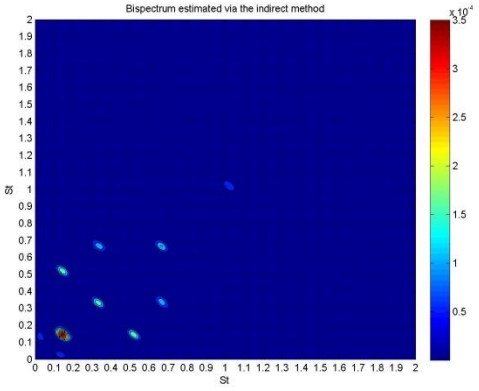

(e) 0.586 Q_{Des}

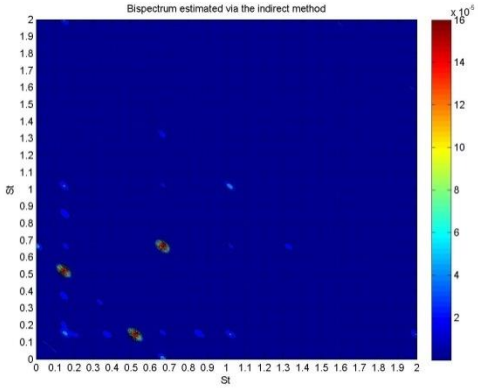

(f) 0.630 Q_{Des}

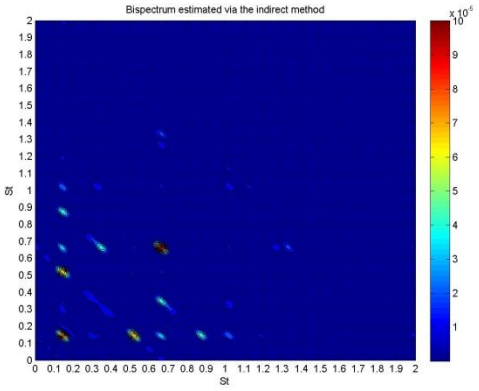

(g) 0.675 Q_{Des}

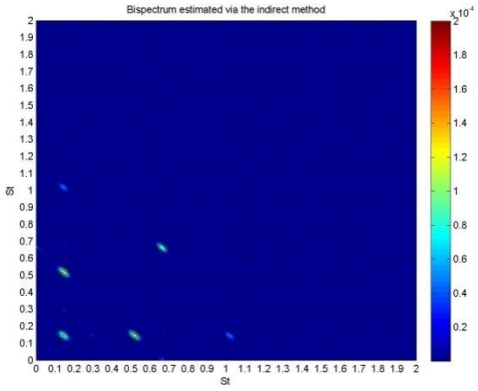

(h) 0.751 Q_{Des}

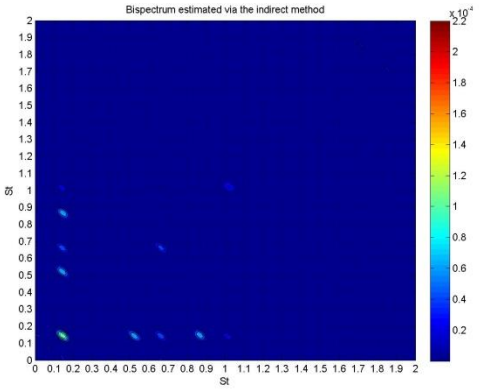

(i) 0.869 Q_{Des}

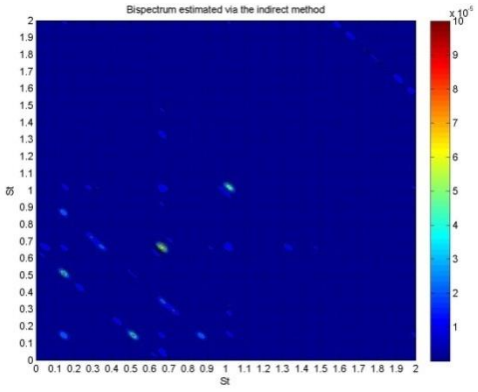

(j) 1.000 Q_{Des}

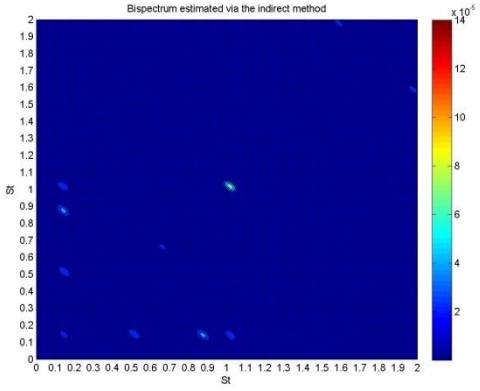

(k) 1.183 Q_{Des}

Fig. 3.4 Bispectrum of pressure signal form transducer #6 first campaign

Table 3.1 Identified non-linear frequency components

Q	Q/Q_{Des}	St = 0.335			St = 0.6635		
[l/s]	[-]	# 3	# 5	# 6	# 3	# 5	# 6
29.0306	0.369	-	-	-	-	-	-
31.7040	0.403	-	-	-	x	x	x
37.4335	0.476	-	-	-	-	-	-
40.9484	0.520	-	-	-	x	x	x
46.1515	0.586	x	x	x	x	x	x
49.596	0.630	x	x	x	x	x	x
53.1898	0.675	x	x	x	x	x	x
59.1733	0.751	-	-	-	x	x	x
68.4122	0.869	-	-	-	x	x	x
78.4801	0.997	-	-	-	x	x	x
93.1494	1.183	-	-	-	x	x	x

Table 3.2 Identified non-linear interaction components at full load

St	Non-linear components	St	Non-linear components
0.335	$7St_R$ -St_1 or St_{BPF} -St_1	0.518	St_1 -St_R
0.371	St_1 -$2St_R$	0.806	St_1 +St_R

3.1.1.2 Intensity of Pressure Fluctuation at St=0.6625 and St=0.335

In this section, the amplitudes of these two frequencies as the nonlinear frequency components are compared, and the value is zero when the corresponding frequency is not the fundamental one. In order to have a better comparison, the intensity of the amplitudes is expressed as dimensionless values by Eq.(3-1):

$$x_{Di} = \frac{x_i}{\bar{x}} \tag{3-1}$$

where x_i is the real amplitude, $\bar{x}$ is the mean value of this group and x_{Di} is dimensionless value.

Take the data form transducer #3, 5, and 6 as examples, Fig. 3.5 shows the intensity of the amplitude of the fundamental frequencies from these transducers. Quite similar features and trends from different transducers could be found in this figure, and they are outlined as bellow:

1. St=0.6625, as a fundamental frequency, could be found in most of testing operating conditions. The change trend is in accordance with the mean

pressure variation at the exit of the impeller versus the flow when the flow rate is greater than 0.6 Q_{Des}. Also a slump was detected around 0.6 Q_{Des} .

2. The fundamental frequency St=0.335 only appear in first part of saddle-instability region; furthermore, the variation goes up firstly and begins to go down around 0.6 $Q_{Des.}$ But the flow rate corresponding to the turning point is different from the flow rate of St=0.6625.

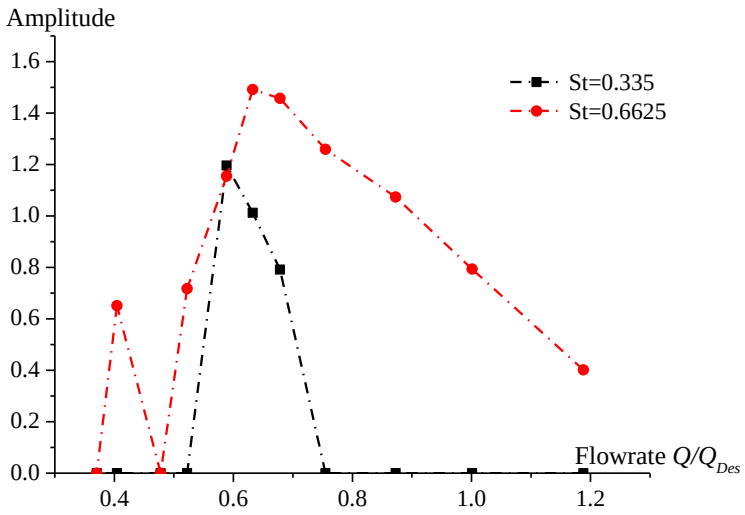

(a) Transducer #3

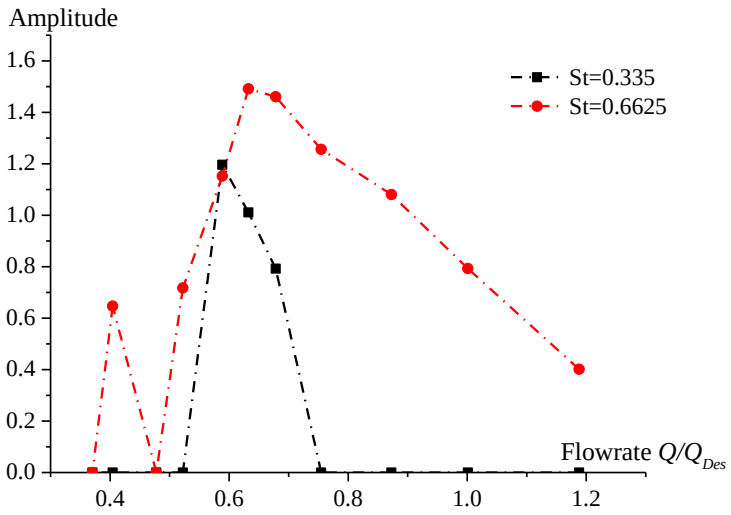

(b) Transducer #5

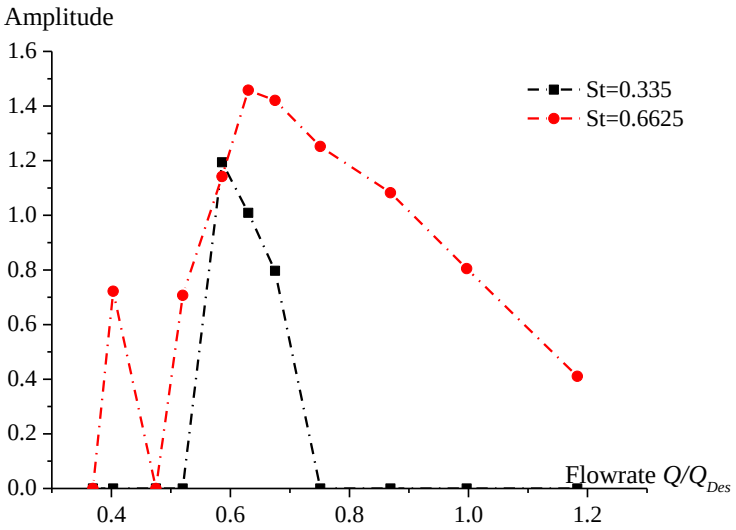

(c) Transducer #6

Fig.3.5 Comparison of the amplitudes of fundamental frequencies (Transducer #4, 5, 6)

3.1.1.3 Time-frequency Analysis

In order to identify and characterize the unsteady phenomena in time-frequency domain, the signals from all transducers were processed by the wavelet method. The wavelet magnitudes from transducer #6 are shown in Fig.3.6.

Besides the impeller rotating frequency, the blade passage frequency and their harmonics, the power spectra is characterized by two peaks at St=0.6625 and St=0.335.These peaks are also captured in the wavelet results, which highlight the unsteady characteristics (figure. 3.6).

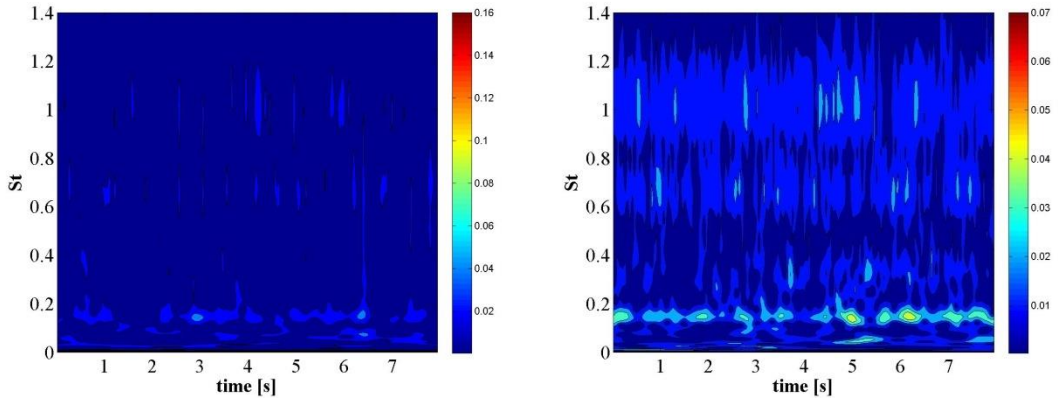

(a) 0.369Q_{Des} (b) 0.403 Q_{Des}

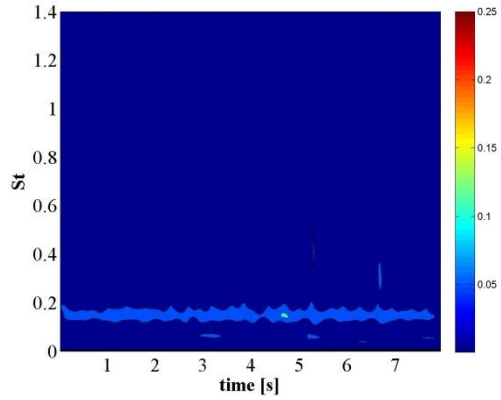

(c) 0.476 Q_{Des}

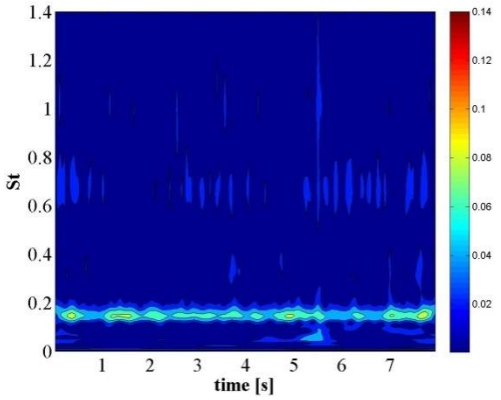

(d) 0.520 Q_{Des}

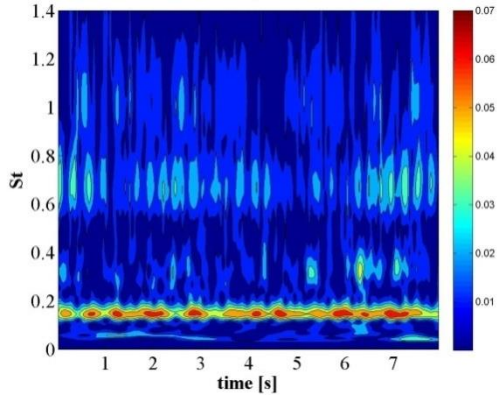

(e) 0.586 Q_{Des}

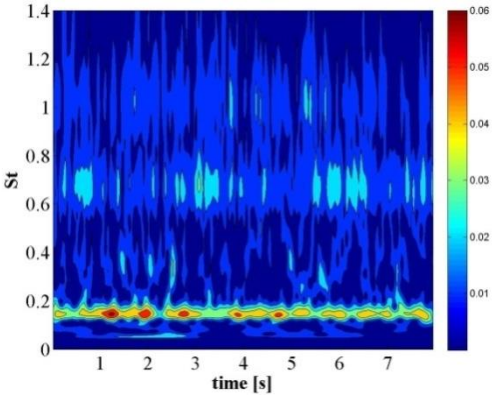

(f) 0.630 Q_{Des}

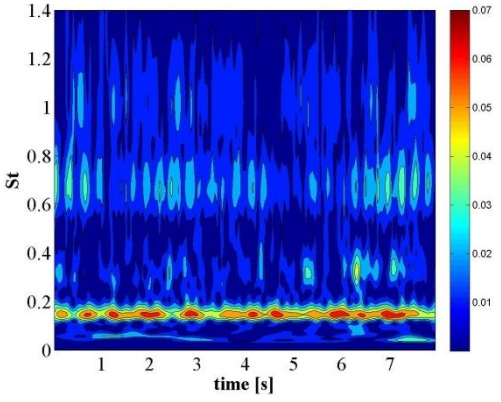

(g) 0.675 Q_{Des}

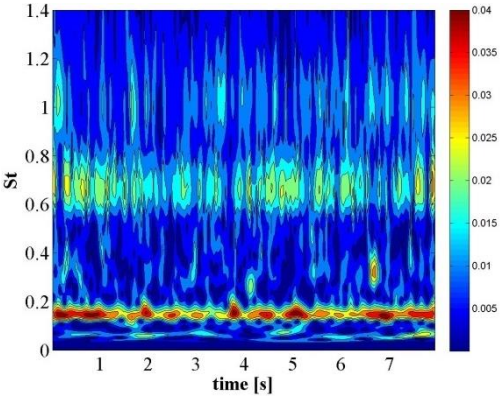

(h) 0.751 Q_{Des}

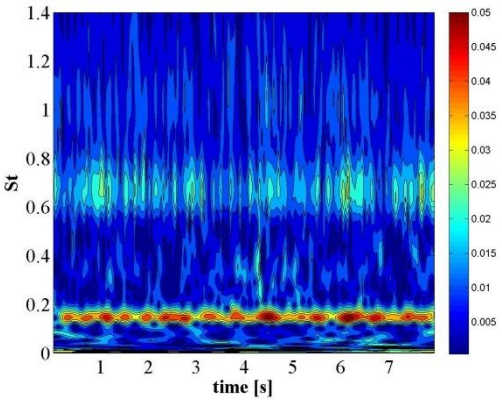

(i) 0.869 Q_{Des}

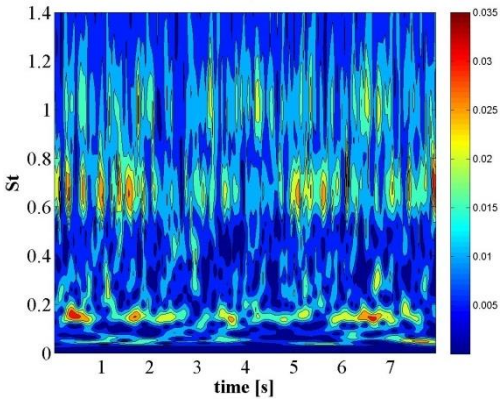

(j) 1.000 Q_{Des}

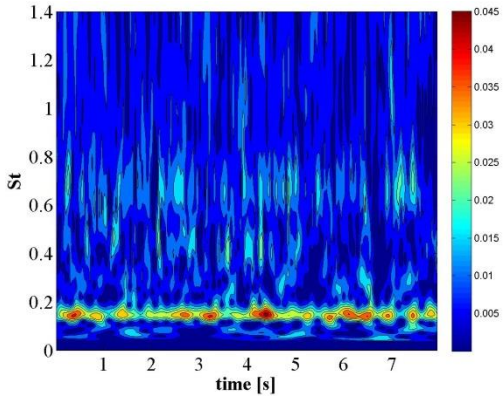

(k) 1.183 Q_{Des}

Fig.3.6 Wavelet magnitude |Wn| of the pressure signal (transducer # 6)

It is worth mentioning that the magnitude of these frequencies display regular fluctuations over time. It could be identified that the fluctuation period of impeller rotating frequency is about 2.5Hz (St=0.0357). The exact period of the other frequency fails to be obtained due to the insufficient evidence in the pictures.

In addition, in order to highlight the correlations of the fundamental frequencies between two different test locations in saddle instability region, a cross wavelet between two transducers has been done. Fig. 3.7 shows the cross wavelet magnitude |Wn| of the pressure signal (transducer #5 and 6) at some flow rates in this region. In this figure, the pictures are composed of two parts: phase and intensity, which are represented, by arrows and colour, respectively. The cross-correlation of subtonal components (St=0.6625 and St=0.143) exists periodically in all listed flow rates. At the flow rate of 0.630 Q_{Des}, the frequency St=0.335 appears to be an obvious pulsation. With the further reduction of the flow rate, the effect of St=0.335 progressively weakens.

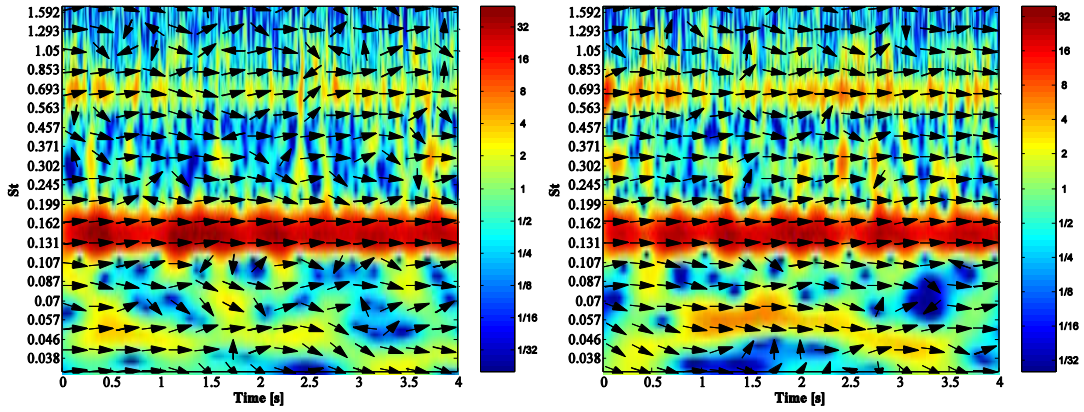

(a) 0.520 Q_{Des} (b) 0.586 Q_{Des}

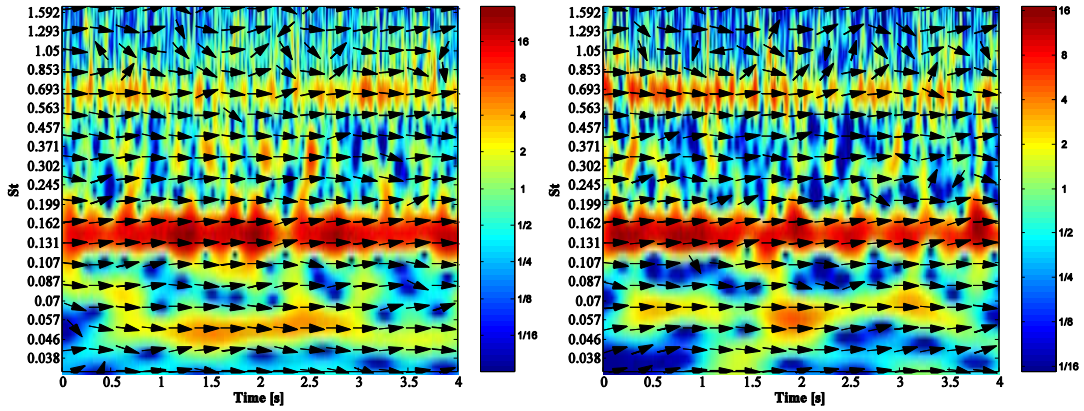

(c) 0.630 Q_{Des} (d) 0.675 Q_{Des}

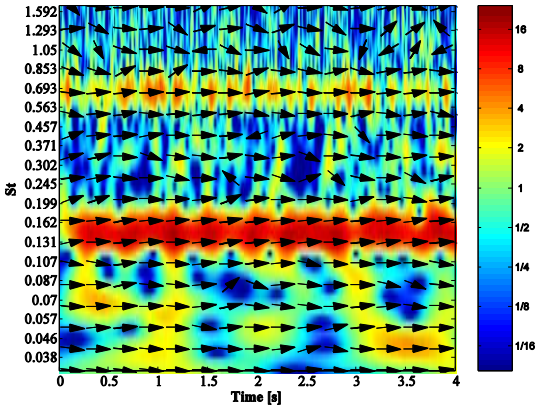

(e) 0.751 Q_{Des}

Fig.3.7 Cross wavelet magnitude |Wn| of the pressure signal in the diffuser vane

3.1.2 Second Series of Tests

3.1.2.1 Frequency Analysis of Pressure Signals

In the second campaign, the flow rate interval for the test is from 0.424 to 0.623 Q_{Des}. The auto power spectrum analysis was performed for these pressure signals. The results of transducer #5, 6, 11 and 12 are shown in Fig.3.8. The spectrum appears obvious peaks still at the frequency of St=0.335and St=0.6625 throughout all the test range, and both of the values of these frequencies turn down near 0.6 Q_{Des}.

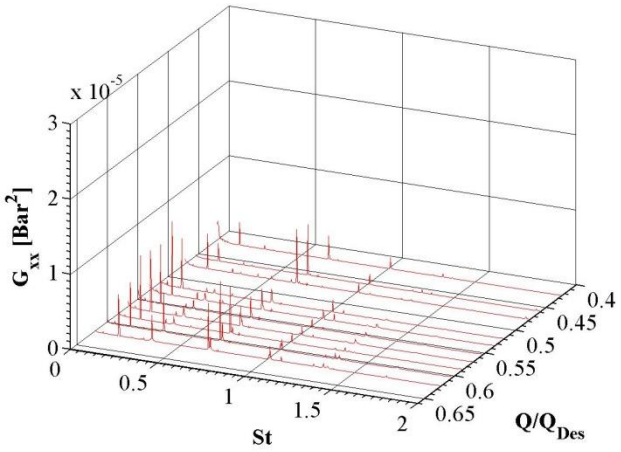

(a) Transducers # 5

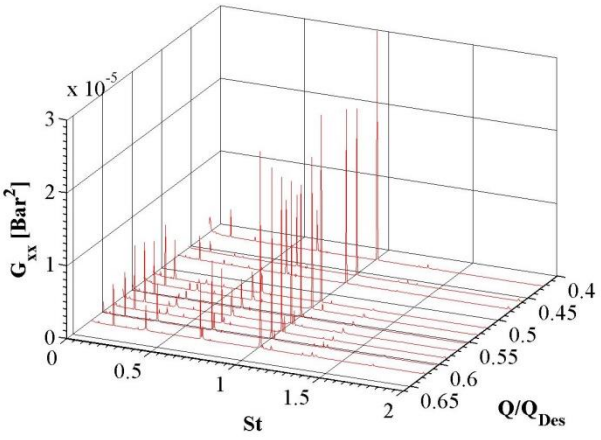

(b) Transducer # 6

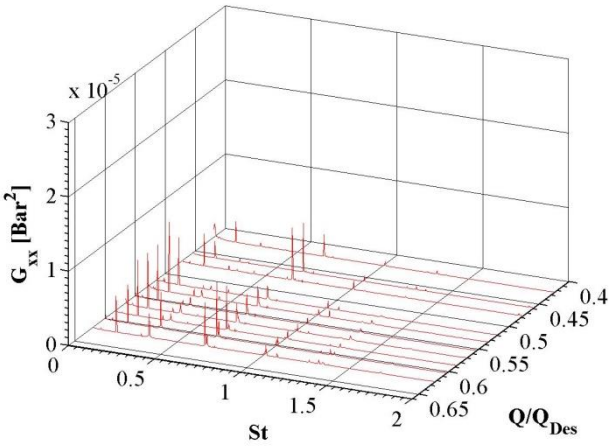

(c) Transducer # 11

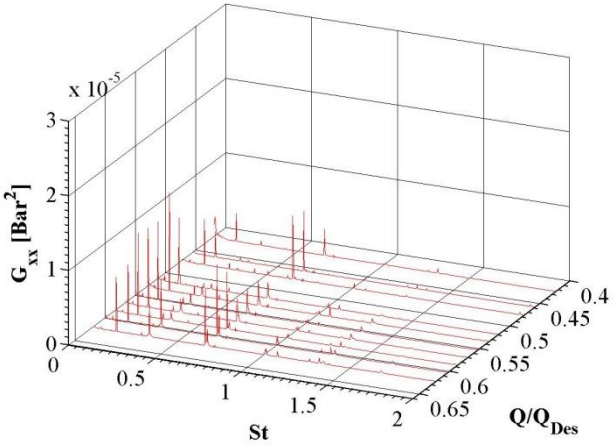

(d) Transducer # 12

Fig.3.8 Power spectrum of pressure measured by the pressure transducer #5, 6, 11 and 12 in the diffuser vane

3.1.2.2 Bispectrum Analysis of Pressure Signals

The bispectrum analysis of pressure signal from the second campaign was done, and Fig.3.9 was the bispectrum of pressure signal form transducer #6. Table 3.3 lists the identified non-linear frequency components at each flow rate.

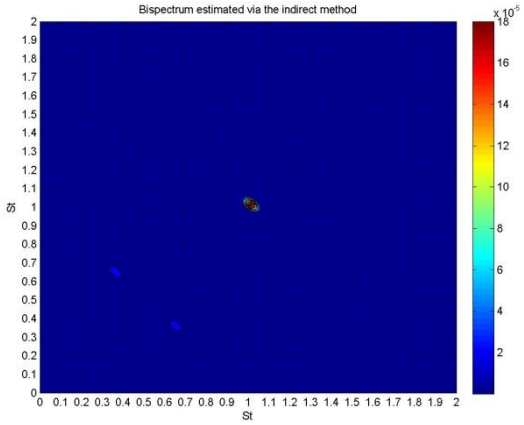

(a) 0.424 Q_{Des}

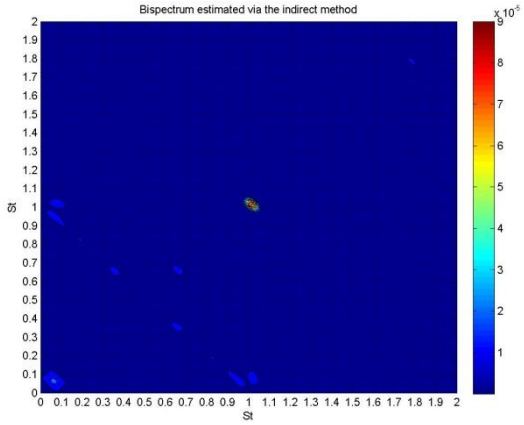

(b) 0.458 Q_{Des}

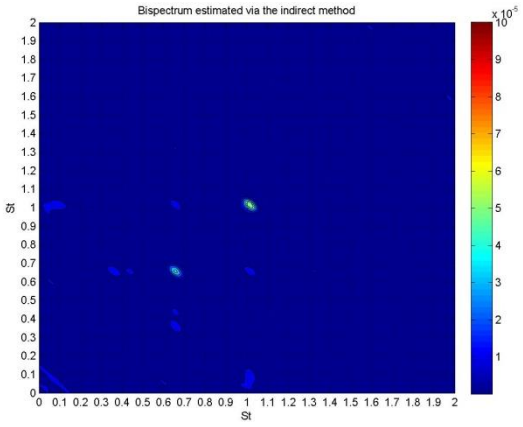

(b) 0.477 Q_{Des}

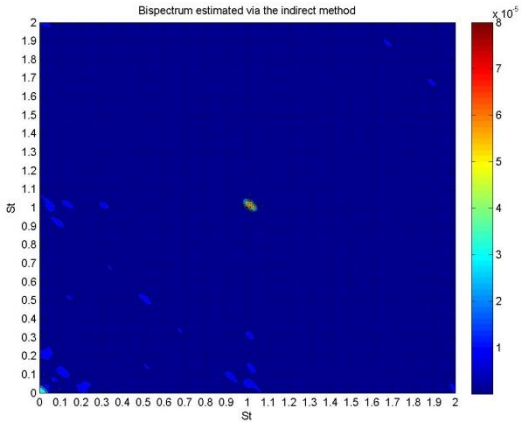

(d) 0.519 Q_{Des}

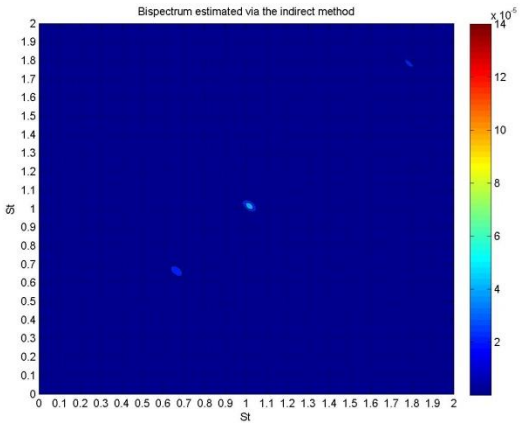

(d) 0.535 Q_{Des}

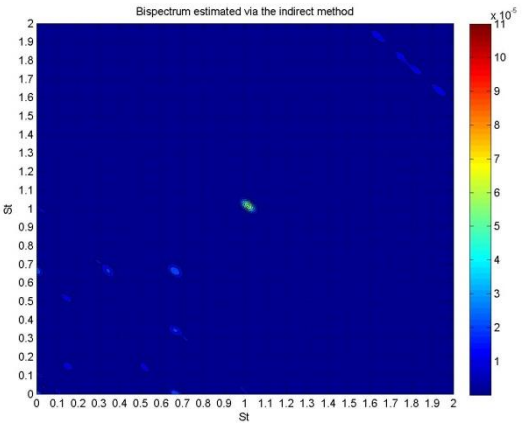

(f) 0.554 Q_{Des}

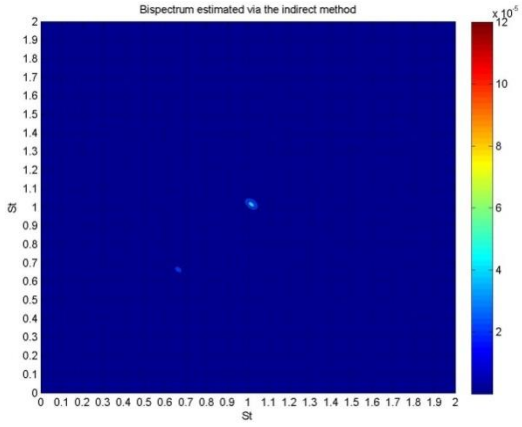

(e) 0.570 Q_{Des}

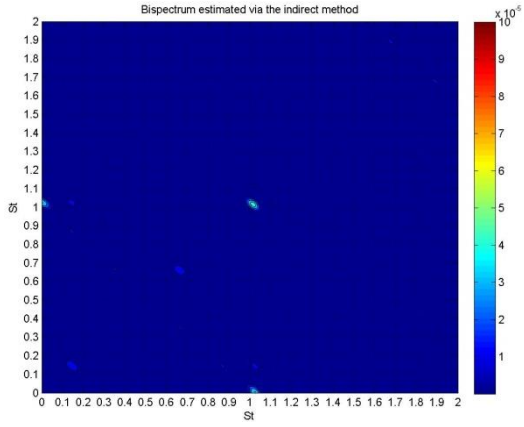

(h) 0.587 Q_{Des}

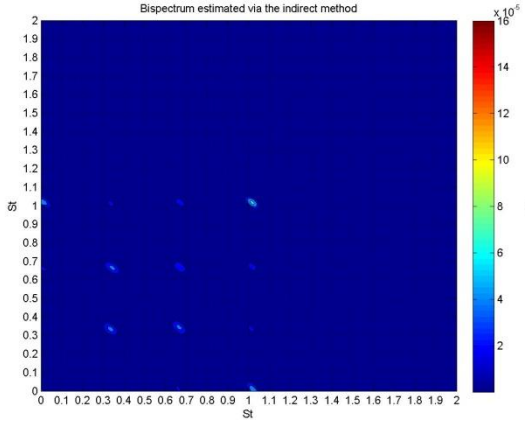

(i) 0.603 Q_{Des}

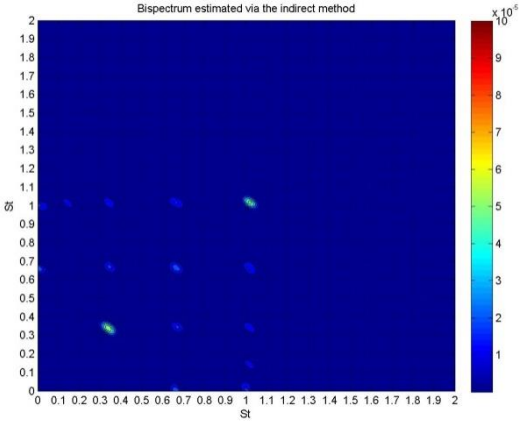

(j) 0.623 Q_{Des}

Fig. 3.9 Bispectrum of pressure signal form transducer #6

Table 3.3 Identified non-linear frequency components

Q	Q/Q_{DES}	St = 0.335			St = 0.6635		
[l/s]	[-]	# 3	# 5	# 6	# 3	# 5	# 6
33.23	0.424	-	-	-	-	-	-
35.94	0.458	-	-	-	x	x	x
37.36	0.477	-	-	-	x	x	x
40.69	0.519	-	-	-	-	-	-
41.92	0.535	-	-	-	x	x	x
43.40	0.554	-	-	-	x	x	x
44.69	0.570	-	-	-	x	x	x
45.99	0.587	-	-	-	x	x	x
47.29	0.603	x	x	x	x	x	x
48.82	0.623	x	x	x	x	x	x

The results show that, St=0.6625 and St=0.335 are both non-linear frequencies in some flow rates in the saddle instability region, and they are consistent with the first test results.

3.1.2.3 Intensity of Pressure Fluctuation at St=0.6625 and St=0.335

The intensity of the nonlinear frequency components is analysed in this section. Fig. 3.10 shows the intensity of the fundamental frequencies at different flow rates form transducer # 3, 5, and 6. In addition, the trend is quite similar to the first campaign: as a fundamental frequency, St=0.6625 could be found in most of testing operating conditions; in the saddle instability region, two fundamental frequencies of St=0.6625 and St=0.335 both appear and drop near 0.6 Q_{Des}.

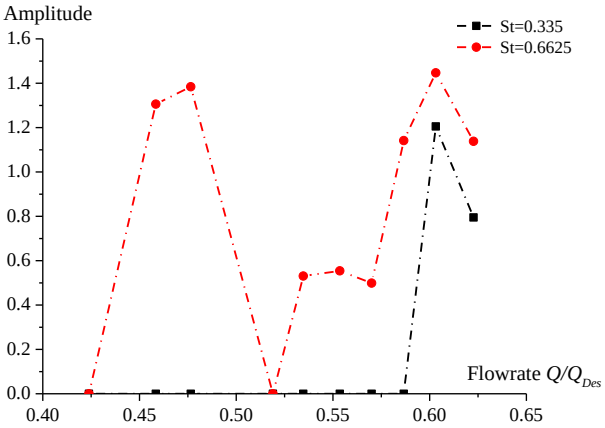

(a) Transducer #3

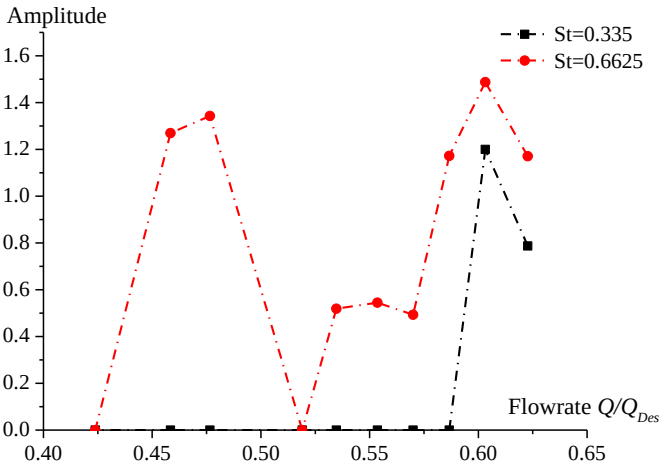

(b) Transducer #5

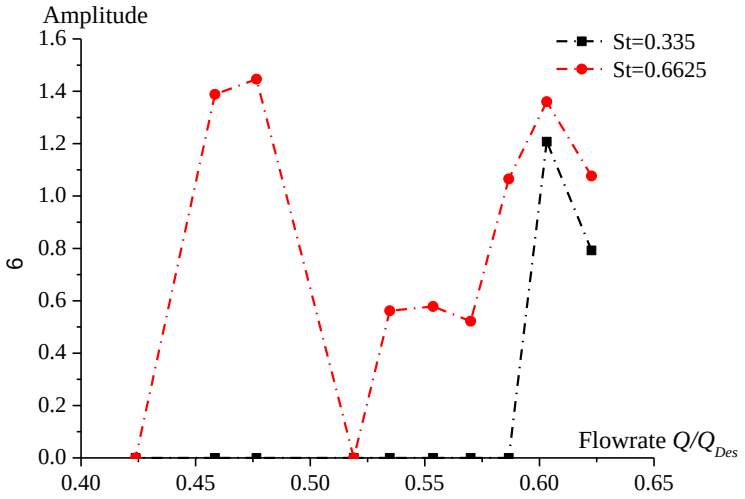

(b) Transducer #6

Fig. 3.10 Comparison of the amplitudes of fundamental frequencies (Transducer #3, 5, 6)

3.1.2.4 Time-frequency Analysis of Pressure Signals

The time-frequency analysis of pressure signals from the second experimental campaign was carried out. The time-frequency characteristics of the pressure signals in the saddle instability region were shown in Fig.3.11 and 3.12. The pressure signals were processed by wavelet and cross wavelet, respectively. In these pictures, the fundamental frequencies of St=0.6625 and St=0.335 fluctuate with time.

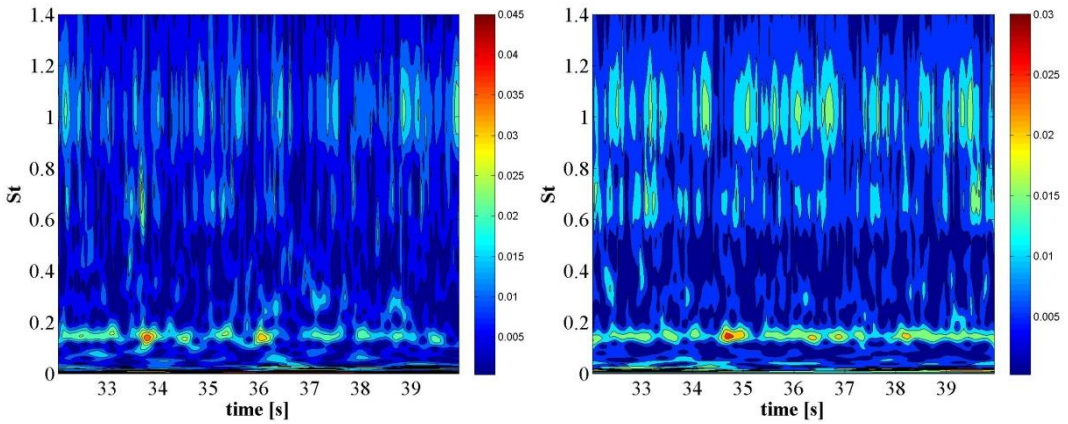

(a) 0.570 Q_{Des} (b) 0.587 Q_{Des}

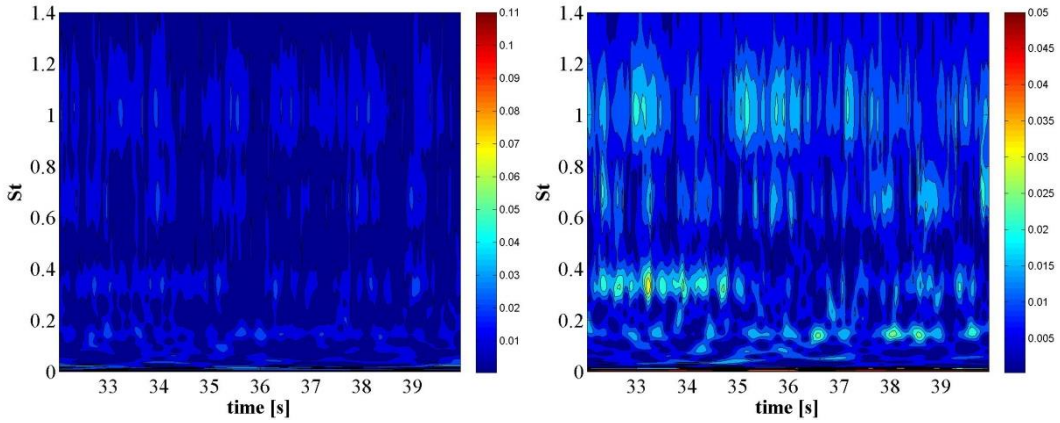

(c) 0.603 Q_{Des} (d) 0.623 Q_{Des}

Fig.3.11Wavelet magnitude |Wn| of the pressure signal (transducer # 6)

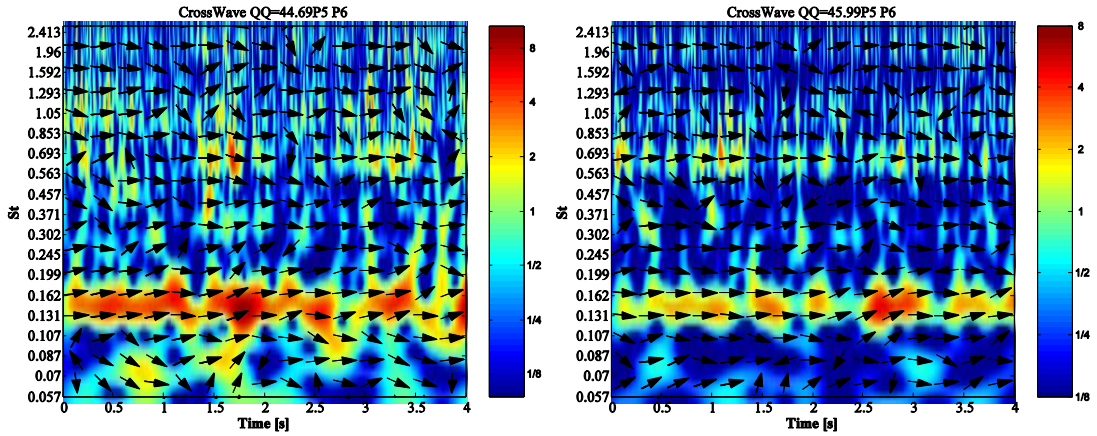

(a) 0.570 Q_{Des} (b) 0.587 Q_{Des}

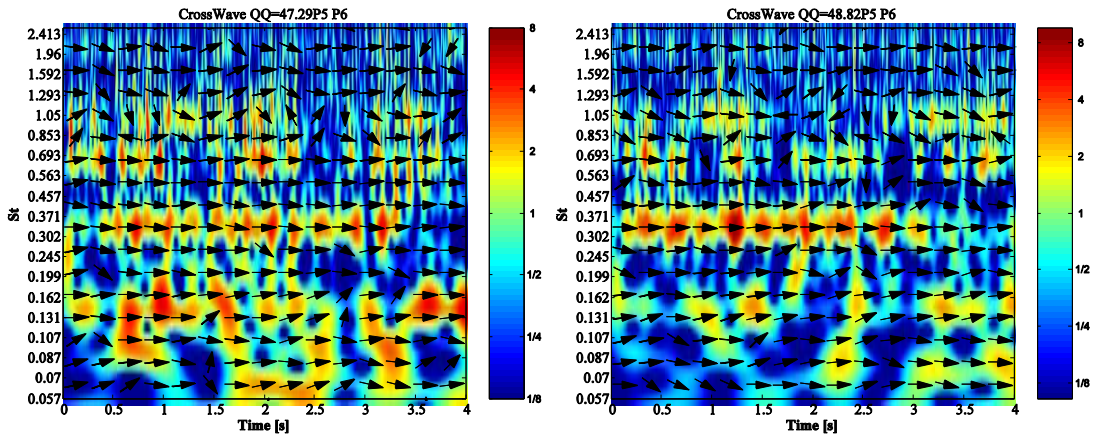

(c) 0.603 Q_{Des} (d) 0.623 Q_{Des}

Fig.3.12 Cross wavelet magnitude |Wn| of the pressure signal in the diffuser vane

3.1.3 Identification of Rotating Stall by Pressure Signal

In order to identify whether the pressure fluctuations have the circular rotation, the work was done as bellow:

First step, the original pressure signal was filtered by the band-pass filter, which based on the frequency of the interested pressure fluctuation.

Second, the filtered signal was divided into many segments by the same time interval, which is equal to the time of 1 impeller revolution.

Then, an instantaneous image of the time-pressure fluctuation could be drawn like Fig.3.13 (a), which is based on these pressure segments. In this picture, the vertical axis represents the circumferential angle of the impeller, and the horizontal axis is the sampling time of pressure on diffuser vane.

Fig. 3.13 (a) presents the temporal wave obtained by the pressure signals filtered by band-pass (St=0.6-0.7) over 20 impeller revolutions (equals to 2s) at full load. The filtered pressure signals reveal high-pressure amplitude which appears 4 or 5 times every impeller revolution and propagates forward to the rotation of the impeller. This instability is corresponding to the peak of spectrum at St=0.6625 (see Fig. 3.13 (b)).

It could be found in the figure that the stall rotates slightly faster than the impeller. Its revolution rate could be estimated by the slop $k_{1,}$ of the black dotted lines (in Fig.3.13 (a)) using the following relation:

$$\begin{aligned} t_{delay\_F} &= 360 \cdot \left|\tan k_1\right| \\ f_{Rs\_F} &= \frac{t_{delay\_F} \cdot n - 1}{t_{delay\_F}} \\ m_F &= \frac{\mathrm{St_F} \cdot BPF}{f_{Rs\_F}} \end{aligned} \tag{3-2}$$

where t_{delay_F} is the delay time of these stalls period, n is the speed of the impeller, f_{Rs_F} is the frequency of rotating stall, m_F is the number of stall. Therefore, for the frequency St=0.6624, the t_{delay_F} is about 1.7s, the f_{Rs_F} is 9.41Hz ((St=0.134), and the number of stall m_F=5.

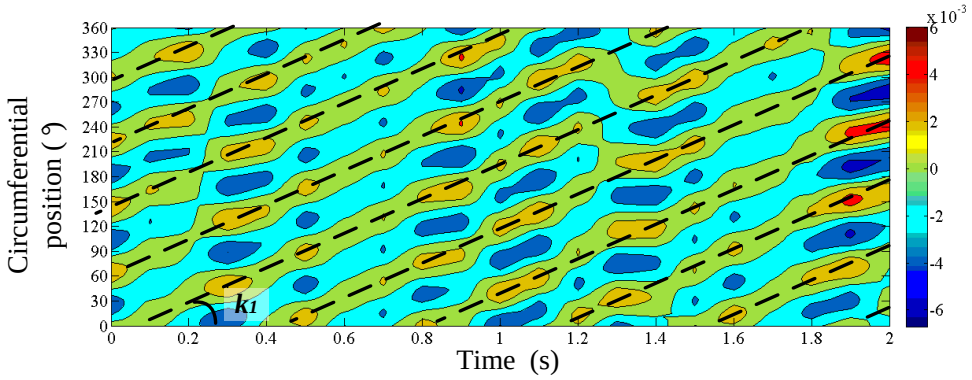

(a) Time history of band-pass filtered pressure signal St=0.6-0.7

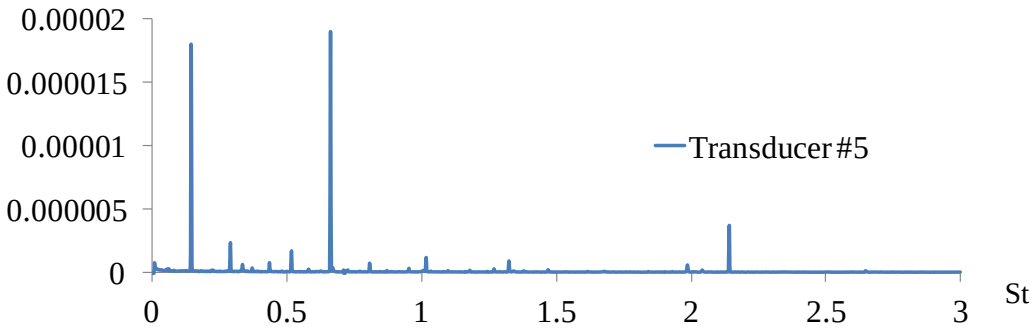

(b) Auto spectrum

Fig.3.13 Pressure signal at design flow rate (transducer #5)

Based on the time and frequency domain analysis of last section, in the saddle-instability region, there are another non-linear frequency components St=0.335 except St=0.6625. In this case, the analysis of pressure signal at the flow rate of 0.623 Q_{Des} obtained by the first campaign was listed in Fig 3.14 (a) presents the time wave of the pressure signal filtered by band-pass St=0.6-0.7 and Fig 3.14 (b) presents time history of the signal filtered by band-pass St=0.3-0.35.

Compared with Fig. 3.13 (a), it is indicated that the propagating characteristics at St=0.6625 at this flow rate is quite similar to full load condition. The disturbance at St=0.6625 still have 5 cells, and the corresponding frequency is 9.41Hz ((St=0.134).

Additionally, as shown in this figure, the pressure fluctuation of St=0.335 rotates with the impeller like the pressure fluctuation of St=0.6625. It could be found that the rotating speed of the distribution of St=0.335 is smaller than the speed of impeller, and the speed could be calculated by Eq.(3-3).

$$t_{ahead\_s} = 360 \cdot \left|\tan k_2\right|$$
$$f_{Rs\_s} = \frac{t_{ahead\_s} \cdot n + 1}{t_{ahead\_s}} \tag{3-3}$$
$$m_S = \frac{St_S \cdot BPF}{f_{Rs\_S}}$$

where k_2 is the slop of the black dotted lines (in Fig.3.14(b)), t_{ahead_S} is the ahead time of these distribution period which equal to 0.62s, f_{Rs_F} is the frequency of the stall. The value is 11.61 Hz ((St=0.166), and therefore the number of these stalls m_s is 2.

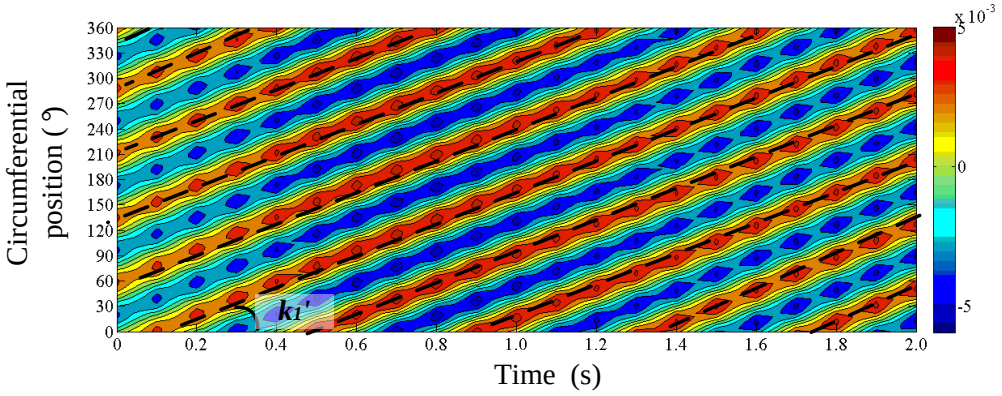

(a) Time history of band-pass filtered pressure signal St=0.6-0.7

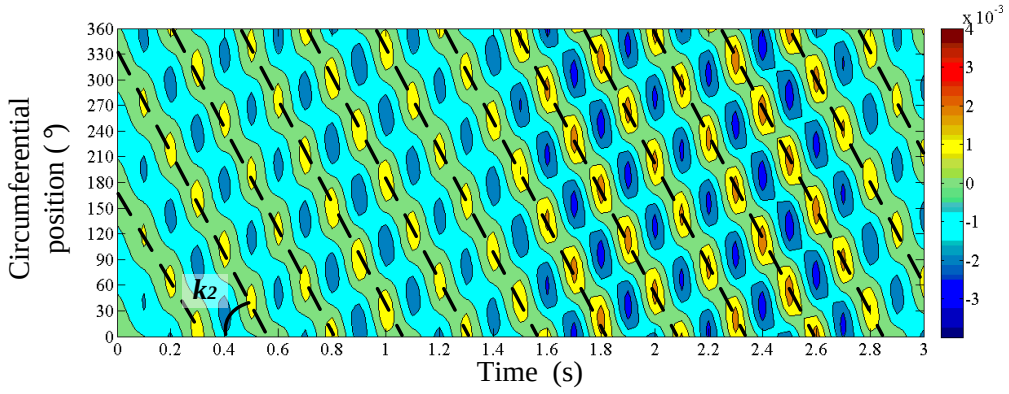

(b) Time history of band-pass filtered pressure signal St=0.3-0.35

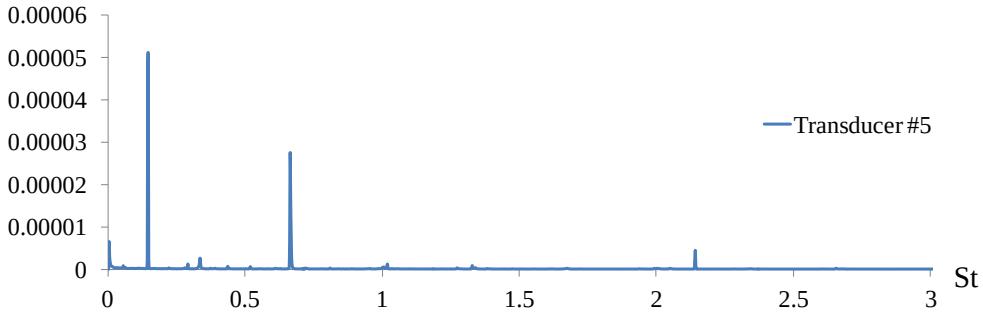

(c) Auto spectrum of original pressure signal

Fig.3.14 Pressure signal at 0.623 Q_{Des} (transducer #5)

Therefore, by the analysis above, it is concluded that the pressure fluctuation of St=0.6625 is caused by a kind of rotating disturbance with 5 rotating cells and rotating frequency of St=0.134. Furthermore, the pressure fluctuation of St=0.335, which is detected at the first part of saddle-instability region, is also caused by a kind of rotating disturbance. It is comprised of two rotating cells, and the rotating frequency is St=0.166.

3.2 High-Speed Flow Visualization

Two different unsteady patterns were detected by the pressure analysis. In order to understand the development of these unsteady flow structures, the analysis of high-speed flow visualizations was carried out. The visual range was zoomed in flow passage between the vanes of diffuser and return channel.

In the analysis of the frames, it is assumed that the air bubbles fairly follow the streamlines with almost no effect on the flow itself. The flow visualizations highlight that the recirculation regions are present in the U-turn return channel at design and lower flow rate.

At full load condition, inside the diffuser vane channel, the trajectory of air bubbles from D03 is straight with a quite negligible longitudinally unsteadiness (Fig. 3.15(a)). In the return vane channel, the bubbles, which blew out of the R16, were rapidly scattered forming puffs of bubbles. The bubbles flow pattern was close to the diffuser suction side (Fig. 3.15(b)), and the frequency of the bubbles clouds was consistent with St = 0.6625. Moreover, a reverse flow volume was present in the corner between the vane suction side and the U-Turn hub (central region in Fig. 3.15(b)). The bubbles, which are blown out of the R16 hole, were partially absorbed by the reverse flow and moved inside it with an ellipsoidal path. This recirculation,

showed a pulsating oscillation and discard of the bubbles equal to the impeller rotating frequency (St=0.143).

With the reduction of the flow rate, at the beginning, the bubbles moved along the diffuser blade surface with random slowing down and restarting (Fig.3.16 b and c) as the black line shown in Fig. 3.17. With a further reduction of the flow rate, the frequency of the pulsations increased, a flow separation began to appear around the trailing edge (Fig. 3.17), and gradually extended along the diffuser vane as sketched by the red line in Fig. 3.17.

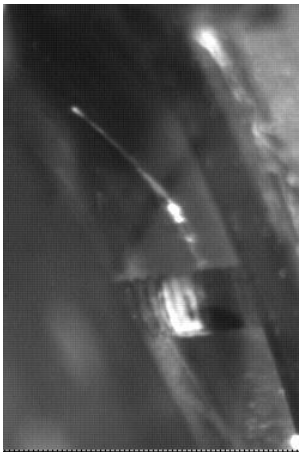

(a) Trajectory of air bubbles from P3 hole in diffuser

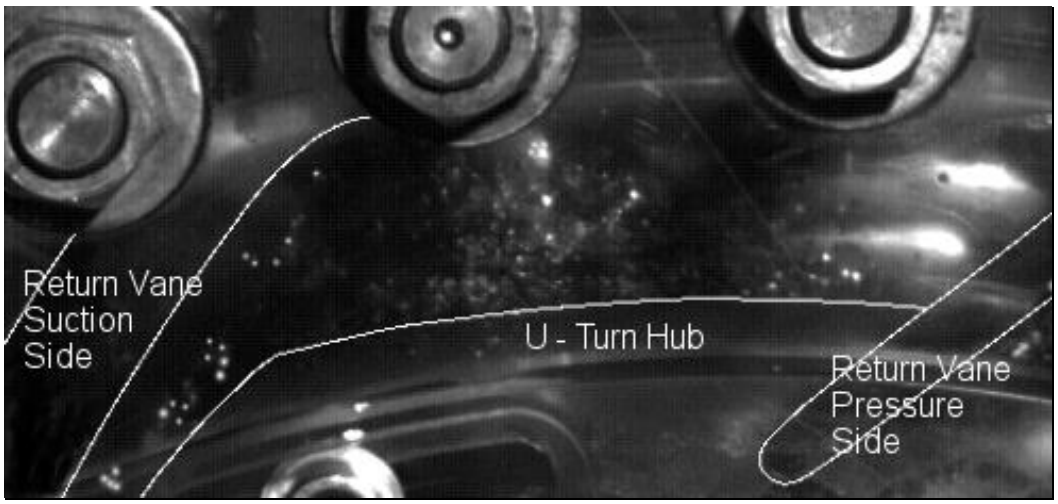

(b) Trajectory of air bubbles from P16 hole in return channel

Fig. 3.15 Frames obtained by high speed camera at design flow rate in the diffuser and return channel at design flow rate

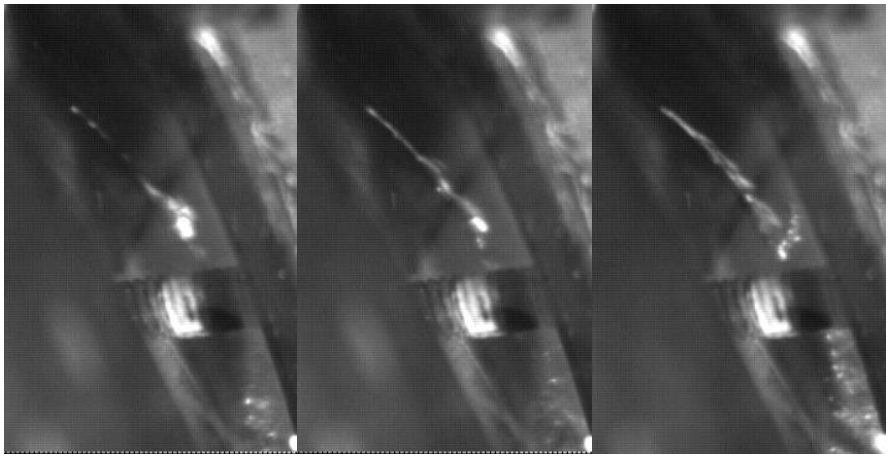

(a) Q/Q_{Des}= 0.90 (b) Q/Q_{Des}= 0.85 (c)Q/Q_{Des}= 0.80

Fig. 3.16 Frames obtained by high speed camera in the diffuser at flow rates from 0.9 to 0.8Q_{Des}

When the flow rate decreased below the design flow rate, the back flow volume in the return channel moved along the suction side, extending towards the back side direction. The unsteady pattern in return channel strengthened emphasizing its characteristic frequency St= 0.6625 with the flow rate decreasing. Moreover, the bubbles, which flew into the diffuser, became slightly unstable in the crosswise direction.

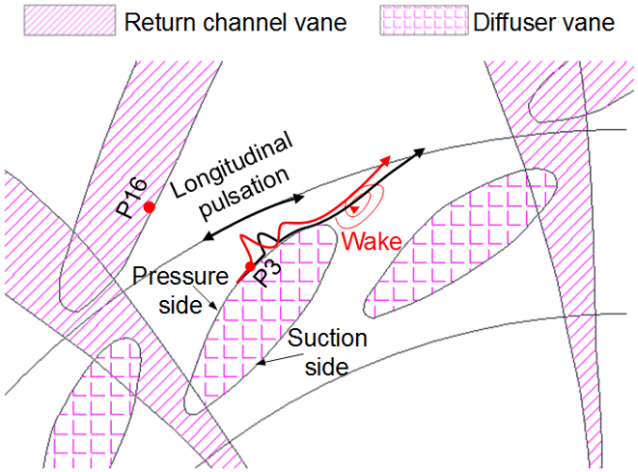

Fig.3.17 Sketch map of the bubbles tracks in diffuser.

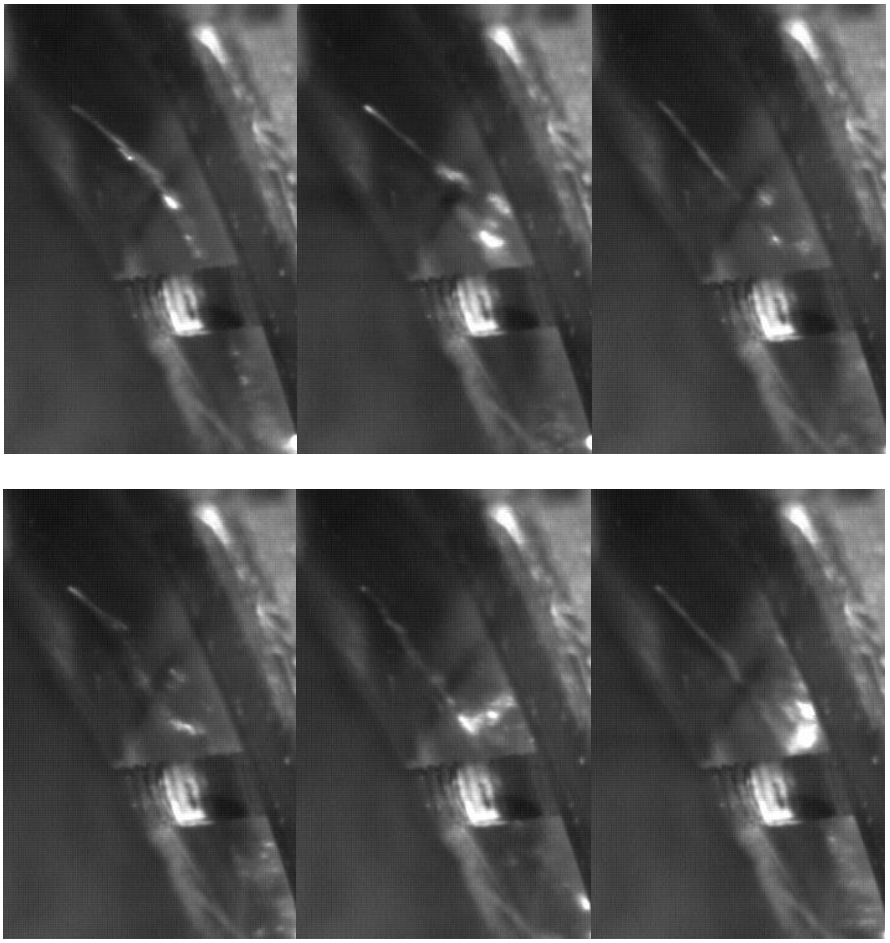

Fig. 3.18 Frames sequence obtained by high speed camera at 0.63 Q/QDes in the diffuser.

At lower flow rate the flow field into the diffuser manifested a full three-dimensional flow structure. At about 0.63 Q_{Des}, a crosswise unstable disturbance appeared, shown by the frames sequence in Fig. 3.18. The air bubbles were periodically spread out axially on the diffuser blade. This disturbance, which is related to the boundary layer separation, stalls in the diffuser and is noticed with a frequency very close to St=0.335.

Furthermore, an intermittent spiral trajectory started to appear at the inlet of return channels, which is shown by the frames sequence in Fig. 3.19. In the same sequence three groups of bubbles are marked to help to identify the complex 3D trajectory. This macro vortices is consistent with the progressive periodic partial choke of the diffuser vane. (A, B and C represent a reverse flow volume, spiral trajectory and bubbles clouds, respectively)

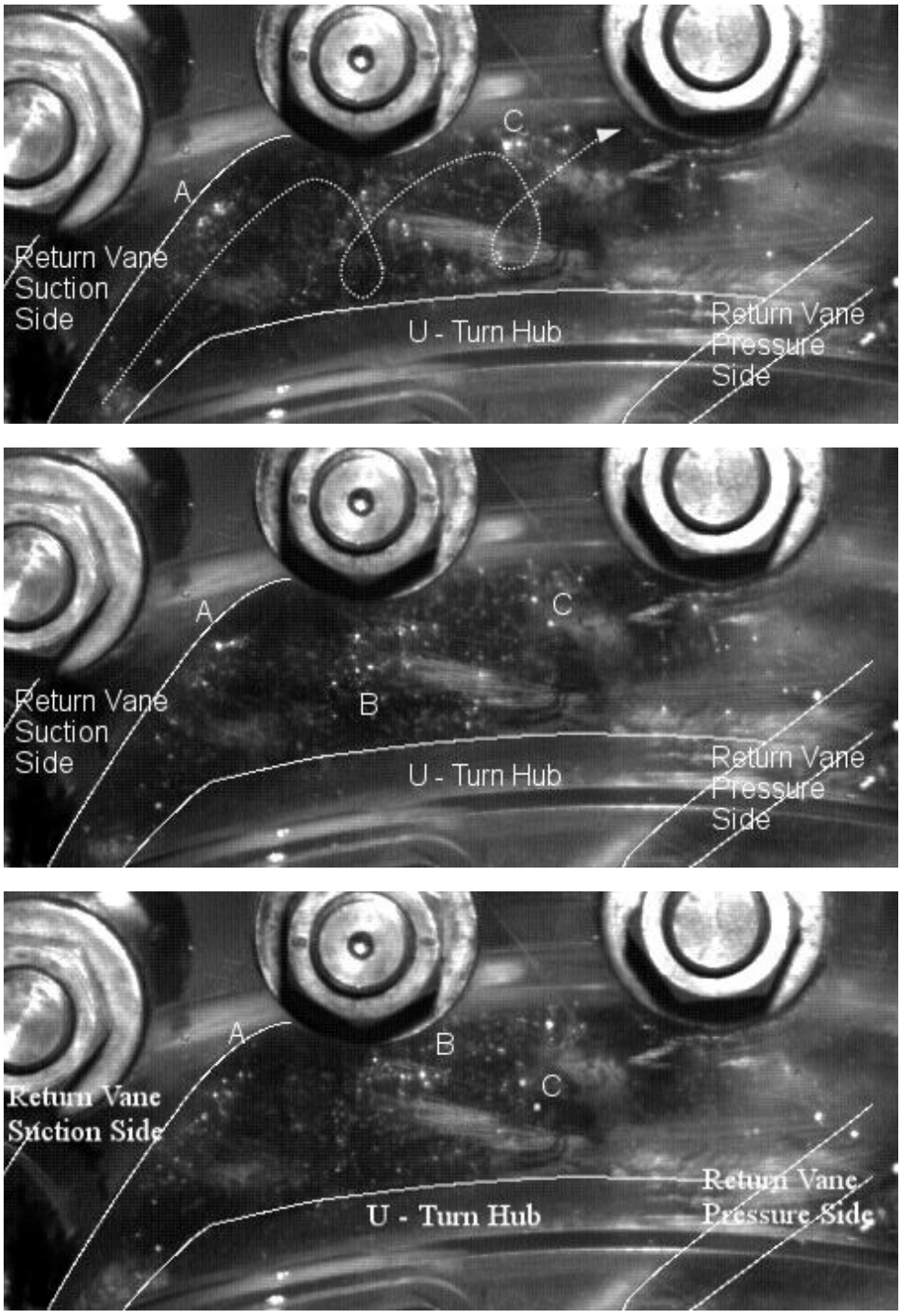

Fig. 3.19 Frames obtained by high speed camera at 0.63 Q_{Des} in the return channel

With a further flow rate reduction, the flow became more unstable. At 0.59 Q_{Des}, as shown in Fig. 3.20, the air injected through the D03 of the diffuser was found periodically to move back toward the impeller. The front side of return channel close to the hub was occupied by the same vortex shown in Fig. 3.19. Moreover, when the diffuser was stalled the air, pumped out of the hole number R04 on the return vane

suction side, moved from the back side of the return channel toward the front side, mixed with the flow in the front side and came back to the outlet (Fig. 3.21).

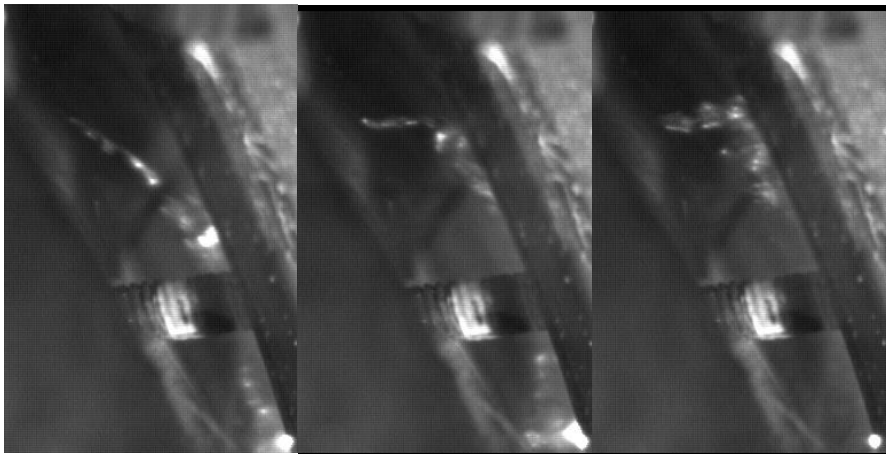

Fig. 3.20 Frames sequence obtained by high speed camera at 0.59 Q/Q_{Des} in the diffuser

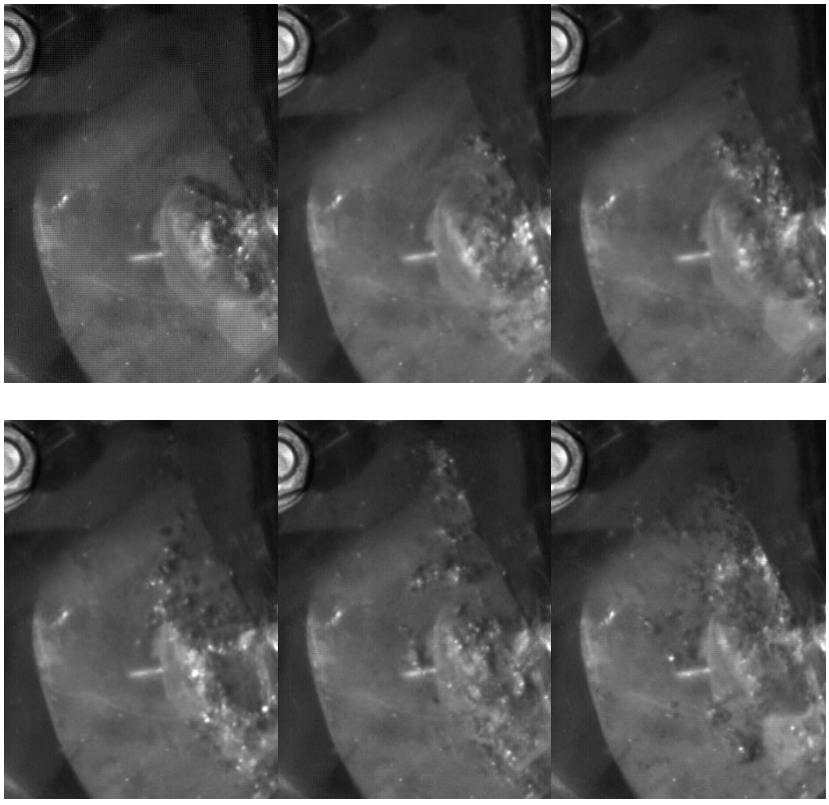

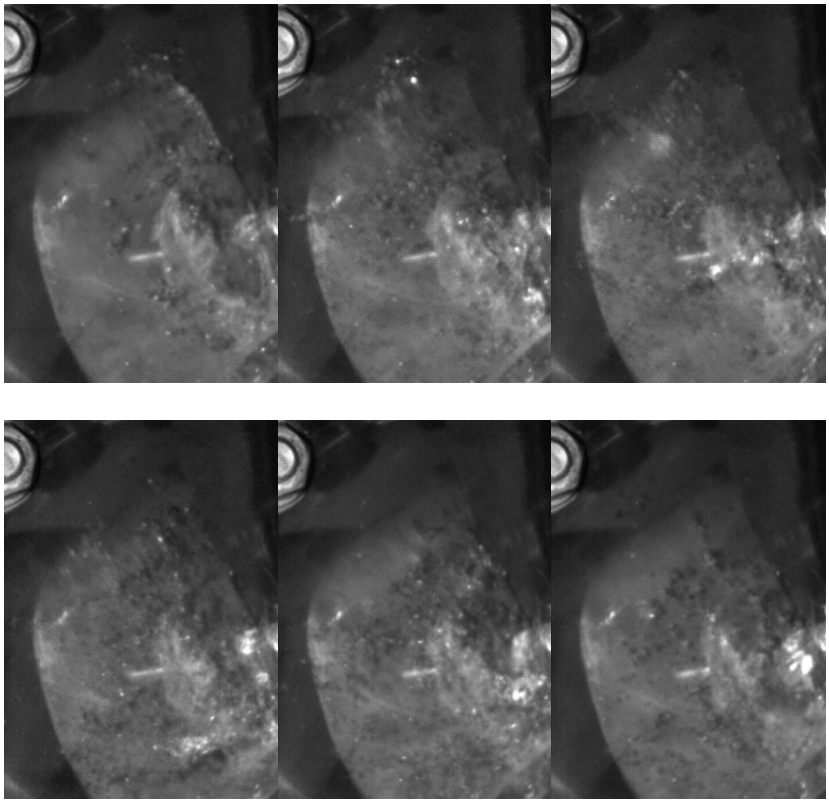

Fig. 3.21 Frames obtained by high speed camera at 0.59 Q_{Des} in the return channel

Below Q_{Des} = 0.45, which is for flow rate lower than the instability region, the periodic stall/back flow inside the diffuser disappeared. The bubbles path analyses show only vortexes of which the intensity and structure changed stochastically. In Fig. 3.22 some of the vortexes are shown.

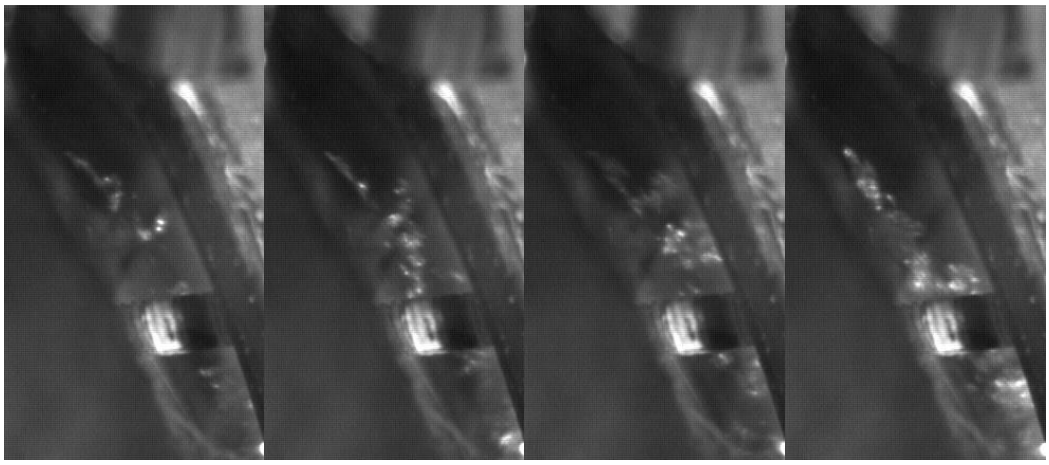

Fig. 3.22 Frames sequence obtained by high speed camera in the diffuser

3.3 Conclusions

Experimental analyses were carried out on a low specific speed pump-turbine operating at full and part load conditions on pump mode to study the characteristics and the development of the unsteady phenomena in saddle-instability region. The pressure variations in diffuser vanes both in time and frequency domains were analyzed. High-speed flow visualizations were used to analyze the flow field in this flow rate interval. Based on the above analysis, the following conclusions were derived in this section:

1. A rotating pressure disturbance at St=0.6625 with 5 cells was detected in diffuser at full load and most part load conditions. Combined with the results form high-speed visualizations, it indicated that this disturbance was caused by the unsteadiness at St=0.6625 which occurs on the stay vane suction side in the return channel just near the U shape corner.

2. Another periodic pressure fluctuation at St=0.335 was found in diffuser when the *Q-H* curve began to be unstable around 0.7 Q_{Des}. It was also propagate circumferentially with 2 cells. The high-speed camera results highlighted that this unsteady perturbation was coupled with an unsteady three-dimensional pattern into the diffuser vane channels. With the development of the unstable on the *Q-H* curve, a positive slop was found by several repeat tests around the critical flow rate 0.6 Q_{Des} and a drop of mean pressure variation has detected at the exit of impeller. Additionally, a reduction of pressure amplitude at St=0.335 and St=0.6625 has also been detected around this flow rate. Furthermore, with the furthering falling flow rate, the disturbance of St=0.335 disappear.

Some features of these two kinds of disturbances have been captured by the experimental results in this section. However, the causes and the development of these unsteadinesses with the falling of flow rate and what role they play on the unstable of *Q-H* curve remain unanswered. More comprehensive analysis about these questions would be done combined with numerical simulation of the fluid field and the relative acoustic field in Chapter 6 and 7.

III Numerical Investigation

Chapter 4 Investigation Methodology of Numerical Simulation

Due to the high expensive in terms of time and costs in experimental investigations, the numerical simulation becomes to be a useful complementary approach. The unsteadiness at part load not only seriously influences the stability of the performance curve, but also has great effect on flow-induce noise and vibration. For example, the rotating stall may resonate with an acoustic mode of the inlet or discharging piping and produces a serious pulsation problem (Dussourd 1968). In this research, the study of numerical simulation is carried out both on the flow field and the relative acoustic field.

4.1 Simulation of the Flow Field

Computational fluid dynamics, usually abbreviated as CFD, is used to research fluid flowing state. It is a relatively fast and cost effective method to evaluate performances and explore the flow hydrodynamics.

A normal CFD analyses normally includes the following parts: problem statement, mathematical model, discretization process and iterative solution strategy.

The problem statement applies the information about the geometry of the domain and operating conditions. The initial condition (IC), boundary conditions (BC) and turbulence model will be chosen based on this information. For the mathematical model, initial boundary value problem (IBVP) is composed of partial differential equations (PDE), IC and BC.

4.1.1 Governing Equations

The fundamental basis of almost all CFD problems are the Navier–Stokes equations, which are nonlinear PDE in almost every real situation and define any single-phase (gas or liquid, but not both) fluid flow. The derivation of the Navier–Stokes equations begins with an application of Newton's second law: conservation of momentum (often alongside mass and energy conservation) being written for an arbitrary portion of the fluid, the three-dimensional unsteady form of the Navier-Stokes Equations is(White 1979):

$$\frac{d\vec{V}}{dt} = \vec{R} - \frac{1}{\rho}\nabla p + \nu\nabla^2\vec{V} + \frac{1}{3}\nu\nabla\left(\nabla\cdot\vec{V}\right) \tag{4-1}$$

where $\vec{V}$ is the flow velocity, $\vec{R}$ represents body forces (per unit mass) acting on the fluid, t is time, ρ is the fluid density, p is the pressure, v is the Kinematic coefficient of viscosity which equal to $\frac{\mu}{\rho}$ and μ is dynamic coefficient of viscosity.

The Navier–Stokes equations are strictly a statement of the conservation of momentum. To fully describe fluid flow, more information is needed, how much depending on the assumptions made. This additional information may include boundary data (no-slip, capillary surface, etc.), conservation of mass, conservation of energy, and/or an equation of state. Normally, the continuity equation was written as bellow(White 1979):

$$\frac{\partial\rho}{\partial t} + \nabla\cdot(\rho\vec{V}) = 0 \tag{4-2}$$

Navier-Stokes equations are analytically solvable only in special cases. In CFD, a discretization method is used to approximate the differential equations by a system of algebraic equations, which can be solved on a computer.

For the analysis of flow phenomena and their numerical simulation in this study, the fluid is assumed incompressible. For incompressible flow and constant viscosity, $\frac{1}{3}\nu\nabla\left(\nabla\cdot\vec{V}\right)$ and $\nu\nabla^2\vec{V}$ equal to 0, the Navier–Stokes equations was written as bellow(White 1979):

$$\frac{d\vec{V}}{dt} = \vec{R} - \frac{1}{\rho}\nabla p \tag{4-3}$$

Some of the discretization methods used in CFX are finite volume method, finite element method, finite difference method, spectral element method and etc. In this study, the commercial CFD software ANSYS CFD 14.0 was used to conduct the simulation and finite volume method (FVM) is adopted to discretizate the equation.

FVM, as a common approach used in CFD codes, has an advantage in memory usage and solution speed, especially for large problems, high Reynolds number turbulent flows, and source term dominated flows (Patankar 1980).

4.1.2 Turbulence Modelling

In computational modelling of turbulent flows, one common objective is to obtain a model that can predict the quantity of interest. For turbulent flows, the range of length scales and complexity of phenomena involved in turbulence make most modelling approaches prohibitively expensive. The resolution required to resolve all scales involved in turbulence is beyond what is computationally possible. The primary approach in such cases is to create numerical models to approximate unresolved phenomena.

A typical approach is the Reynolds-Averaged Navier-Stokes equations (or RANS equations). The idea behind the equations, which is proposed by Osborne Reynolds(Reynolds 1895), is Reynolds decomposition, whereby an instantaneous quantity is decomposed into its time-averaged and fluctuating quantities. Typical examples of such models are the k-ε or the k-ω models in their different forms (Launder and Spalding 1974). These models simplify the problem to the solution of two additional transport equations and introduce an Eddy-Viscosity (turbulent viscosity) to compute the Reynolds Stresses.

Although RANS models are the economic approach for computing complex turbulent industrial flows, RANS models do not accurately predict all flow details in massively separated flow regions. In addition, the RANS formulation does not provide any information on turbulent flow structures and spectral distribution, which might be of importance to predict flow-induced noise or vibrations. Although the Large Eddy Simulation (LES) methods could obtain better results for separated and recirculating flow, on the other hand, experience has shown that the use of LES in boundary layer flows at high Re numbers is prohibitively expensive. Thus, LES is not an appropriate way to simulation the unsteadiness in turbomachines.

In order to save computing resources and computing time, hybrid RANS-LES approach is a good way to simulate the flow field in pump. Feng et al.(Feng, Benra et al. 2010) used the hybrid RANS-LES approach to predict successfully a “two-channel” stall phenomenon in the impeller , but RNG k-ε and SSG model failed to predict it. Lucius et al. (Lucius and Brenner 2010, Lucius and Brenner 2011) used another hybrid RANS-LES method called scale-adaptive simulation to calculate rotating stall in a centrifugal pump, and Vlad (Hasmatuchi, Roth et al. 2011) also applied it to investigate the stall flow in a pump-turbine.

In this study, the detached eddy simulation (DES) was adopted in the simulations to highlight the fluid-dynamical characteristic of the unsteady flow and investigate their origin. DES is a hybrid method of RANS and LES approaches that RANS is used to save computing power in the boundary layer region and LES is used to provide the information on turbulent flow structure and spectral distributions. DES is

a non-zonal approach and provides a single smooth velocity field across the RANS and the LES regions of the solution (Kotapati-Apparao, Squires et al. 2003, Kotapati-Apparao, Squires et al. 2004). For this simulation, the shear stress transport k-ω model covers the boundary layer while the Smagorinsky-Lilly model is applied in detached regions.

4.1.3 Computational Domain and Meshing

The computational domain includes the whole pump-turbine model. It is divided into four main components: inlet, impeller, diffuser and refeeding channels. The effect of leakage flow on the fluid flow would not be considered negligible in this research. The leakage system is modelled at both the impeller inlet and outlet as shown in Fig. 4.1. Moreover, the leakage flow rate of the impeller inlet and outlet is determined from the experiment results (Cavazzini 2013).

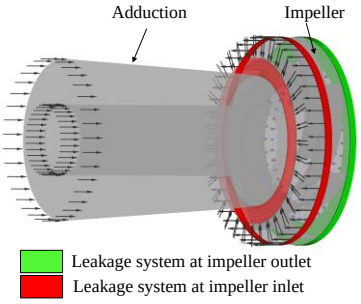

Fig. 4.1 Leakage system

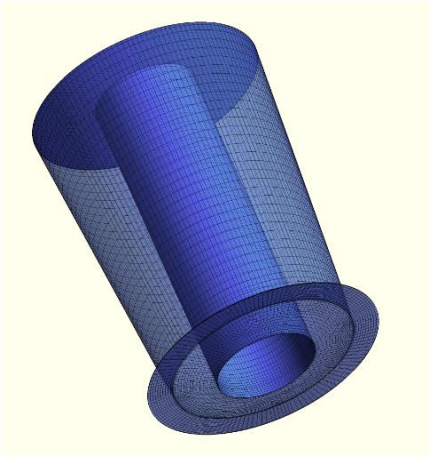

(a)Mesh details of inlet

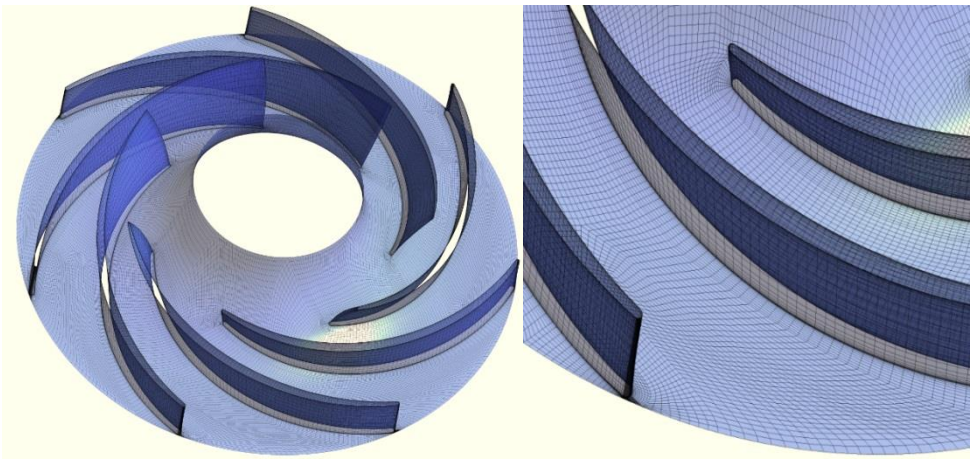

(b)Mesh details of impeller

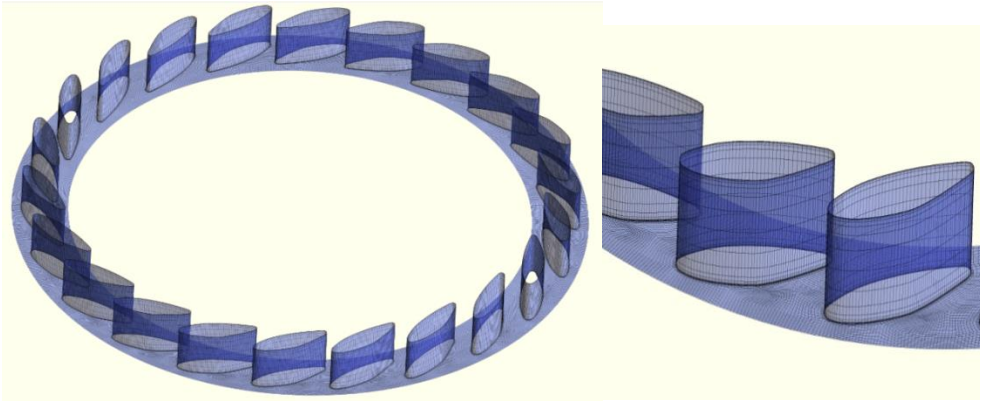

(c) Mesh details of diffuser

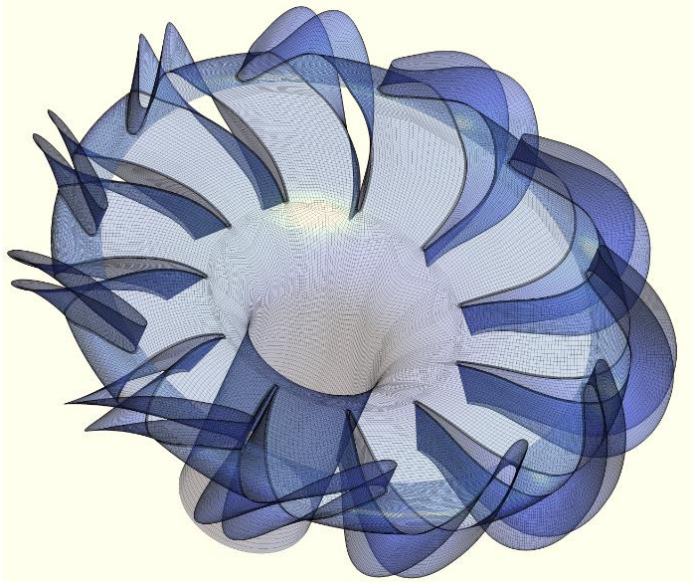

(d) Mesh details of return channel

Fig. 4.2 The mesh of different domain components

For the LES model, it is serious sensitive to the mesh and the time step. Thus, the refinement of grid and time step is important in this simulation. The discretization of different domain components is shown in Fig. 4.2. The adduction is discretized by a

structured mesh of about 339 500 elements. Anyway, care was taken to have a y+ value of approximately 30 at the first elements close to the wall. An O grid for the impeller investigation was performed. Preliminary tests were carried out to study the grid dependence and to guarantee an accurate and grid independent solution for the impeller. A grid independent solution can be obtained for the stage head H and the stage efficiency calculation with about 200 000 elements per passage. In the impeller computational domain, there is a total 2 600 000 cells with y+ values below 30. O-type grids are also adopted for both the diffuser and the return channel discretization with about 2 900 000 and 3 300 000 million cells, respectively. And several H-blocks are built to describe the cavities of the leakage system.

4.1.4 Boundary Conditions and Numerical Algorithm

The time step definition is based on the impeller rotation and it is of about one degree. The scheme adopted for the time discretization is a second-order implicit time stepping. A maximum number of five iterations are fixed for each time step, resulting in a mass residue of 10^{-6}, momentum residues of 10^{-4}, and turbulence kinetic energy and energy dissipation residues of 10^{-4}. In addition, the RMS (root-mean-square) courant number was CFL ≈0.15.

On both blades and wall surfaces, the boundary layer is assumed fully turbulent. For the interface between stator/rotor blocks, the standard transient sliding interface approach is chosen. The mass flow rate with stochastic fluctuations of the velocities with 5% free stream turbulence intensity is described at the inlet and the average static pressure is prescribed at the outlet.

In order to highlight the extremely complex fluid dynamic problem, head, flow rate and pressure are measured in the impeller, diffuser and return channel, respectively. The pressure monitor points were set in each impeller, diffuser and return channel blades, Fig. 4.3 shows the distribution of pressure monitors in one impeller blade, diffuser vane and return channel. The numerical signals are acquired for 14 impeller revolutions, corresponding to about 1.4s after 20 revolutions required achieving a quasi-steady simulation convergence.

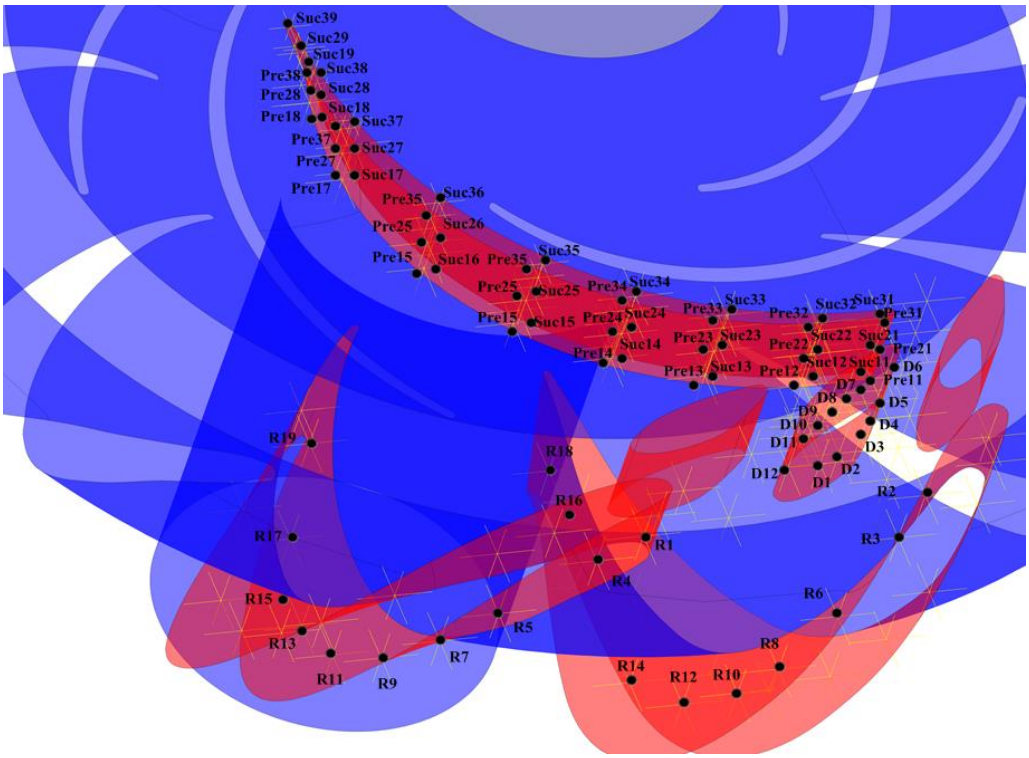

Fig 4. 3 Pressure monitors in a part of the model pump

4.2 Simulation of Intensity of Dipole Sources

With increasingly strict criteria for environmental noise, the property about low noise has become more and more important. The noise source in centrifugal pumps can be divided into structure-borne noise and flow-induced noise(Dürrer, Wurm et al. 2006). Normally，the noise inner the pump generated by unsteady flow phenomena (such as vortices, turbulent eddies, vortex shedding, turbulent boundary layers etc.) is termed as flow-induced noise (Yang, Yuan et al. 2014). Reynolds number characterizes the level of turbulence in the flow:

$$\mathrm{Re} = \frac{\text{inertial forces}}{\text{viscous forces}} = \frac{\rho V L}{\mu} \tag{4-4}$$

where ρ is the density of the fluid, V is the mean velocity of the object relative to the fluid, L is the characteristic linear dimension and μ is the viscosity of the fluid. Low *Re* flow always has large flow scales, and flow of high *Re* includes large flow scales and smaller flow scales. The unsteady vortices appear on many scales and interact with each other and with the surface, and then the flow-induced noise generates. In pumps, several processes result in pressure pulsations and excite flow-induced noise consequently(Jeon 2003).

Flow-induced noise could be classified into two parts. One part is the discrete noise at some characteristic frequencies (such as the blade-passing frequency (BPF), frequency of rotating stall and so on). This noise is the consequence of strong effect of periodic flows inner pump. The other one is the broadband noise which is due to turbulent flow and its frequency content was roughly determined by the length scale and velocity of hydrodynamic disturbances(Lee, Heo et al. 2010, Li, Ouyang et al. 2010). In general, the discrete noise is the primary part of flow-induced noise for pumps.

4.2.1 Method of Computational Flow-Induced Noise

For the research of discrete noise, experiment is the most direct and reliable choice(Rzentkowski and Zbroja 2000), but the complexity of the noise test and the large expense excludes the frequent use of this method. Fortunately, numerical simulation spans these gaps and has become a useful tool to research this issue.

For the simulation of the acoustic field caused by flow, the most straightforward approach is direct Computational Aero Acoustics (CAA), which means direct numerical simulation of both the unsteady turbulent flow and the generated noise. However, the high numerical cost of the direct CAA is prohibitive application at low Mach and high Reynolds numbers.

Compared to the direct CAA approach, the hybrid approach is relatively fast, cost effective and more flexible (Layton and Novotný 2010). In addition, the hybrid method of CFD coupled with computational acoustic has been used frequently. For example, Langthjem and Olhoff performed a coupled simulation of the hydroacoustic of a two-dimensional laboratory pump using a discrete vortex method (Langthjem and Olhoff 2004, Langthjem and Olhoff 2004), and Sergey has developed a 3D CFD--CAA acoustic-vortex method (Timushev 2009).

In this approach, the computational domain is split into different regions: one is for the generation of sound and the other is for the propagation of sound. Firstly, the flow field was simulated by Computational Fluid Dynamics (CFD) tool, and the flow induced noise sources due to flow effects are generated on this step. Secondly, an acoustic solver calculates the propagation of sound waves caused by flow effects.

For this approach, the fundamental assumption is one-way coupling. It means that the unsteady flow produces sound and affects its propagation while the sound waves do not affect the flow field significantly.

The principal application of the hybrid approach is the flows at low Mach numbers and not strong coupling.

For this case, the appropriate Mach number could be calculated by equation:

$$M = \frac{impeller\ periheral velocity}{speed of\ sound} \tag{4-5}$$

and the Mach number of this pump is far smaller than 1.

Lighthill's analogy is one of the classical methods for the hybrid approach. This analogy is only valid when the acoustic back-reaction on the hydrodynamic field could be neglected. This needs to meet the following three conditions(Langthjem and Olhoff 2004, Langthjem and Olhoff 2004):

1. The characteristic Mach number $M \ll 1$;

2. Compressibility is unimportant in determining the flow;

3. The flow is not coupled to a resonating system.

At the same time, the pump system in this study also satisfies the condition 2 and 3. Therefore, Lighthill's analogy is suitable for the acoustic simulation in this study. In this analogy, the noise sources are divided into three different acoustic sources (monopole, dipole and quadrupole) which include displacement of the fluid by a moving boundary, pressure fluctuations on surfaces within the CFD calculation, as well as interior flow features.

Monopole source (as shown in Fig. 4.4) is a result of fluid being displaced by the swept volume of a moving boundary as it propagates through its range of motion. Sometimes this noise source is also called the “self noise” or the “thickness noise” of the device. Typically it is neglected for low speeds case and its acoustic power is proportional to the fourth power of velocity.

Dipole source arises from the fluctuation of forces on the surface, so it is possibly rotating. Sometimes these sources are also referred to as “loading noise.” Strictly speaking, these forces cannot be evaluated without knowledge of the acoustic field. However, the Lighthill analogy neglects any two-way coupling, and the forces due to acoustic fluctuations are much smaller than the dynamic forces. Hence, it is perfectly valid to only consider the dynamic forces created by the bulk fluid flow. Its acoustic power is proportional to the sixth power of velocity.

Quadrupole sources arise in the interior of the flow and results from turbulence fluctuations in wakes, shear layers, or interaction of flow features. Because many of these features are three-dimensional in nature and transient data for a symmetric tensor is needed over some three-dimensional region of the CFD calculation,

quadrupole sources are very expensive to evaluate and store. The acoustic power is proportional to the eighth power of velocity.

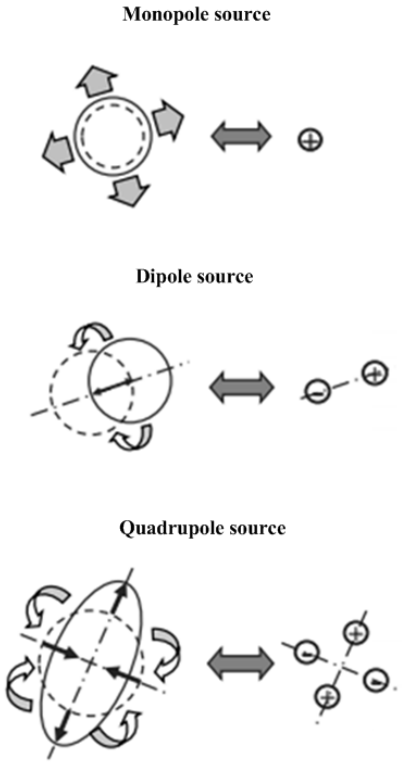

Fig. 4.4 Diagram of three different acoustic sources

4.2.2 Numerical Scheme of Intensity of Dipole Sources

The roles of these three acoustic sources play in centrifugal pump were analyzed by Langthjem (Langthjem and Olhoff 2004, Langthjem and Olhoff 2004). He indicated that monopole sources might exist in a centrifugal pump in form of no uniform outflow from the impeller, and in the form of flow and stagnation pressure oscillations at the pump discharge. However, these are normally weak in a well-designed pump. Dipole sources exist in the form of fluctuating pressure forces on both rotating and stationary parts. These may be of significant magnitude, especially for pumps with high hydrodynamic efficiencies. Quadrupole sources are found in the unsteady, highly turbulent wake flow.

Ffowcs Williams and Hawkings (Williams and Hawkings 1969) analyzed the balance between dipole and quadrupole contributions to the total sound generation by multi-bladed fans rotating in a free field, and the results showed that the quadrupole contribution may be comparable with the dipole contribution if the fan has very many blades rotating near sonic speed (M≈1). However, for a typical centrifugal pump, the

Mach number is far smaller than 1, so the noise contribution from quadrupoles can safely be neglected in this study.

Therefore, only the pressure fluctuations on the internal surface (the dipole sources), which are caused by the interaction between the fluid including the rotating blades, the diffuser, and the return channel, are considered in this study.

In order to obtain various noise sources, the DES model is used in the CFD simulation, which is discussed in the previous section. During the prediction, the surface pressure pulsations of the blades as the dipole source are provided by ANSYS-CFX, and then the strength of the dipole source is computed by FFT transform.

The maximum frequency to be analyzed in this step is given by time step setting in the CFD simulation.

$$f_{\max} = \frac{1}{2\Delta t} \tag{4-6}$$

for this case, the time step is 3.23×10^{-4} which is equal to the time for the impeller rotating one degree. $f_{\max}$ is equal to 1540Hz. The real time of input sources data is 1s (10 impeller revolutions). Thus, the frequency resolution of this simulation is 1Hz.

Chapter 5 Numerical Simulation Validation

The numerical analysis was carried out for some flow rates from full load to part load (Q/ Q_{Des} = 0.4571, 0.5325, 0.583, 0.630, 0.674, and 1.000). In this section, with the help of experimental results, the feasibility of the numerical solution was proved both quantitatively and qualitatively.

5.1 Quantitative Validation

For the quantitative validation, the head and the power obtained through numerical simulation were compared with the experimental values firstly as shown in Fig. 5.1. The head of pump by simulation results was calculated by Eq. (5-1) based on weighted average:

$$H = \frac{1}{\rho g}\left(\frac{\sum mP_{total\_2}}{\sum m} - \frac{\sum mP_{total\_1}}{\sum m}\right) \tag{5-1}$$

Where P_{total_2} is total pressure of outlet and P_{total_1} is the total pressure of inlet. The numerically calculated characteristic shown in Fig. 5.1 (a) is also with the head oscillation band. Outside the head discontinuities on the lower branch of the saddle/hysteresis good numerical convergence was always obtained. Below the transition between the two head-branches, numerical convergence was not obtained. At the time, the numerical power is consistent with the test value (Fig. 5.1 (b)). Thus, the model for the leakage system in this simulation could simulate the loss in the leakage very well. In general, the results obtained from this numerical simulation show very good agreement with the performance characteristics by experiment.

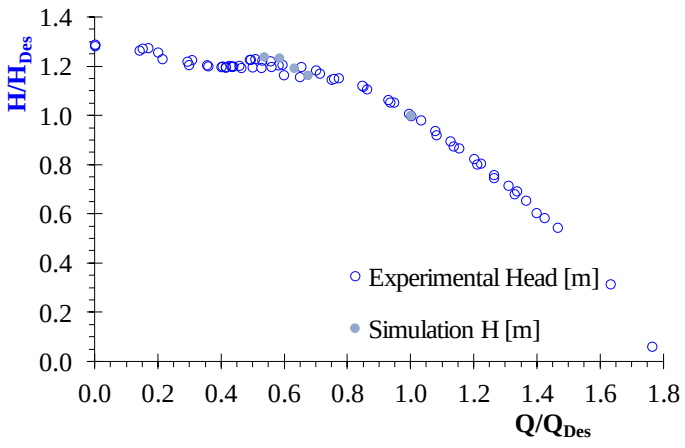

(a) The comparison of head

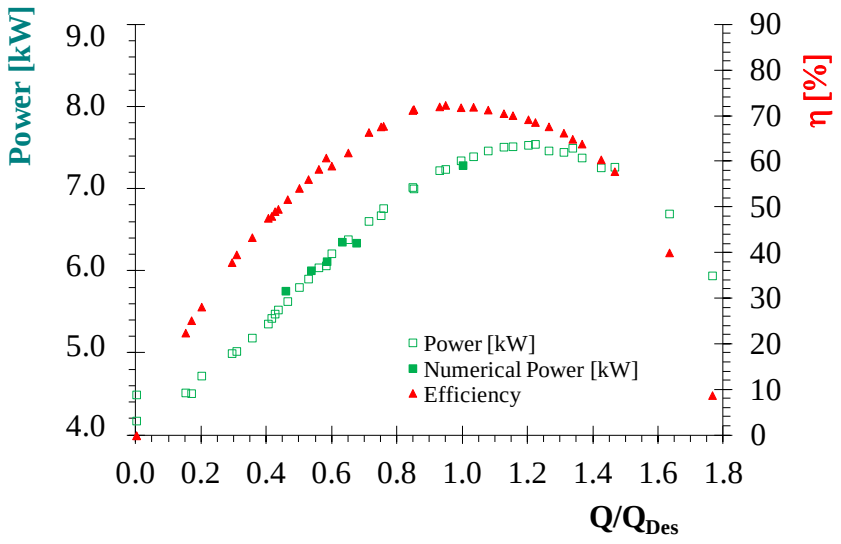

(b) The comparison of head

Fig. 5.1 Experimental and numerical pump characters

At the same time, the frequency peak St=0.6625, which is found in experimental analysis from full load to part load, was also found in the head fluctuations of numerical simulation results, which is shown in Fig. 5.2. However, the amplitude of fluctuations at St=0.6625 was less pronounced in simulation compared to the experimental results.

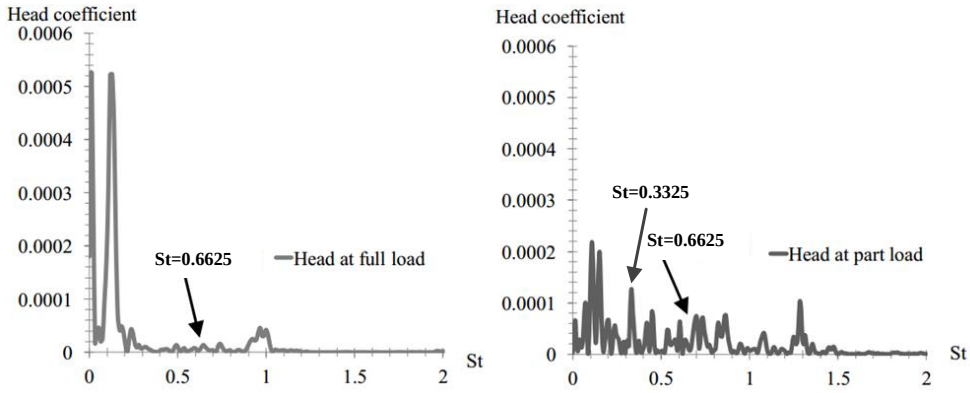

(a) Q/Q_{Des} = 1 (b) Q/Q_{Des} = 0. 583

Fig. 5.2 Head fluctuations of numerical simulation results against frequency at different flow rates

Additionally, in the saddle instability region, the frequency peak at St=0.335, which is the other non-linear frequency component, was also detected in the results of numerical simulation at part load $0.583Q_{Des}$.

Furthermore, the pressure intensity decrease at St=0.335 and 0.6625 around 0.6 Q_{Des} was also detected by the simulation results. Figure 5.3 shows the cross spectrum of pressure between two monitors located at the inlet of the adjacent diffuser channels. In this figure, it is indicated that the value at St=0.6625 and St=0.335 vanished when the flow rate decreases from 0.63 to 0.583 Q_{Des}. Moreover, the intensity of amplitude at St=0.335 reduced with the reduction of flow rate, which is consistent with the experiment results in Chapter 3.1.

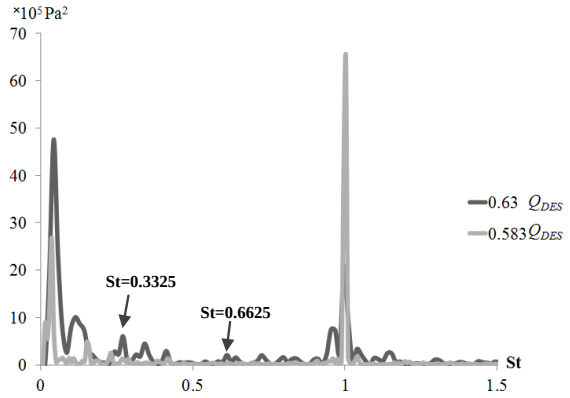

Fig. 5.3 Cross spectrum of pressure monitors at the inlet of diffuser channel 8 and 9 at 0.63 to 0.583 Q_{Des}

5.2 Qualitative Validation

In addition, the comparison of the flow field was conducted to validate the accuracy of numerical simulation results with the help of the high-speed flow visualizations. For the experimental results, the bubbles were injected from the surface of diffuser and stay vanes. Thus, the validation of the flow field was divided into two parts: diffuser channel and return channel.

First, the flow field in diffuser channel was compared as shown in Fig. 5.4 and 5.5 at full load and part load. The flow fields, which were captured by both the high-speed camera and simulation, are relatively consistent: the approaching flow in the diffuser was quit uniform at full load, and only weak flow separations was detected near hub and shroud at the trailing edge of diffuser vane.

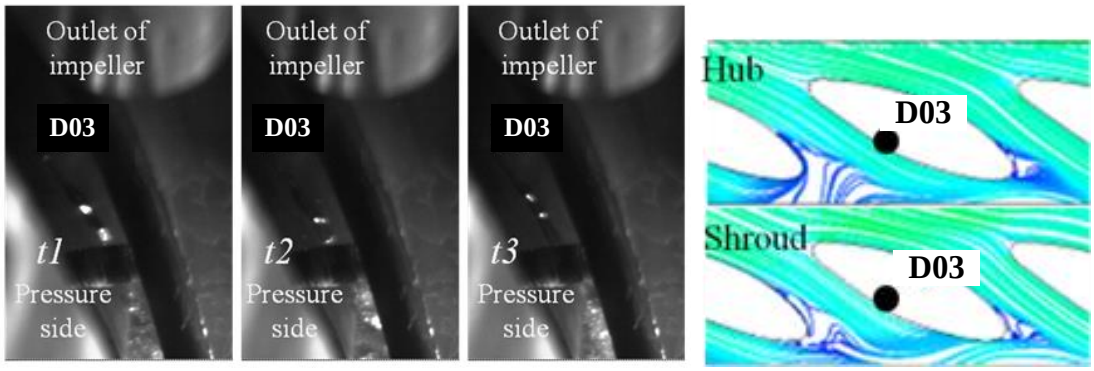

(a) High speed visualization (b) Numerical simulation results

Fig. 5.4 Comparison of flow field at full load in diffuser vane channel

When the test pump operated at part load condition, local unsteady flow became more frequent and intense in diffuser vane channel. Figure 5.5 (a) shows the bubble trajectories at different times in the diffuser channel at 0.583 Q_{Des}. The bubbles flow near the pressure side of diffuser vane sometimes in a smooth way (likes t1), sometimes showing unstableness on the crosswise direction (likes t5) and sometimes moveing back toward the impeller (likes t7). At the same time, in the simulation, a strong flow separation at the vane suction side was captured on the crosswise direction. With the development of the unsteady flow, it could influence the fluid on the blade pressure side. That could explain why the unsteady was detected intermittently in crosswise direction by high-speed camera.

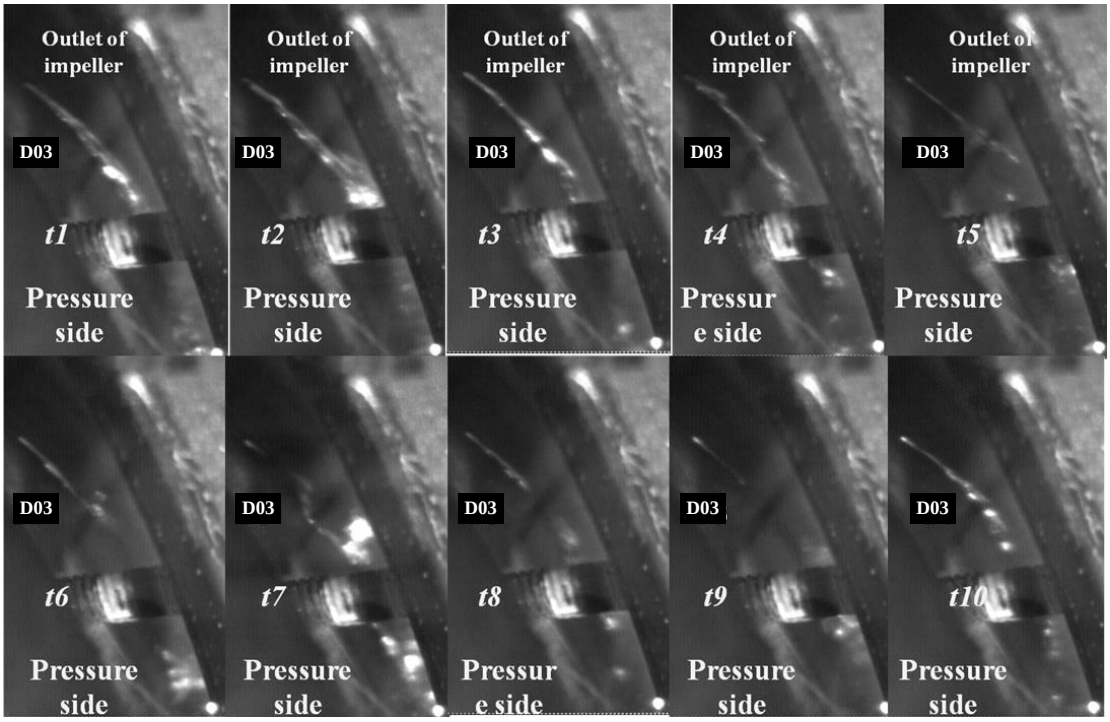

(a) High speed visualization

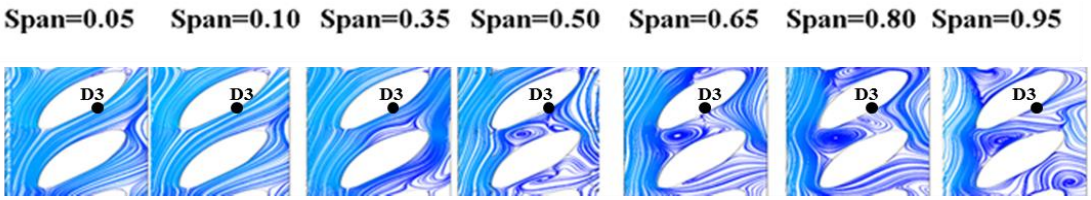

(b) Numerical simulation results

Fig. 5.5 Comparison of flow field at full load in diffuser vane channel at Q/Q_{Des}=0.583

The comparison of the flow field in return channel was also conducted. The pictures captured by experimental and numerical results are shown in Fig. 5.6 and 5.7. Figure 5.6 presents the flow field near the leading edge of return vane at the pressure side at full load. Figure 5.6 (a) shows the trajectories of bubble from the R15 by high-speed camera at different times and a small periodical whirl was detected. In the simulation, this whirl was also captured as showed in Fig. 5.6 (b). Moreover, this whirl weakens gradually from shroud to mid span.

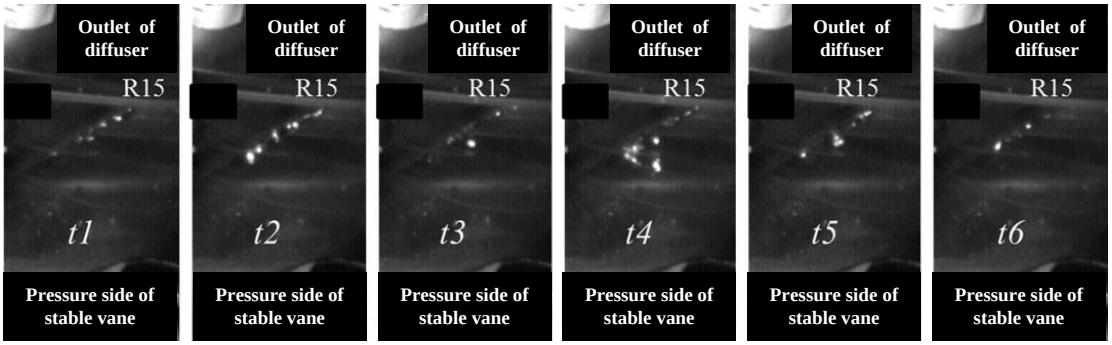

(a)High speed visualization

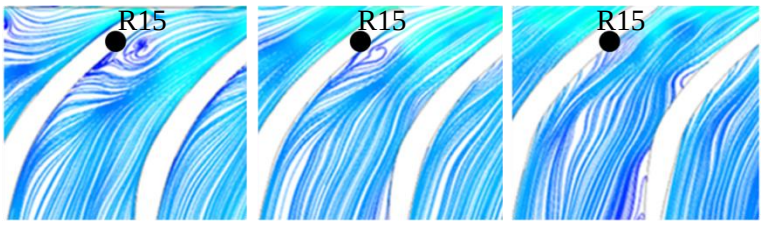

Span=0.95 Span=0.8 Span=0.65

(b) Numerical simulation results

Fig. 5.6 Comparison of flow field at full load in return channel (R15)

Figure 5.7 shows the bubble trajectories from the R16 near the leading edge of suction side. There was a strong 3-dimentional unsteady pattern including a periodic fluctuation at St=0.6625 near R16 which was also detected in the simulation as shown in Fig. 5.7 (b).

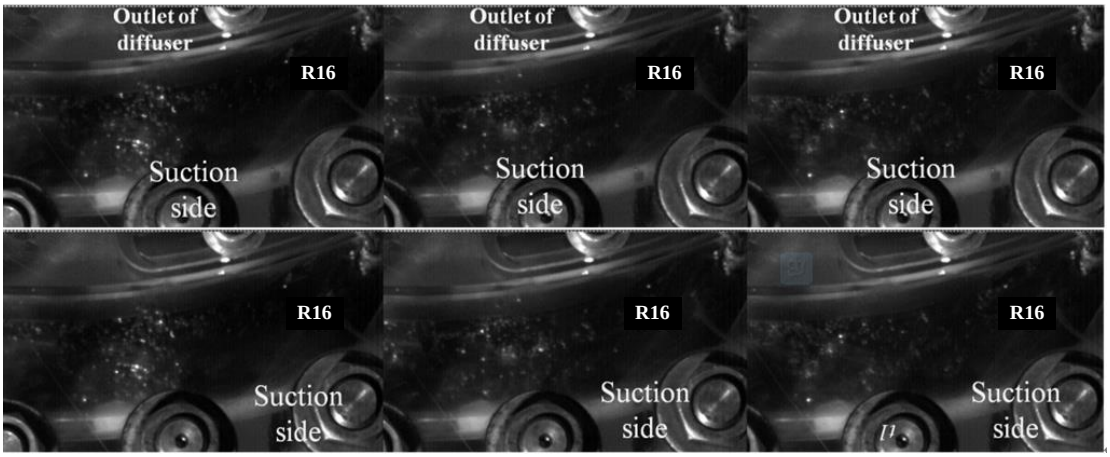

(a) High speed visualization

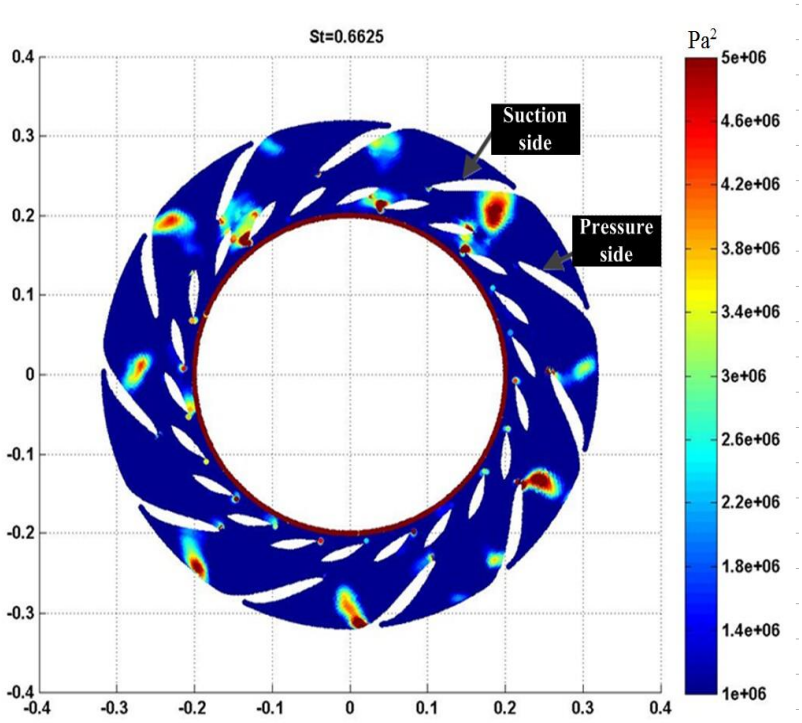

(b) Pressure distribution at St=0.6625 by numerical simulation results

Fig. 5.7 Comparison of flow field at full load in return channel (R16)

5.3 Conclusions

BThe comparison between numerical and experimental data indicates that the numerical head and shaft power from full load to part load agree well with the experimental data.

Additionally, the numerical results also capture the pressure disturbance at St=0.6625 from full load to part load and the other non-linear frequency component at St=0.335 in the unstable region of Q-H curve. However, the numerical pressure of these frequencies present weaker intensity in the spectrum than the experimental data.

At the same time, the decreasing of the pressure intensity around the critical flow rate of $0.6Q_{Des}$ was also computed by the simulation results. Furthermore, with the help of the high-speed visualizations, the reasonable agreement of flow field between numerical and experimental results was validated.

Thus, the simulation of the flow field in this research could be used as reliable results to help understand the features of the flow inner pump at different flow rates.

Chapter 6 Unsteady Patterns at Full Load Condition

The experimental analysis in chapter 3 indicated that unsteady flow patterns occur even at full load condition in the test pump. By the results of high-speed camera, it shows that these unsteady flow patterns mainly occur in the first part of return channel and caused weak unsteady patterns near the trailing edge of diffuser vanes. Thus, the flow field in diffuser and return channel by simulation was discussed firstly in this chapter to help know more information about these unsteady flow patterns at full load condition.

6.1. Unsteady Flow Patterns in Diffuser and Return Channel

6.1.1 Statistical Analysis on Pressure Fluctuations

In order to highlight the time scales of unsteady fluctuations, statistical methods were adopted to analyze the pressure fluctuation intensity on each grid node in the fluid domain (Pei, Dohmen et al. 2012, Pei, Yuan et al. 2012, Pei, Yuan et al. 2013). The advantage of these methods is their ability to record the pressure fluctuation distribution and strength in the inner unsteady flow field directly and comprehensively for several impeller revolutions.

In this study, root mean square and the standard deviation of pressure was used to indicate the pressure fluctuation intensity. The pressure on any grid node *i* can be given as $p_i(x,y,z,t)$. The pressure coefficient, which represents the normalized pressure, is defined as follows:

$$C_{pi} = p_i / 0.5\rho u_2^{\,2} \tag{6-1}$$

The average pressure coefficient in any period could be calculated using Eq. (6-2)

$$\overline{C_{pi}} = \frac{1}{N}\sum_{n=0}^{N-1} C_{pi}(x,y,z,\frac{n}{N}) \tag{6-2}$$

where *N* is number of the time step adopted in the calculation. In this study, two different time records were used to analyze the time scale of the pressure disturbance, which are one impeller revolution (0.1s, *N*=308) and 10 impeller revolutions (1s, *N*=3080).

The maximum and minimum pressure coefficients could be calculated using Eqs. (6-3) and (6-4)

$$C_{pi\max} = \max[C_{pi}(x, y, z, \frac{n}{N})] \tag{6-3}$$

$$C_{pi\min} = \min[C_{pi}(x, y, z, \frac{n}{N})] \tag{6-4}$$

where n=(0, 1, 2……, N-1).

The root mean square of the pressure coefficient could be calculated using Eq. (6-5), and the standard deviation of pressure coefficient was calculated by Eq. (6-6)

$$C_{pirms} = \sqrt{\frac{1}{N-1}\sum_{n=0}^{N}\left(C_{pi}(x, y, z, \frac{n}{N})\right)^2} \tag{6-5}$$

$$C_{pisdv} = \frac{1}{N-1}\sqrt{\sum_{n=0}^{N}\left(C_{pi}(x, y, z, \frac{n}{N}) - \overline{C_{pi}}\right)^2} \tag{6-6}$$

In the CFX solver, most variables, such as the pressure variable, are global variables, which can be read from each grid node in the calculation domain. Therefore, using the CFX Expression Language and the Frozen Copy function, all the statistical coefficients related to the results for several entire impeller revolution periods, defined above, can be expressed, and the corresponding global variables can be established. The statistical results on each grid node can then be obtained by reading the variables.

At full load, the distribution of pressure and velocity in impeller was quite even, and the unsteady flow patterns mainly occurred in diffuser and return channel. Thus, the statistical analysis was focused on diffuser and return channel. Fig. 6.1 was the distribution of instantaneous pressure coefficient C_{p} and root mean square of the pressure coefficient C_{pirms} (in 0.1s) in diffuser and return channel at full load. For the distribution of instantaneous C_{p}, it was uneven around the outlet of diffuser and inlet of return channel. However, the distribution of C_{prms} is quite even in diffuser and return channel. Thus, unsteady phenomena mainly occurred near the inlet of return channel and the time scale was smaller than 0.1s. So the frequency of this phenomena approximately equals or greater than 10Hz.

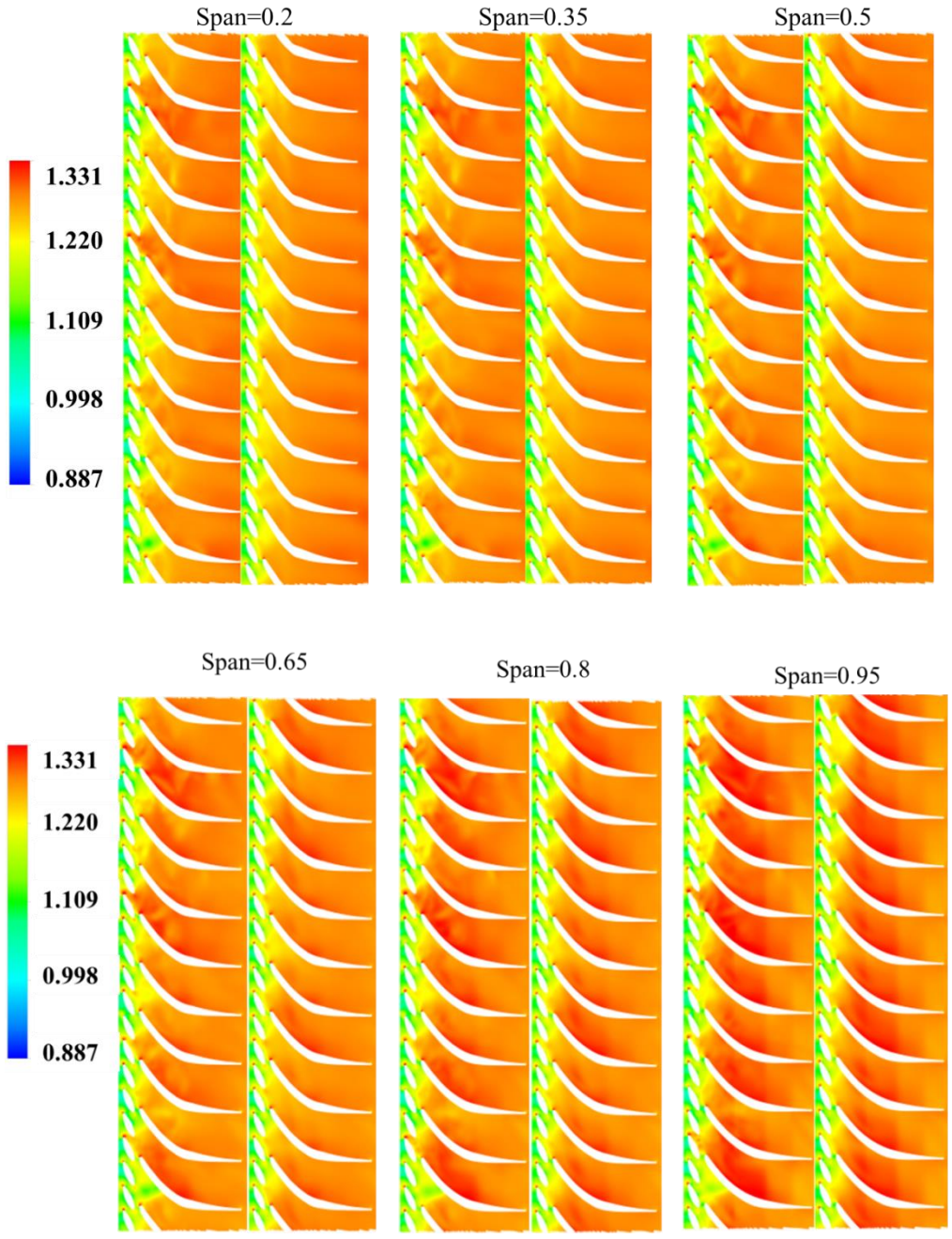

Fig. 6.1 Pressure distribution in diffuser and return channel at full load

6.1.2 Unsteady Pattern at St=0.6625

At full load condition, inside the diffuser vane channel, the trajectory of air bubbles from D03 hole was straight with a quite negligible longitudinally unsteadiness downstream of the trailing edge (Fig. 6.2 (a)) which is consistent with the simulation results (Fig. 6.2 (b)). In the return vane channel, the bubbles, which blew out from the R16, were rapidly scattered forming puffs of bubbles. The bubbles

flow pattern was close to the vane suction side (Fig. 6.3(a)), the unsteady flow pattern has a pulsation with frequency St= 0.6625. This region is agreeing with the uneven region of instantaneous C_{pi} in Fig. 6.1. Moreover, in the picture of streamlines (Fig. 6.3 (b)), a similar unsteady flow pattern was also found.

Meanwhile, the velocity at the mid span of diffuser and the first part of return channel was processed by fast Fourier transform. Fig. 6.3 (c) illustrates the distribution of the results at St=0.6625. The picture shows that the high value region of velocity at this frequency also mainly appeared at the first part of return channel and near the suction side of vane. This location was coincided highly with the place of the unsteady pattern in return channel which was found by high speed camera.

In order to know more details of this disturbance, Fig. 6.4 shows the distribution of the pressure amplitude at St=0.6625 on different cross sections of diffuser and return channel at full load. It indicates that the high amplitude pressure regions mainly appear near the suction side of stay vanes. From hub to shroud, pressure intensity of the high amplitude regions gradually weakens. Furthermore, near hub, some obvious high pressure regions were found near the trailing edge of adjusted vane.

Therefore, due to the U return stay vane, even at full load condition, there are unsteady flow pat terns with frequency St=0.6625 in the return channel near suction side of the stay vane and the U shape corner. This unsteady flow pattern was strongest near hub.

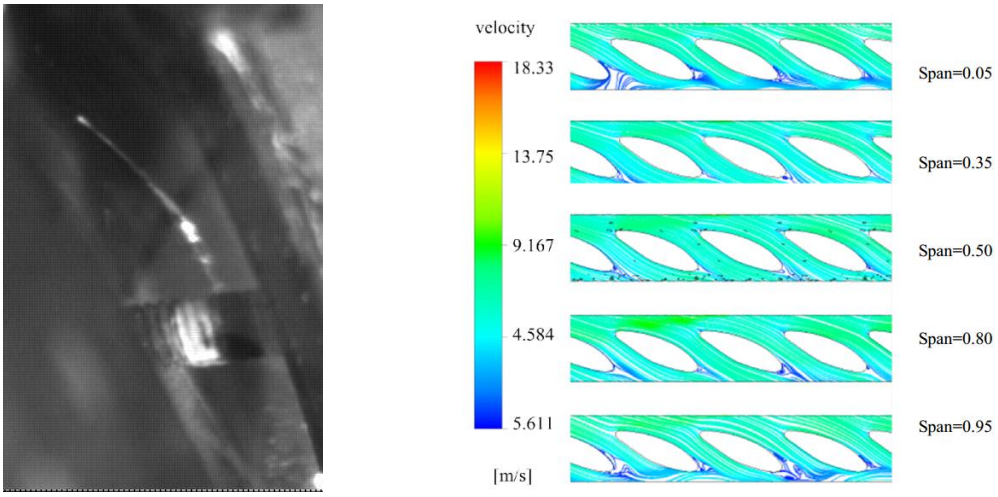

(a) (b)

Fig. 6.2 Flow field in diffuser at Q_{Des} (a) The trajectory of air bubbles from D03 hole in diffuser (b) Instantaneous velocity streamlines at different spans of diffuser

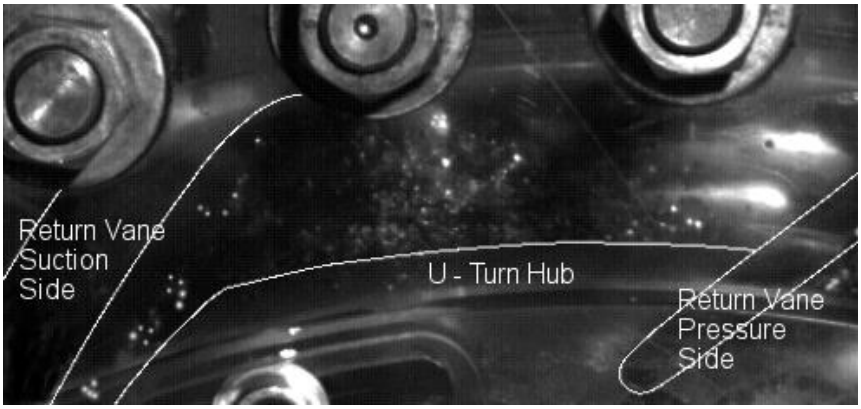

(a)

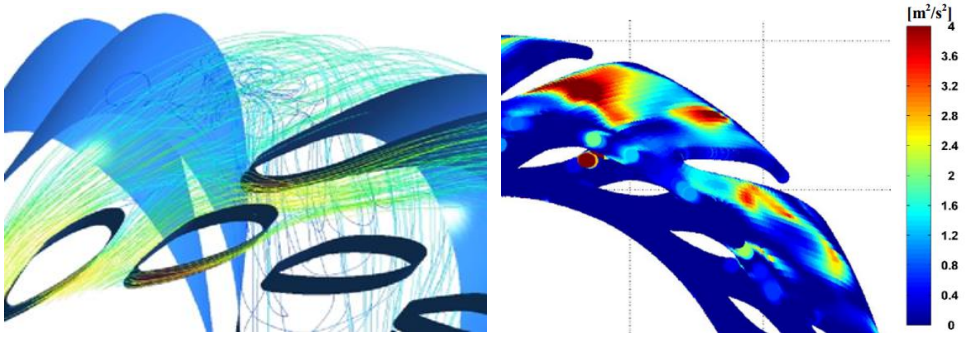

(b) (c)

Fig. 6.3 Flow field in diffuser and return channel at Q_{Des} (a) Trajectory of air bubbles from R16 hole (b) Instantaneous velocity streamlines by simulation (c) Velocity distribution at St=0.6625 at mid spam by simulation

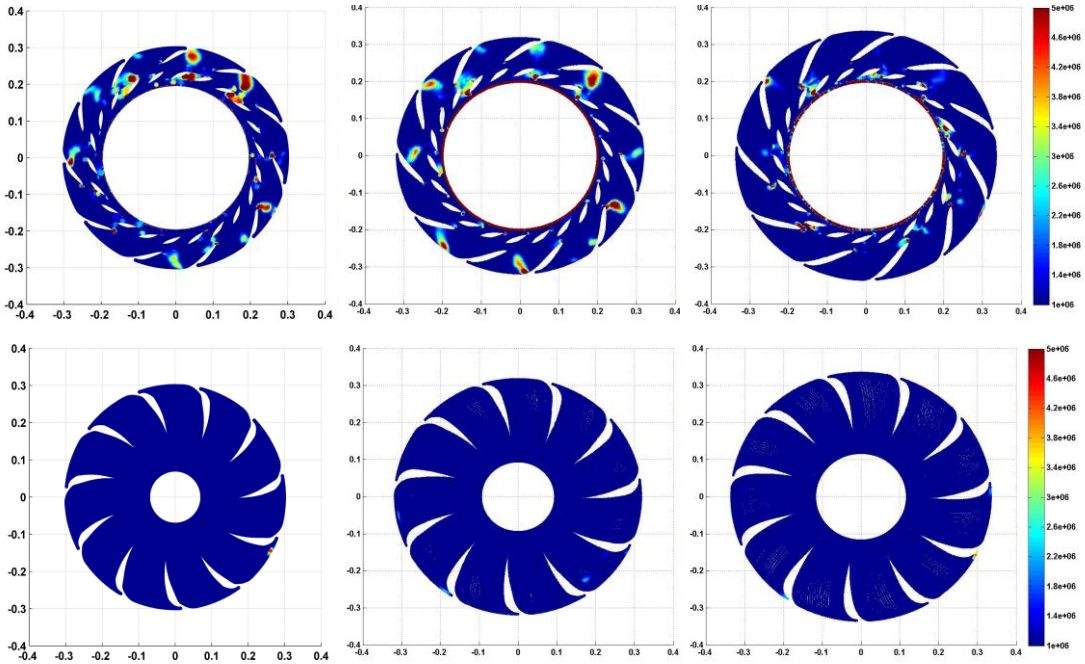

(a) Hub (b) Mid (c) Shroud

Fig. 6.4 Distribution of the pressure amplitude at St=0.6625 on different cross sections of diffuser and return channel at Q_{Des}

6.1.3 Unsteady Pattern at St=0.042 and 0.085

Except unsteady disturbance at St=0.6625, there were some other disturbance at different frequencies (St=0.042 and 0.085). In order to highlight the characteristics of these unsteady disturbances, the pressure, velocity, total pressure and flow rate of diffuser and return channels were analyzed in this section.

6.1.3.1 Frequency Analysis of the Pressure and Velocity

In order to highlight the location of the patterns in the diffuser and return channel, the frequency analysis on the velocity and pressure at these frequencies on the cross section were analyzed.

The data (velocity and pressure) on each node, which were extracted from the sections near hub span, mid span and near shroud span of the diffuser and return channel, were processed by the Fourier transforms.

Firstly, the distribution of velocity intensity was discussed at St=0.042 and St=0.085. For these frequencies, the high amplitude region was also focused on the first part of return channel and some trailing edge of diffuser vane as shown in Fig. 6.5 and 6.6. It could be found that the locations of high amplitude at these frequencies were consistent with St=0.6625 (Fig. 6.3(c)). Furthermore, the distribution of pressure intensity at these two frequencies which shows in Fig. 6.6 was also similar to the distribution at St=0.6625 (Fig. 6.4).

Thus, at full load, the unsteady flow which occurs in the return channel also contains periodically disturbance with frequencies St=0.042 and St=0.085. Like the unsteady disturbance at St=0.6625, these unsteady patterns happened in first part of return channel and near the suction side of stay vane and influence some diffuser channels remarkably.

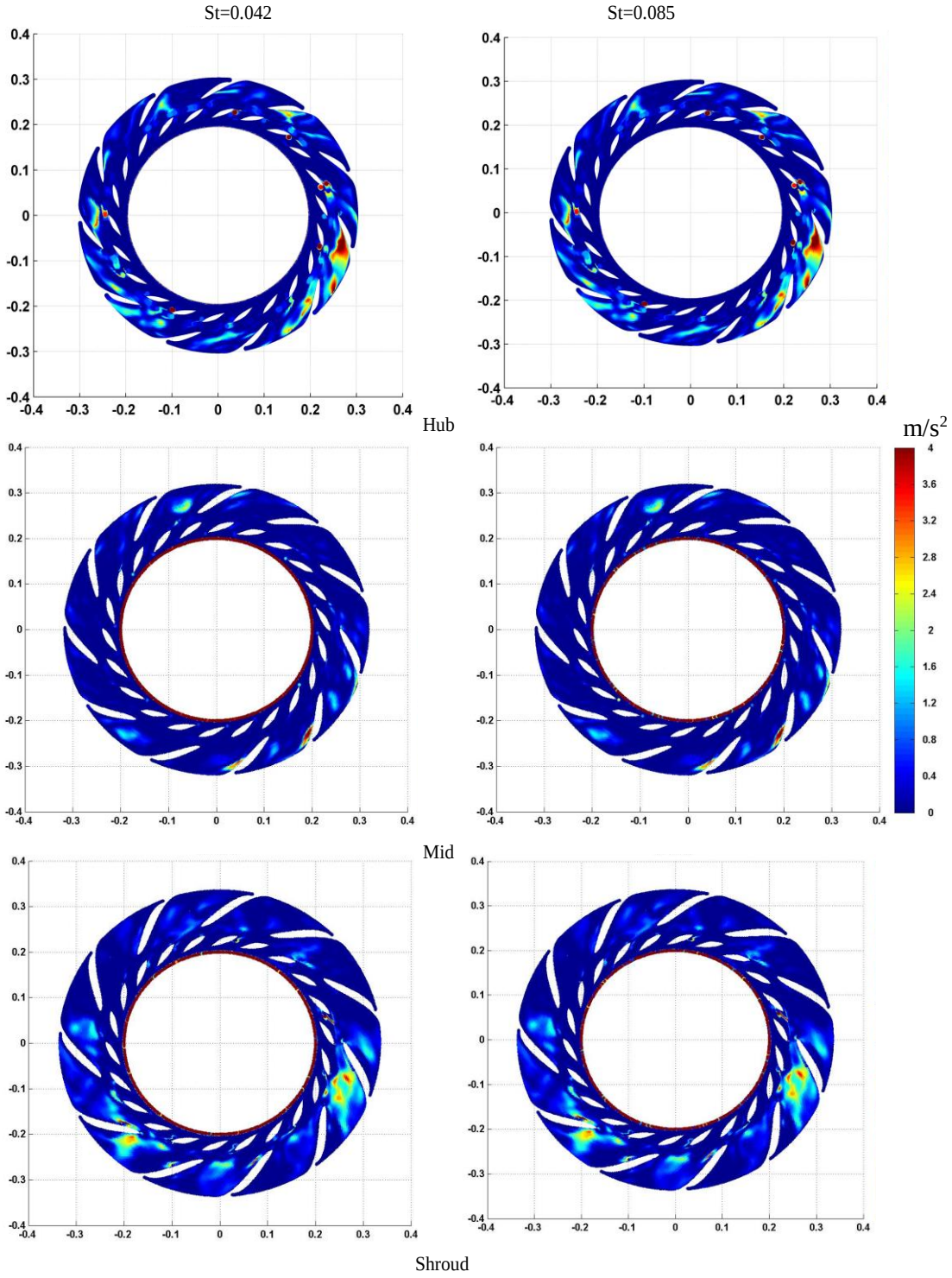

Fig 6.5 Distribution of the velocity amplitude at St=0.042 and St=0.085 on different cross sections of diffuser and return channel at Q_{Des}

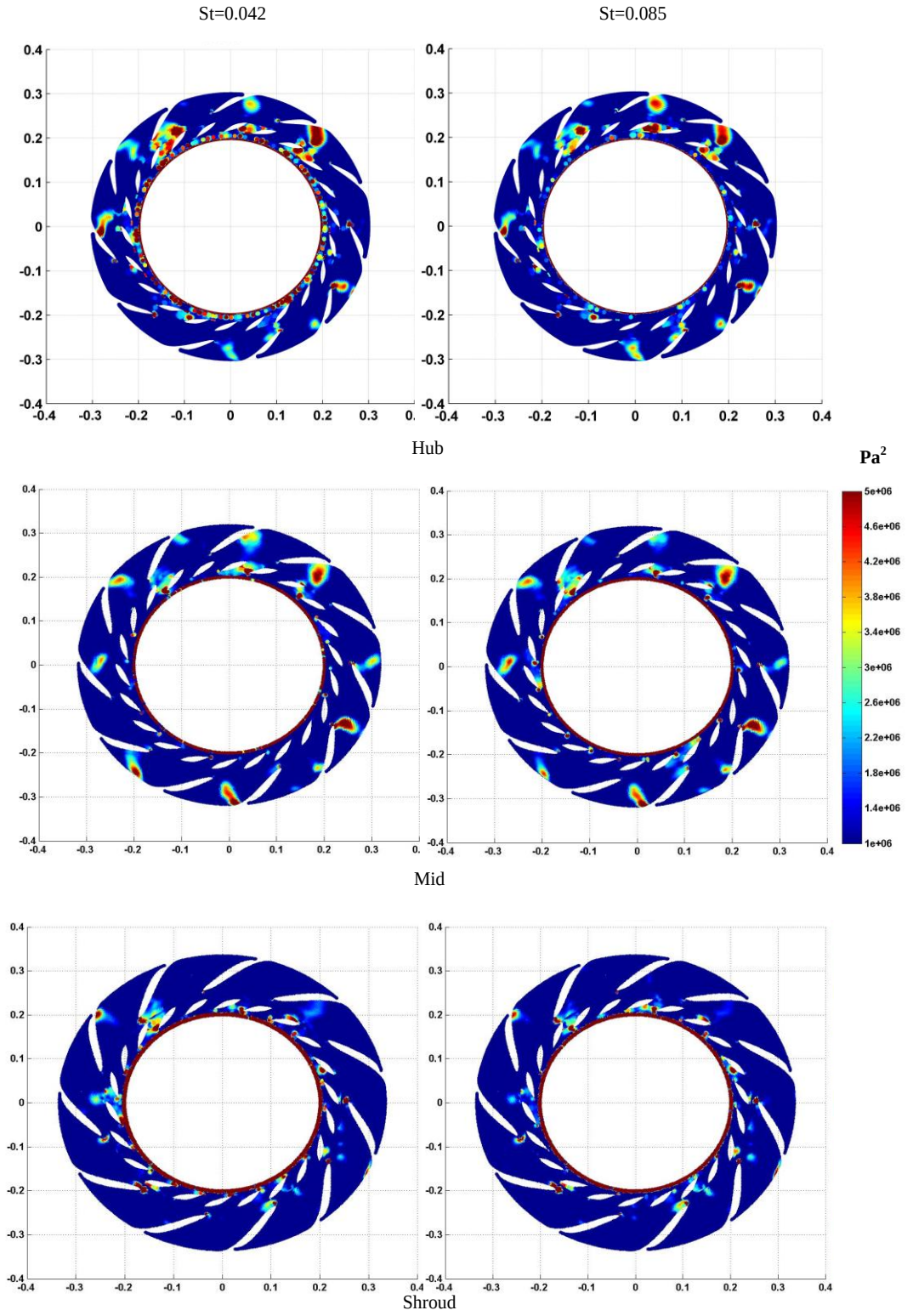

Fig 6.6 Distribution of the pressure amplitude at St=0.042 and St=0.085 on different cross sections of diffuser and return channel at Q_{Des}

6.1.3.2 The Analysis of the Instantaneous Total Pressure in Each Diffuser and Return Channel

Based on the analysis of the instantaneous pressure, total pressure and flow rate in the diffuser and return channels, several propagation characters were detected at St=0.042 and St=0.085.

Figure 6.7 shows the information about total pressure at the inlet of each diffuser channel. Figure 6.7 (a) presents that the total pressure of each diffuser channel changes in two impeller revolutions (0.2s). It indicates that the perturbation consists of 7 cells and propagates in the impeller rotating in the same direction and with the speed ω_{imp} of the impeller. This feature is consistent with the auto spectrum of the total pressure in diffuser channel 1 (Fig. 6.7. (b)) which presents a peaks at BPF. This perturbation is caused by the rotor and stator interaction.

The total pressure at the outlet of each diffuser channels was shown in Fig. 6.8. The fluctuation of total pressure at outlet was more complex than at inlet. In Fig. 6.8 (a), there is an encounter pattern rotating in the reverse direction at $1.75\omega_{imp}$ which was indicated by black dotted lines marked $-1.75\omega_{imp}$ and consisting of 4 diametrically cells. It may contribute the auto spectrum peaks near St=1 in Fig. 6.8 (b). Also, another rotating perturbation was found in the time history which rotates far smaller than impeller and propagates forward. Compared with the spectrum of total pressure in the inlet of diffuser, there was a weak peak at St=0.6625 captured at the outlet. While this peak and the other frequency peaks (St=0.042 and St=0.085) in Fig. 6.8 (b) could not clearly obtained in the picture of time history Fig. 6.8 (a).

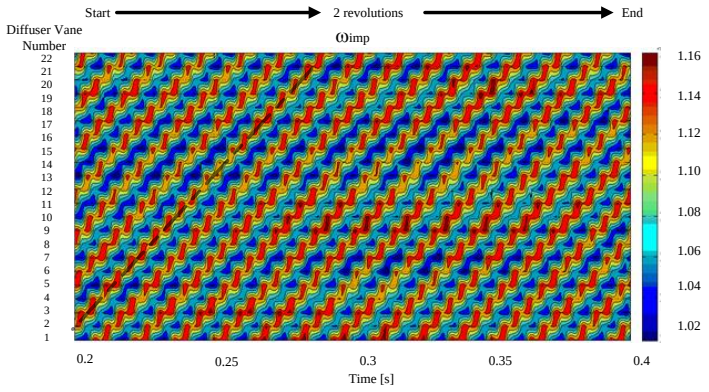

(a) Time history of total pressure in each diffuser channel

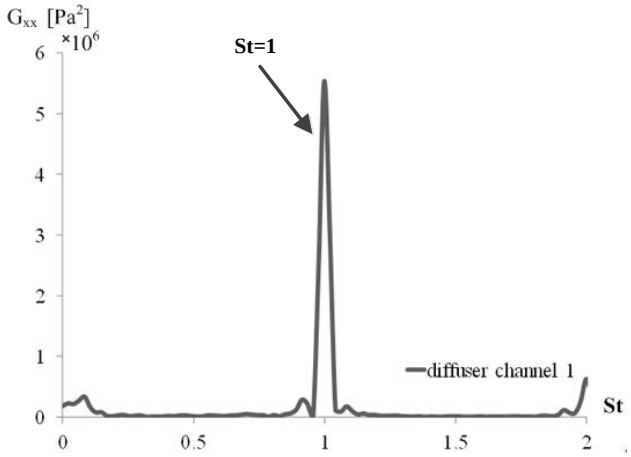

(b) Auto spectrum of total pressure in diffuser channel 1

Fig. 6.7 Total pressure at the inlet of diffuser channels

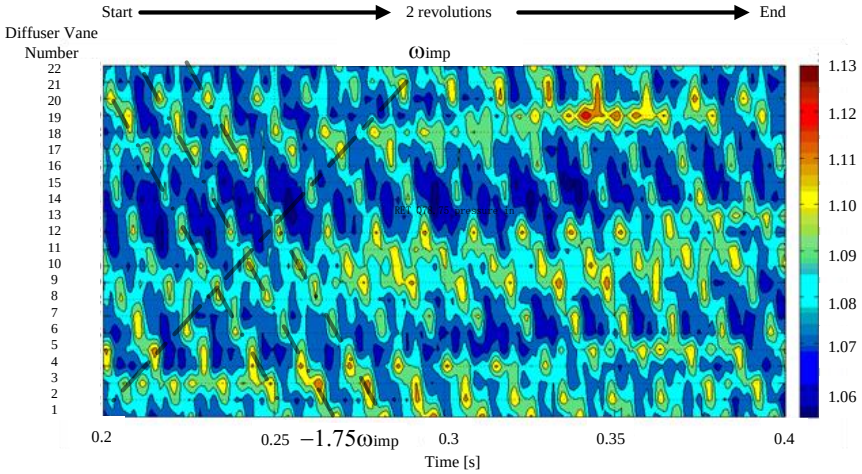

(a) Time history of total pressure in each diffuser channel

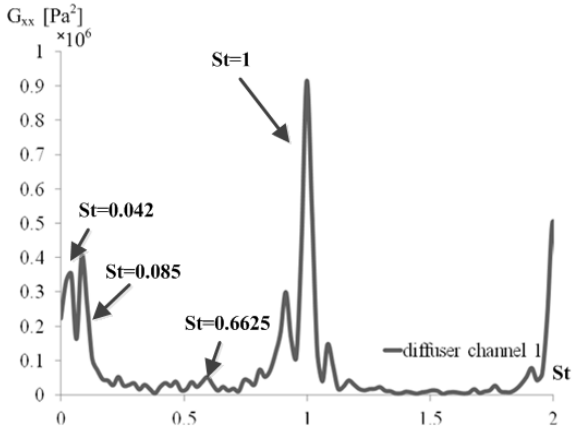

(b) Auto spectrum of total pressure in diffuser channel 1

Fig. 6.8 Total pressure at the outlet of diffuser channels

At the inlet of the return channel, the time history picture about the instantaneous total pressure was quite similar to the outlet of diffuser as shown in Fig. 6.9 (a). The rotating pattern with four cells in the reverse direction at $1.75\omega_{imp}$ still existed. While in the outlet of return vane channel there was not any rotating disturbance in Fig. 6.9 (b).

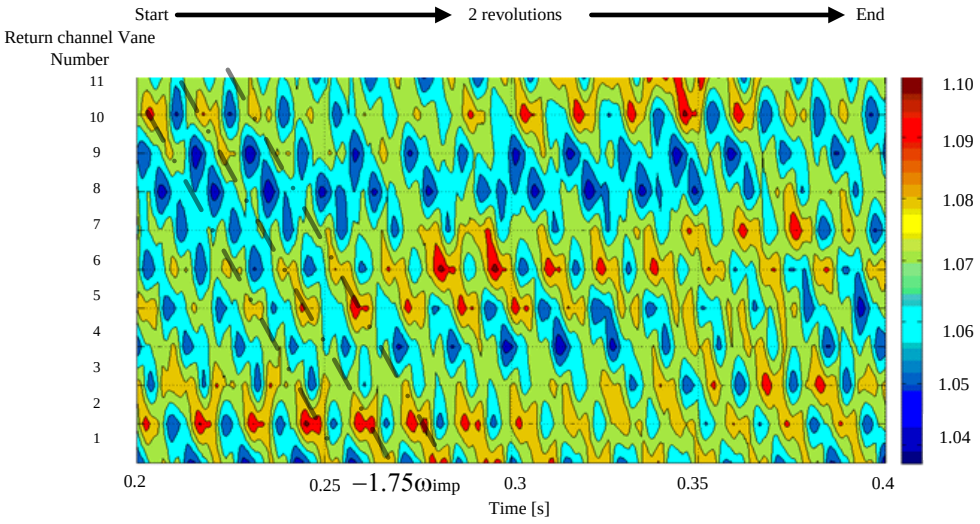

(a) at the inlet of return channel

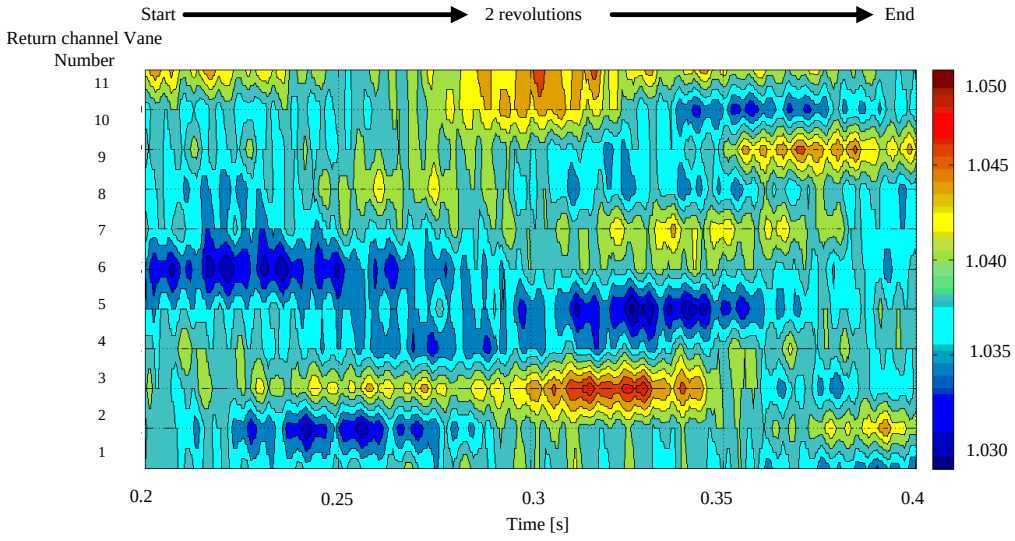

(b) at the outlet of return channel

Fig. 6.9 Time history of total pressure at the inlet and outlet of return channel

Meanwhile, the total pressure at the inlet and outlet of return channel in frequency domain show that the all pressure peaks were weaken when the flow flows past the return channel. Moreover, the peak at St=0.6625 disappears at the outlet of return channel (Fig. 6.10).

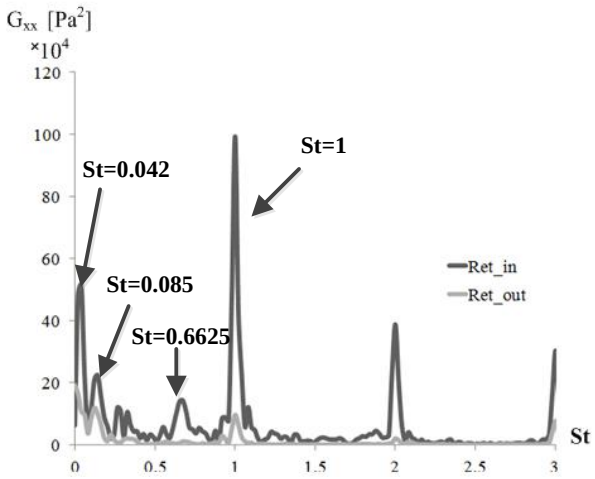

Fig. 6.10 Comparison of auto spectrum of total pressure at the inlet and outlet of return channel

Therefore, through the analysis on instantaneous total pressure at inlet of diffuser, the distribution of the total pressure was quite even, only a rotating disturbance caused by the rotating blade crossing the diffuser vane was detected (the peaks at impeller rotating frequency and BPF). At the same time, a rotating pattern was indicated at outlet of diffuser and the inlet of return channel. It has four diametrically cells and rotates at $1.75\omega_{imp}$ in the reverse direction which also contributes an obvious peak at BPF. However, the rotating pattern was not found at the outlet of the return channel and only some stable patterns were detected at this section.

6.1.3.3 The Analysis of the Instantaneous Flow Rate in Each Diffuser and Return Channel

The instantaneous flow rate at the inlet of diffuser was analyzed firstly. Figure 6.11 shows the auto spectrum in diffuser channel 1. It could be found that the frequency distribution of the flow rate was quite similar at the inlet and outlet of the diffuser vane channel. In addition to the BPF, other frequencies St=0.042 and St=0.085 were indicated.

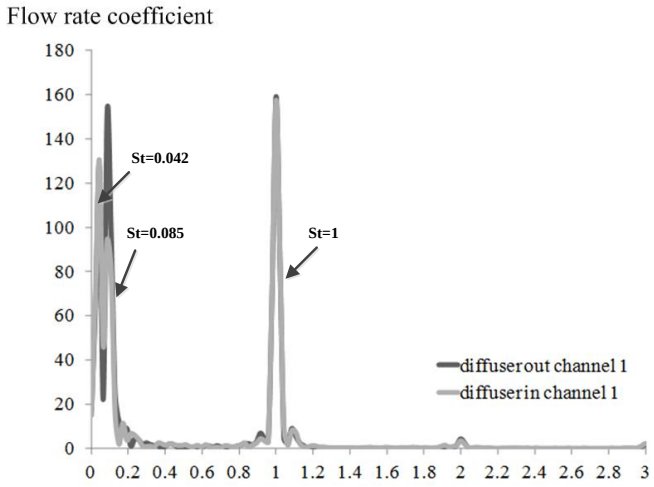

Fig. 6.11 The out spectrum of the instantaneous flow rate in the diffuser vane channel

Since the unsteady flow pattern mainly occurred at the first part of the return channel, the flow rate signal at outlet of diffuser was more sensitive to this unsteady pattern than at inlet, and the time wave was shown in Fig. 6.12. Two kinds of rotating encounter were found in this picture. They are a reverse rotating disturbance at 0.2 ω_{imp} with 3 cells and a forward propagated pattern with 4 cells at 0.073 ω_{imp}. They are contributed to the frequency peaks at St=0.085 and St=0.042 (in Fig. 6.12), respectively.

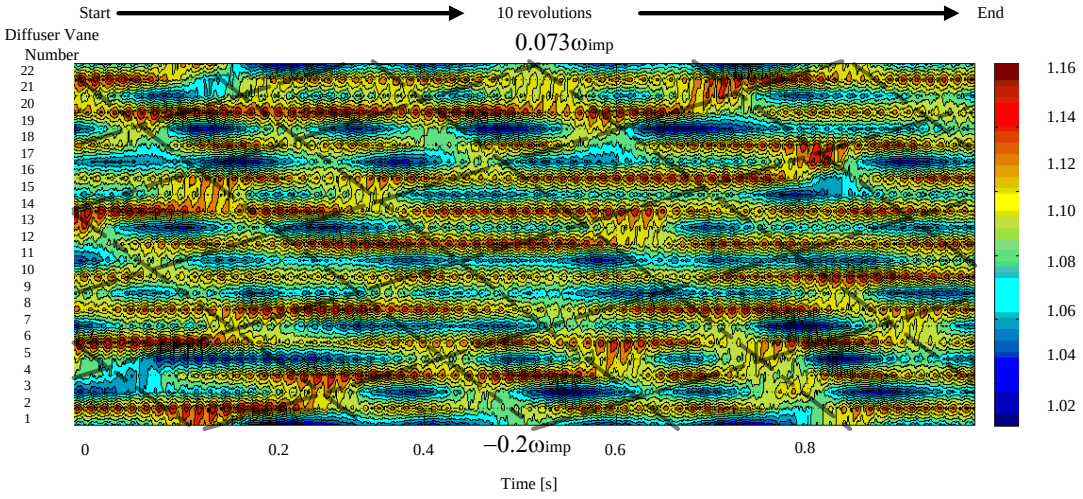

Fig. 6.12 The time wave of the instantaneous flow rate at the outlet of diffuser vane channel

There is a gap between the diffuser and return channel, some part of the flow from the diffuser and return channel would run into the next adjacent return channel as Fig. 6.13 shown. It is indicated that the fluid cross this face was quite unstable.

Near the hub and shroud, some fluid in the return channel near the inlet run to the next adjacent return channel.

In order to evaluate the leakage that flows into the adjacent channel, a leakage monitor face (the yellow face in Fig. 6.14) was built, and the flow rate crossing the face was monitored by time.

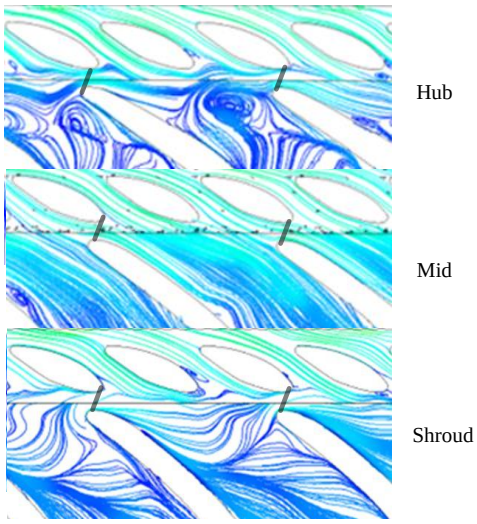

Fig. 6.13 Velocity streamlines on the sections of different span

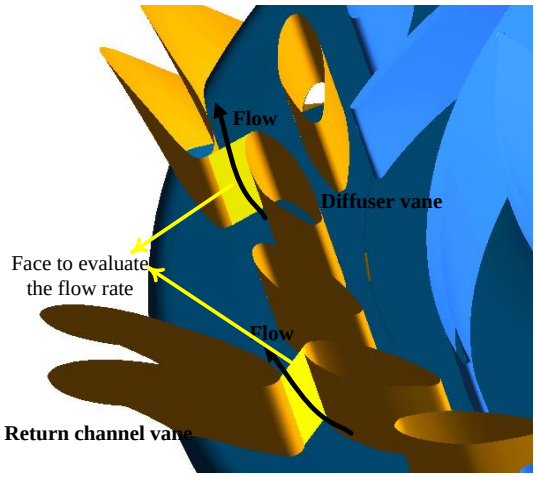

Fig. 6.14 Face built for monitoring the flow rate run into adjacent return channel form diffuser

The time wave of the flow rate observed from these faces was shown in Fig. 6.15 (a). The reverse rotating disturbance at $0.2\omega_{\mathrm{imp}}$ which was detected at the outlet of diffuser channel was also indicated while the forward rotating pattern with 0.073 ω_{imp} disappeared.

Thus, the rotating pattern with 0.073 ω_{imp} has greater impact on the flow rate in diffuser channel than return channel. Moreover, it also has greater impact near the inlet of the diffuser due to the flow rate amplitude of St=0.042 was stronger at the inlet than outlet of diffuser (in Fig. 6.11).

At the same time, the rotating disturbance at 0.2 ω_{imp} was detected at the inlet of return channel, as shown in Fig. 6.15. Thus, for the analysis of flow rate in diffuser and return channel, it could be found that this disturbance at St=0.085 has greater impact in the return channel than diffuser. This would explains why the amplitude of St=0.085 is stronger at the outlet than inlet in diffuser as shown in Fig. 6.11.

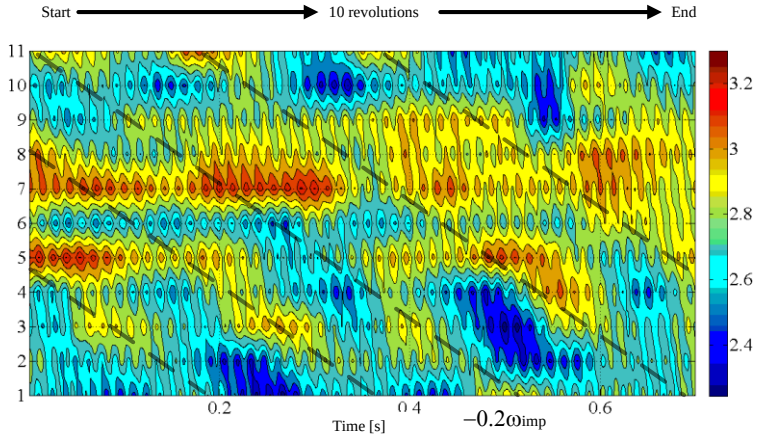

(a) Time history of flow rate in each monitor face

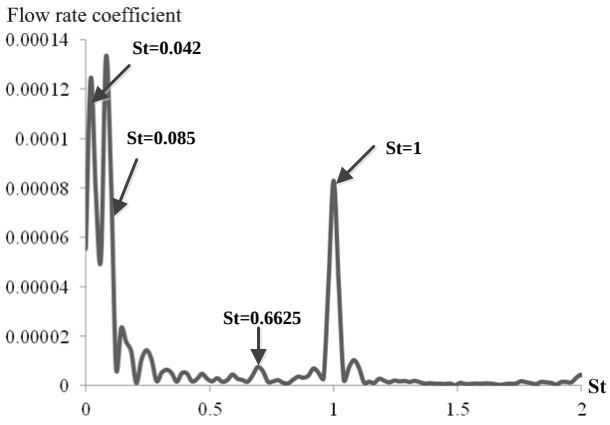

(b) Auto spectrum of flow rate in each monitor face

Fig. 6.15 Flow rate on the monitor face

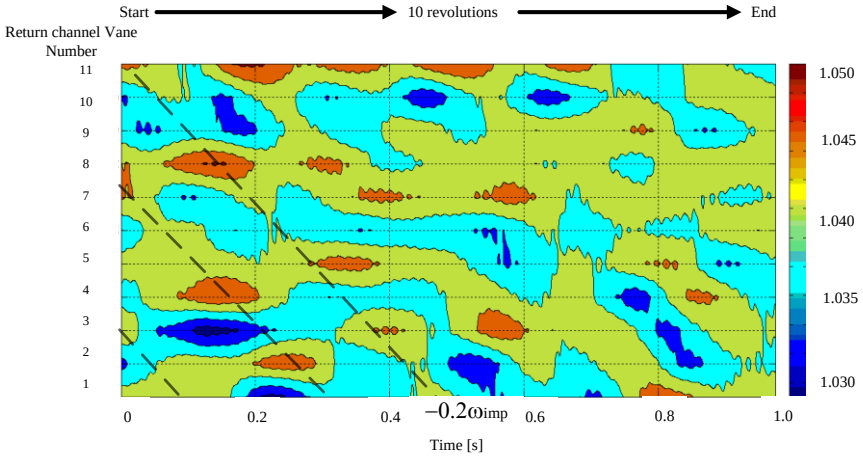

Fig. 6.16 Time history of flow rate at the inlet of return channel

6.2. Unsteady Disturbance in Impeller

Although the flow field in impeller was even at full load condition, the pressure inner it was also influenced by the unsteady flow from the return channel by the pressure analysis in frequency domain.

The pressure spectra from the pressure monitors (Fig. 4.3) inside the impeller in the rotating reference from hub to shroud span was drawn in Fig. 6.17. Near the trailing edge, there was a peak around St=1.579 (110Hz, n_{b4}×f_{IR}) which was caused by the rotor and stator interaction. Fig. 6.17 also indicates that there were several peaks at frequencies bellow St=1.579. Some of them were the harmonics of f_{IR}, some other peaks were not the harmonics of f_{IR} such as St≈0.335 and 0.66.

Furthermore, by the high order analyses, a non-linear frequency component was detected near St≈0.335 except St≈1.579 and f_{IR} as shown in Fig 6.18. In the relative system of reference, the Strouhal number could be expressed by(Cavazzini 2006, Pavesi, Cavazzini et al. 2008):

$$\mathrm{St}_{\mathrm{relative}} = \frac{m}{n_b} - \mathrm{St}_{\mathrm{absolute}} \tag{6-7}$$

By the calculation, the number of modes m, matching $\mathrm{St}_{\mathrm{relative}}$≈0.335, was 7. Moreover, the corresponding $\mathrm{St}_{\mathrm{relative}}$ was around 0.6625 which was consistent with periodical disturbance occurs in return channel. In addition, the peak around St≈0.66 in the rotating frame was the non-linear interaction component by St≈0.344 and BPF.

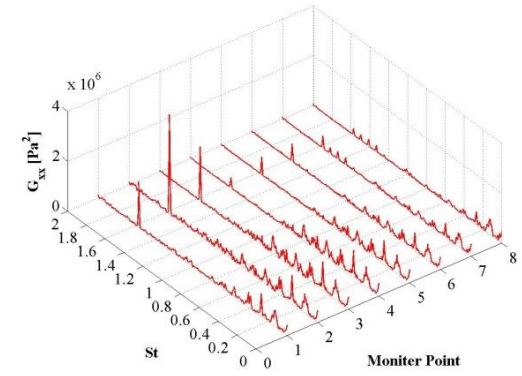

(a) Pressure side - hub

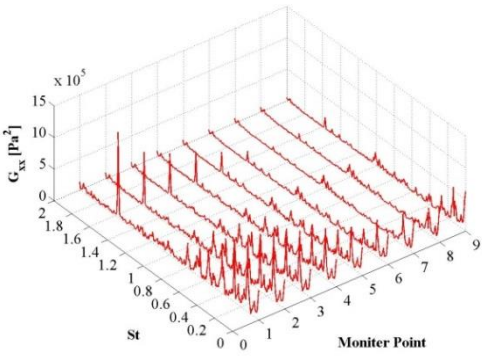

(b) Suction side - hub

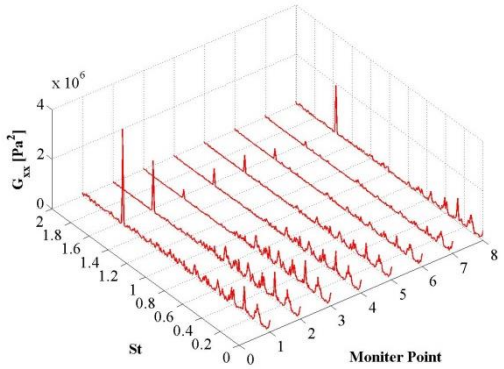

(c) Pressure side - mid

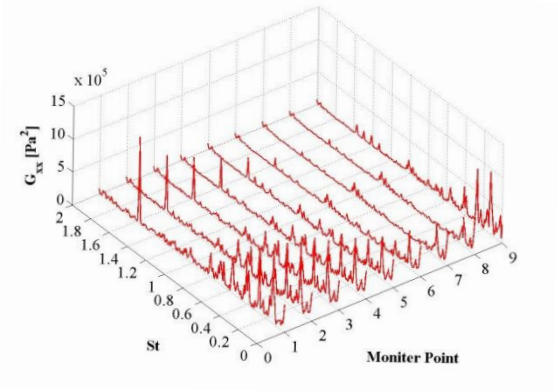

(d) Suction side - mid

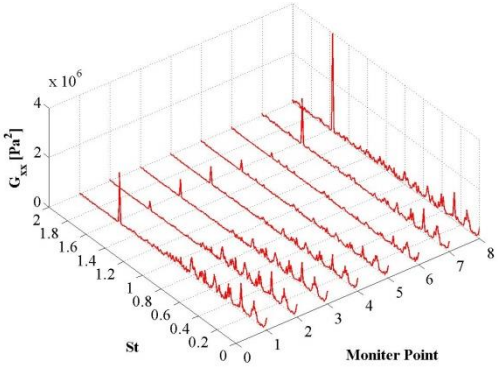

(e) Pressure side - shroud

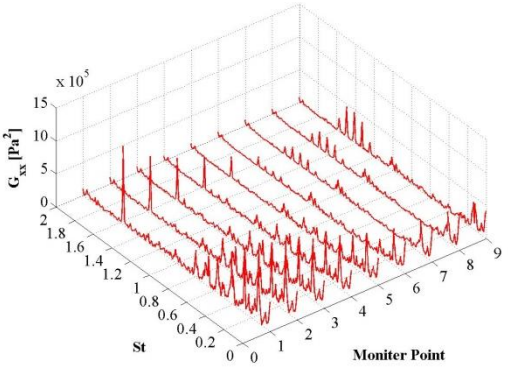

(f) Suction side - shroud

Fig. 6.17 The spectrum of pressure in impeller blade

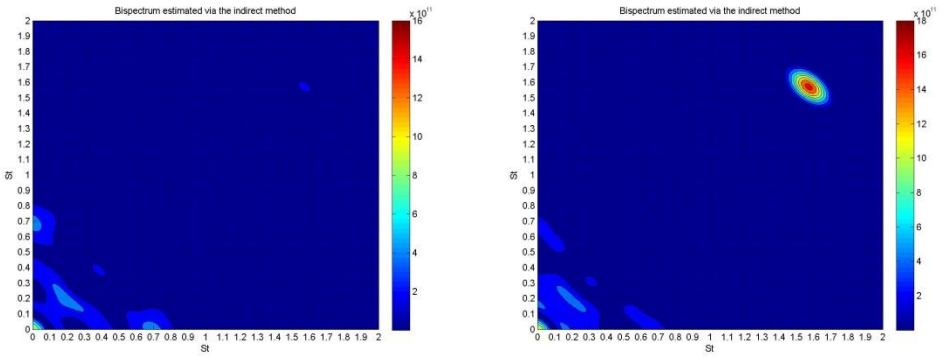

(a) No. Pre 24 (b) No. Suc 22

Fig. 6.18 Pressure Bispectrum at pressure side (a) and suction side (b) of impeller at full load

6.3 Intensity of Dipole Sources in Return Channel

In this section, the acoustic effect of the diploes sources in return channel and diffuser was analyzed. The forces on the surface of diffuser and stay vane cause the dipole source by flow fluctuations. The data transform was conducted for the dipole source. Fig. 6.19, 6.20 and 6.21 are the distribution of intensity of dipole sources at three different frequencies (St=0.143, St=0.6625 and St=1).

It could be found that the impeller passage frequency also plays a remarkable role in the unsteadiness, which occurs in the return channel suction side in Fig. 6.19. Although the St=0.6625 was found in experimental and numerical results, but in the simulation results, the intensity at this frequency was weaker than the intensity at impeller passage frequency and BPF (Fig. 6.20). Compared with Fig. 6.19 and 6.20, it could be found that the BPF plays the key role in intensity of the dipole source at full load, although some other disturbance was detected by experimental and numerical results such as St=0.6625.

Fig. 6.19 Intensity of dipole source at St=0.143 at full load

Fig. 6.20 Intensity of dipole source at St=0.6625 at full load

Fig. 6.21 Intensity of dipole source at St=1 at full load

6.4 Conclusions

Through the above analysis, the unsteady flow at design flow rate, which occurred in return channel, includes several periodic fluctuations. The fluctuations at St=0.042, St=0.085, St=0.6625 and St=1 were found in this region. The intensity of these unsteady patterns mainly presents to be strongest near hub. By the analysis both in time and frequency domain, rotating propagation characters were found in some frequencies, and listed as below:

Table 6.1 Information about the rotating propagation characters at full load

Frequency(St)	Rotating	Propagate Direction	Speed(ω_{imp})	Number of Cells
0.042	Yes	Forward	0.073	4
0.085	Yes	Backward	0.2	3
1	Yes	Forward	1	7
1	yes	Backward	1.75	4

Although several periodic unsteadiness were found at full load, based on the acoustic analysis in diffuser and return channel, it was found that the intensity of acoustic pressure at BPF plays a critical role in the contribution of intensity of the dipole sources at full load.

Furthermore, by the pressure analysis in the impeller, it could be found that although the unsteady disturbance with frequency St=0.6625 occurs in return channel, this disturbance impacts the pressure field in impeller at full load.

Chapter 7 Unsteady Flow Patterns at Part Load Conditions

7.1. Unsteady Disturbance in Impeller

Based on the analysis in the previous chapters about experiment and numerical simulation, the peak of St=0.6625 in frequency domain, which is detected in a wide flow rate range, even at full load condition, is proven to be caused by a periodic unsteady flow which occurs in the return channel.

Meanwhile, with the decrease of flow rate, another nonlinear frequency component at St=0.335 was found in first part of the *Q-H* instability region. However, the origin of this unsteady pattern is still unknown.

With the reduction of flow rate, the flow in the impeller starts to be more non-uniform, several types of unsteady flow patterns may appear in the impeller such as the jet-wake at the outlet, the flow recirculation, cavitation at the inlet of impeller, and rotating stall etc. These unsteady patterns are all likely to affect the performance characteristics, and lead to the saddle-instability region, which appears in the *Q-H* curves.

However, for the test pump, it is not sure what really happened with the reduction flow rate and which kind of unsteady pattern cause the nonlinear frequency components of St=0335. In order to identify the unsteady patterns at part load condition, an in-depth analysis is needed by comparing the results of experiment and numerical simulation.

7.1.1 Qualitative Analysis on the Fluid Status in Impeller

When the flow rate was below the BEP (best efficiency point), with the reduction of flow rate, the approach flow velocity vector from the outlet of impeller become to not match with the shape of diffuser inlet. This phenomenon could cause the increased shock losses and non-uniform distribution of flow at the outlet of impeller and inlet of diffuser. Additionally, the stalled flow acts like a change in blade profile to which the streamlines can often adapt. Thus, the streamlines in impeller and diffuser were illustrated together to help identify the unsteady pattern which occurs in impeller at part load as shown in Fig. 7.1, 7.2 and 7.3.

Compared with the flow field at full load condition, a flow separation occurred on each impeller suction side at 0.674 Q_{Des} (Fig. 7.1). The separation started at the shroud of blade suction side. The separation gradually weakened from shroud to hub, propagated downstream along the impeller suction side, and was dissipated around the mid span finally.

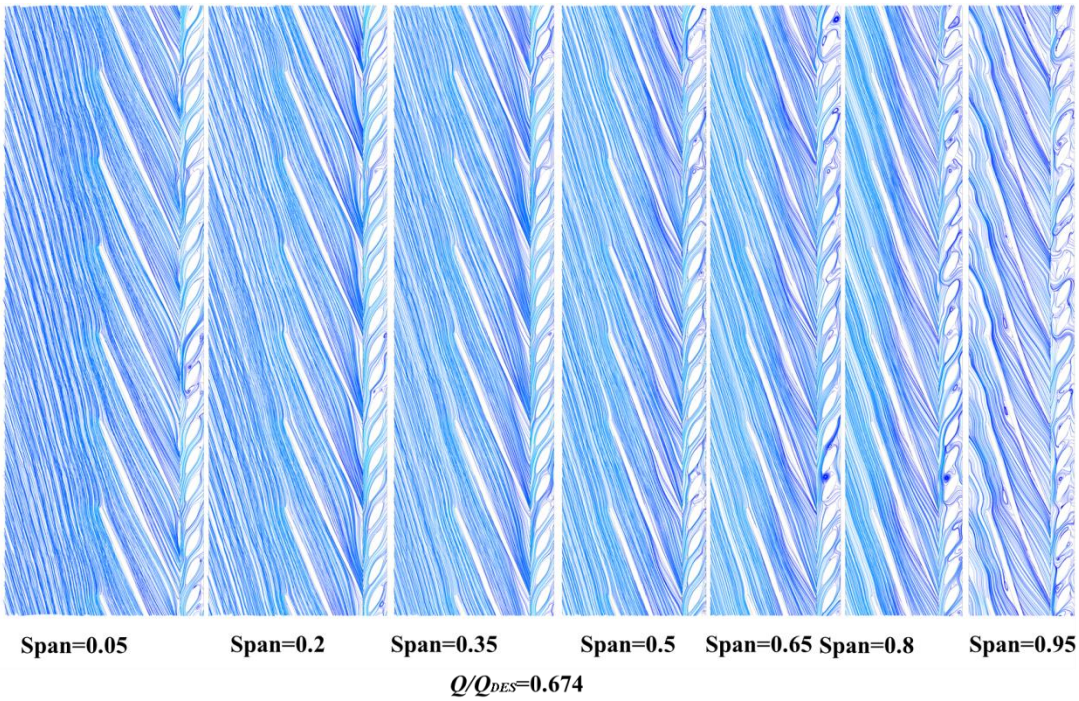

Fig. 7.1 Streamlines at different crosswise spans of impeller and diffuser at 0.674 Q_{Des}

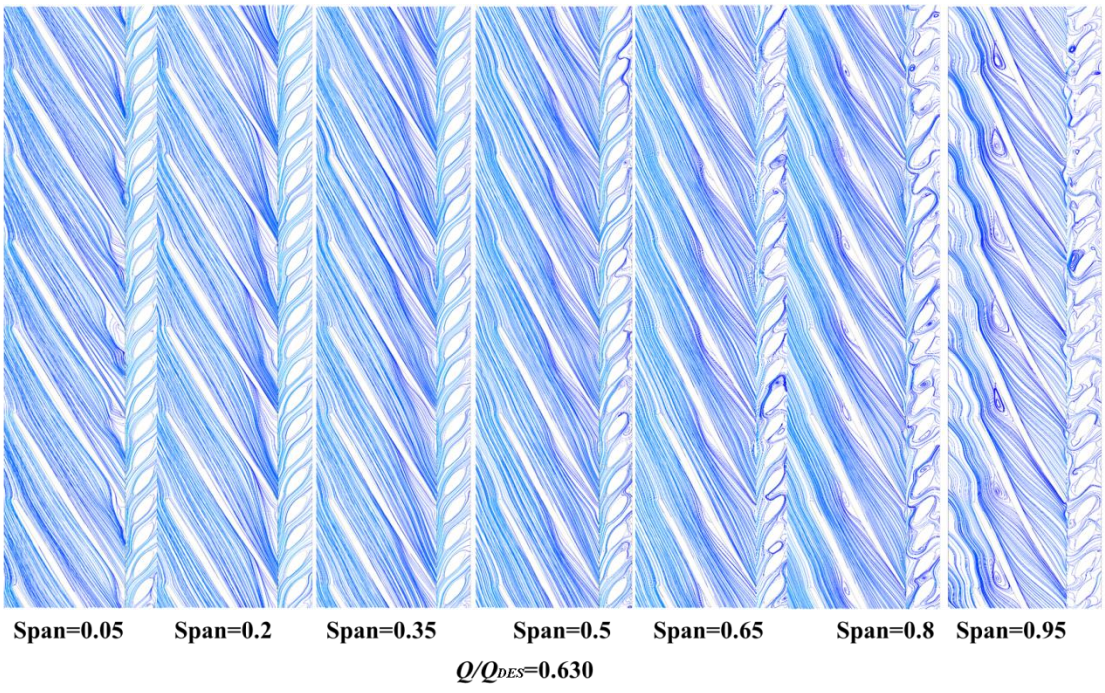

Fig. 7. 2 Streamlines at different cross sections of impeller and diffuser at 0.630 Q_{Des}

At this condition, at the outlet of the impeller and the inlet triangle area of diffuser, flow separations, recirculation and vortices were all found. The separations blocked some diffuser channels on the cross section near the shroud. Additionally, the wake was found near the trailing edge of impeller blade suction side at the cross section near the hub.

With the reduction of flow rate, the flow separations, recirculation and vortices near the outlet of impeller were more remarkable at 0.630 Q_{Des}, and the flow status in impeller was summarized as below:

Flow separations occurred at the leading edge of each blade suction side near the shroud, propagated along the blade to the downstream, and gradually weakened from shroud to hub.

Near the outlet of impeller, a wake-jet pattern has been found at the trailing edge of impeller blade, and it weakened from hub to shroud. Additionally, a recirculation has been detected in the inlet area of diffuser at the cross section near shroud. It was a joint working of two different unsteady patterns in the diffuser, which were marked by letter A, and B in Fig. 7.4. A is the unsteady flow near the inlet of diffuser, and B is the dramatic unsteady patterns which flow back from the return channel. With the development of these unsteady flows, they mixed together and caused blockage near the throat of adjusted vane.

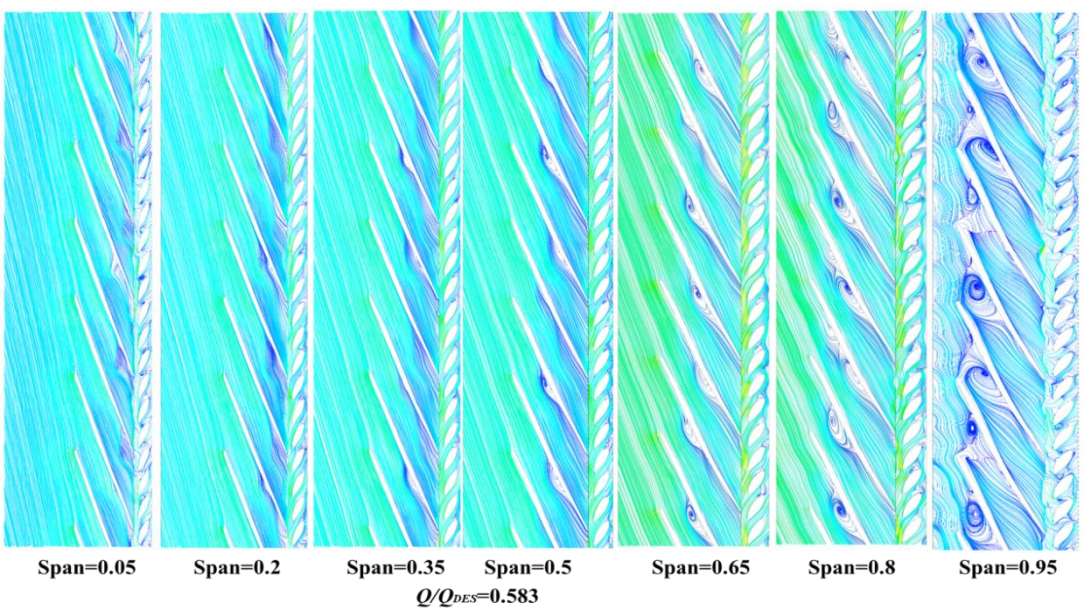

Fig. 7.3 Streamlines at different cross sections of impeller and diffuser at 0.583 Q_{Des}

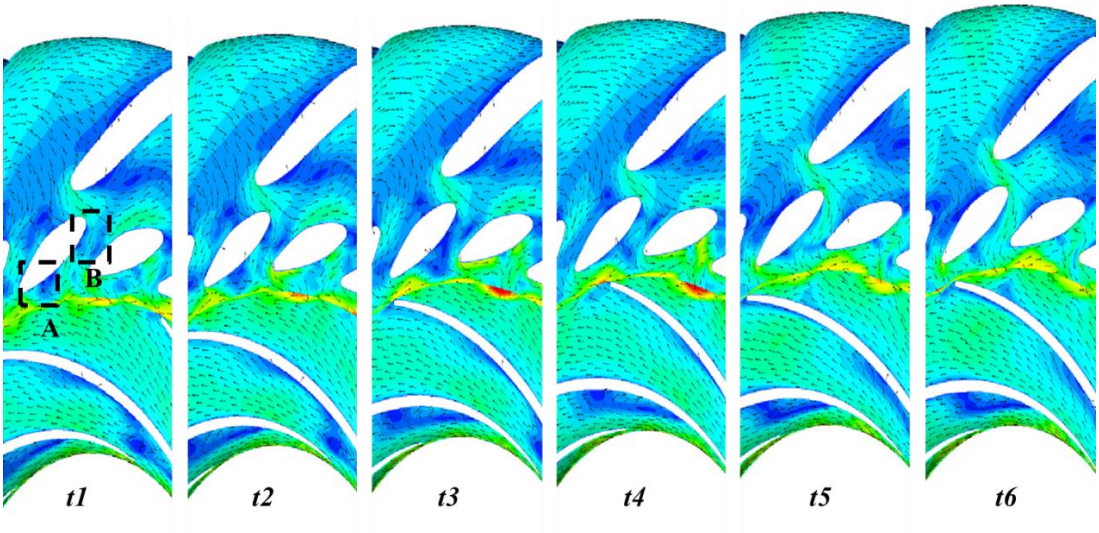

Fig. 7.4 Part of flow field at near shroud cross sections at 0.674 Q_{Des}

With the further reduction of flow rate, the flow in the impeller becomes more uneven as shown in Fig. 7.3 at 0.583 Q_{Des}. The unsteady flow near the trailing edge of blade became stronger. Furthermore, near the impeller inlet, two flow separations appear at the suction side in some channel and block the inlet of impeller blade channel near the shroud. Combined with Fig. 7.5, it could help to understand the development of the flow field in impeller. At the blade suction side, the flow separation and wake were more severe with the reduction of flow rate. With the development of the wake and the flow separation, they mixed together on some cross sections around the middle of blade.

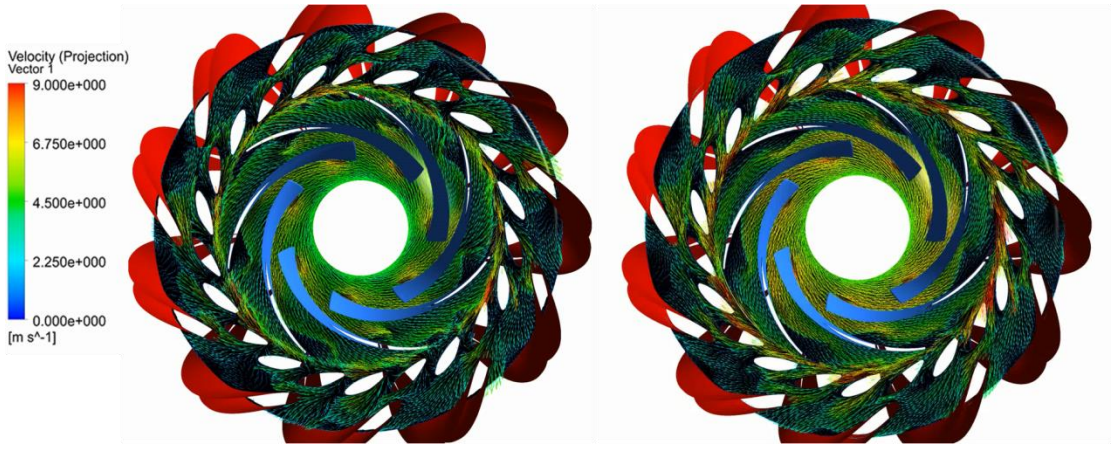

Fig. 7.5 Stream plots at different cross sections of impeller and diffuser at 0.583 Q_{Des}

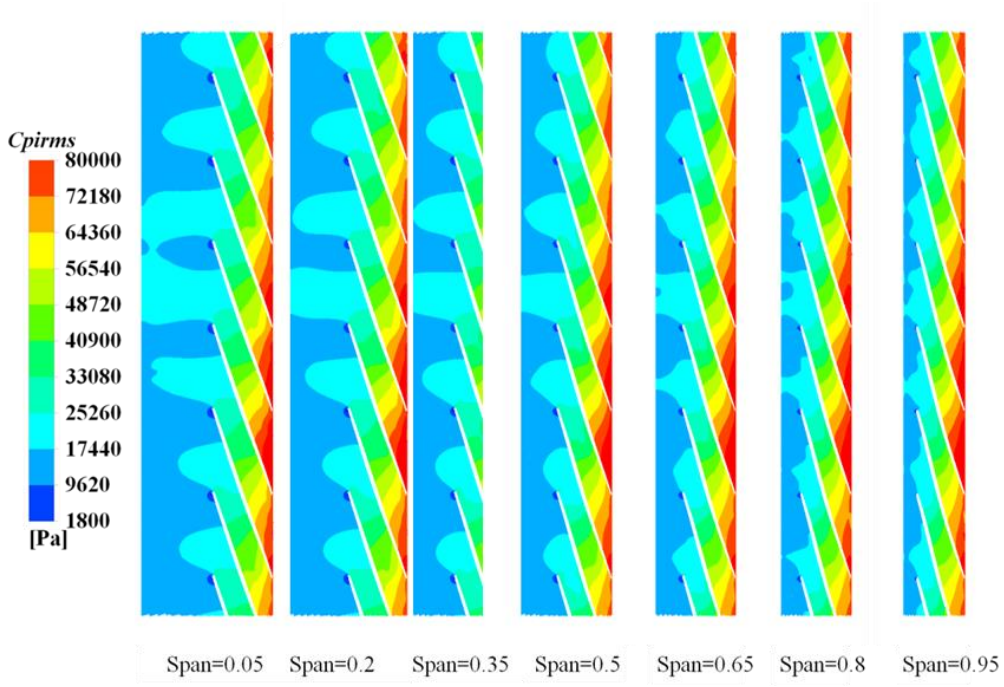

(a) Time record: 0.1s

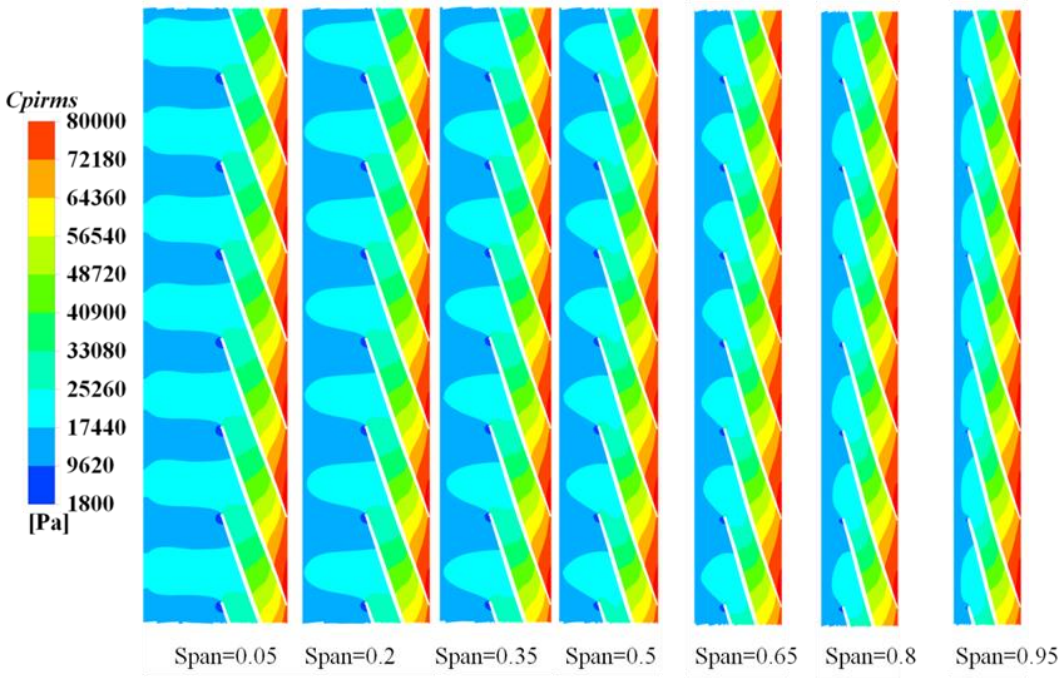

(b) Time record: 1s

Fig. 7.6 Distribution of C_{pirms} in impeller at 0.583 Q_{Des}

In order to identify the time scale of these unsteady flows in impeller, the root mean square of the pressure coefficient for different time records (0.1s and 1s) were calculated, and the distributions of C_{pirms} in impeller at 0.583 Q_{Des} were shown in Fig.

7. 6. It is indicated that the distribution of C_{pirms} in the blade channels were even in different time records. Near the inlet of impeller, the distribution of C_{pirms} is uneven in the time records 0.1. With the increasing of the time record, the distribution became even in the inlet when the time record is 1s. Thus, although the instantaneous flow in the impeller became more intense, the unsteady flows in impeller were periodic. Furthermore, near the inlet of diffuser, there was a periodic unsteady flow which frequency is smaller than 10Hz and larger than 1Hz.

7.1.2 Pressure Analysis on the Fluid Status in Impeller

The pressure signals from one impeller blade at 0.584 Q_{Des} were illustrated in frequency domain as shown in Fig. 7.7. The obvious peaks were found at St=1.579 due to the rotor and stator interaction. Remarkable peaks were also found below St=1.579 at the frequencies such as St around 0.34, 0.66 and 0.81 in the most of pressure monitors. Furthermore, on the leading edge of blade, there were several peaks smaller than St=1.579. These frequency peaks are discussed in the section 7.1.3.

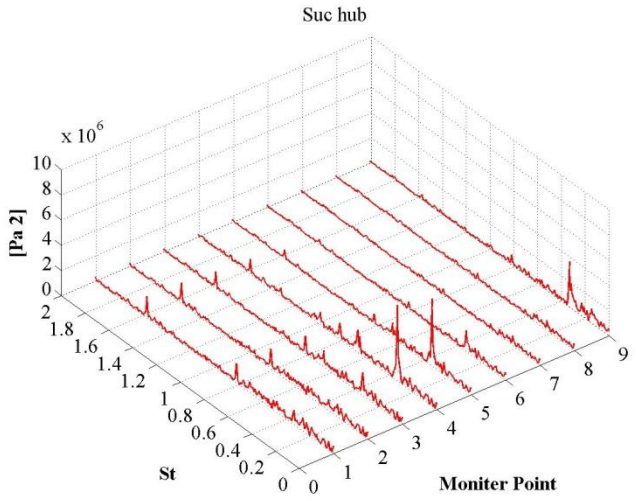

(a) The pressure on the blade suction side near hub

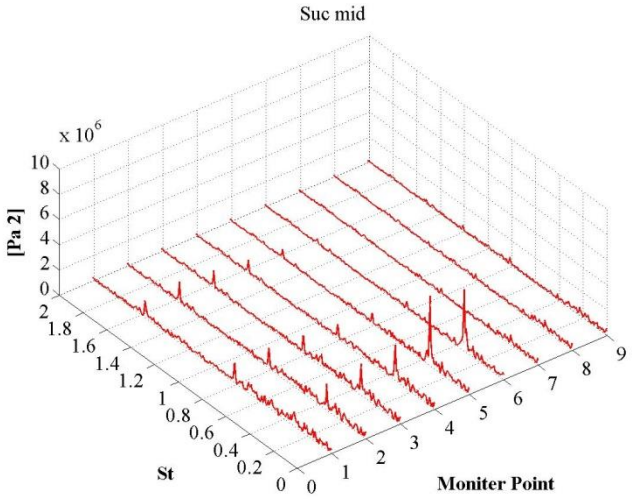

(b) The pressure on the blade suction side at mid span

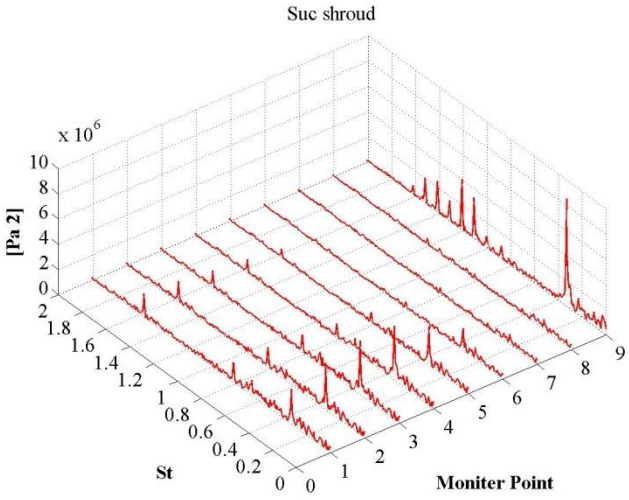

(c) The pressure on the blade suction side near shroud

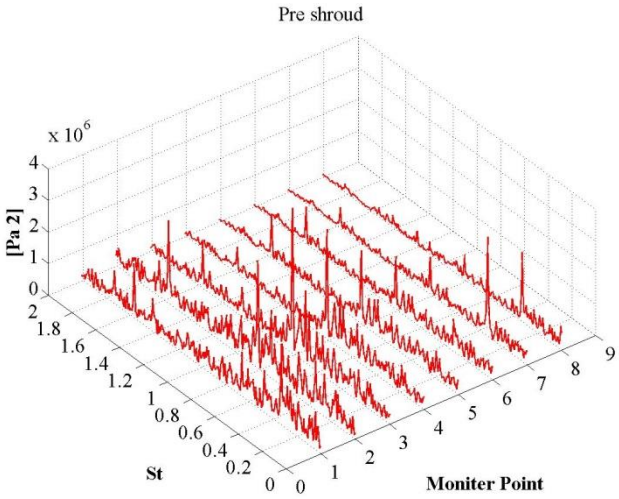

(d) The pressure on the blade pressure side near shroud

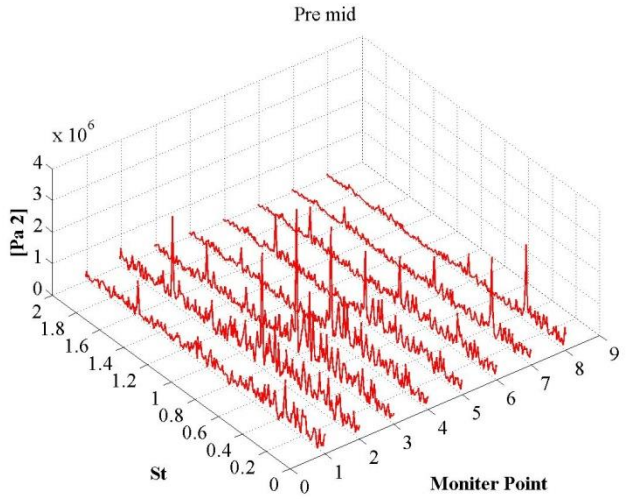

(e) The pressure on the blade pressure side at mid span

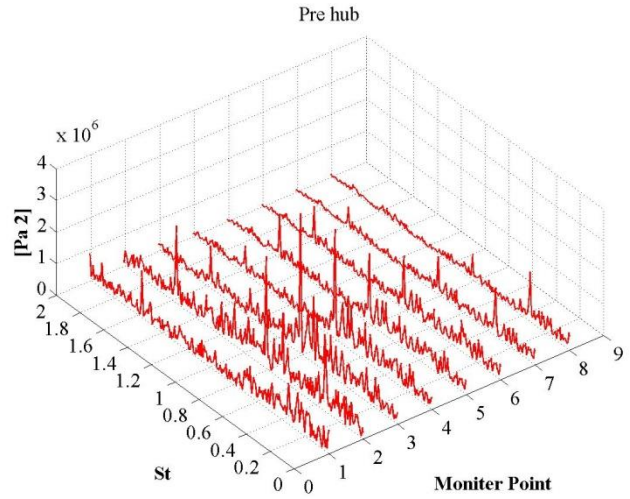

(f) The pressure on the blade pressure side near hub

Fig. 7.7 Auto spectrum of the pressure from the pressure monitors on one impeller blade at 0.584 Q_{Des}

By the high order analyses, the bispectrum results of pressure monitors in one blade at mid span were shown in Fig 7.8. It could be found that, except St=1.579 and f_{IR}, non-linear frequency components (St=0.34 and St=0.81) were found in the suction side of blades. The main component is St = 0.34 on this side which appear in most of the monitors. For St=0.81, it appeared near the trading edge.

In the pressure side of blade, St=0.81 was the main non-linear frequency component and St=0.41 (about half of St=0.81) was the second non-linear frequency component from the trailing edge to the throat area of blade. As the monitors closer to

the leading of blade, the intensities caused by St=0.81 and St=0.41 reduce and St around 0.34 become the strongest component as shown in Fig. 7.8 (o) Pre27.

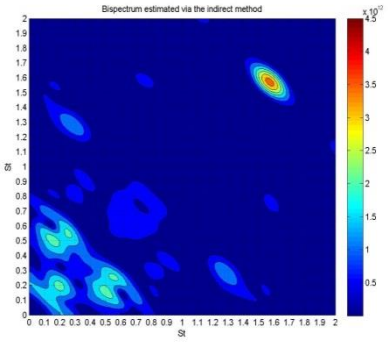

(a) Suc 21

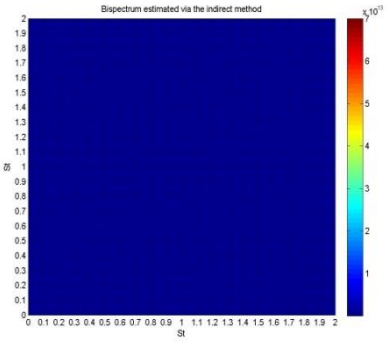

(i) Pre 21

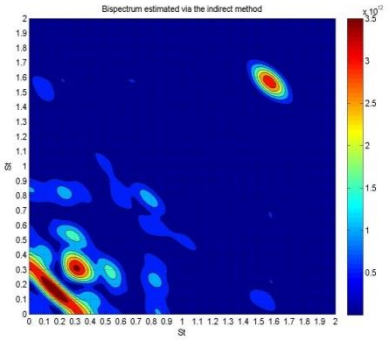

(b) Suc 22

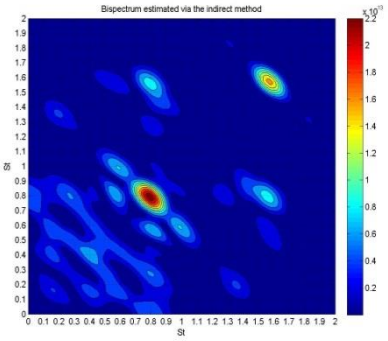

(j) Pre 22

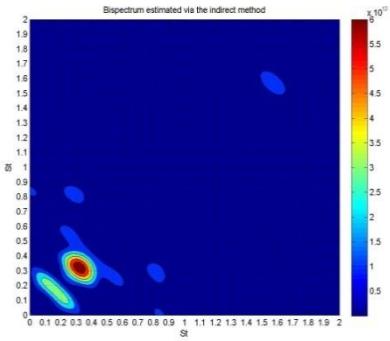

(c) Suc 23

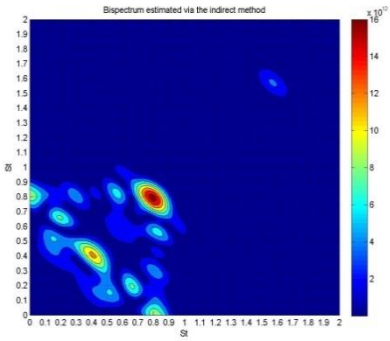

(k) Pre 23

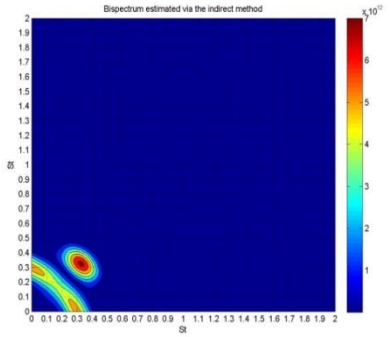

(d) Suc 24

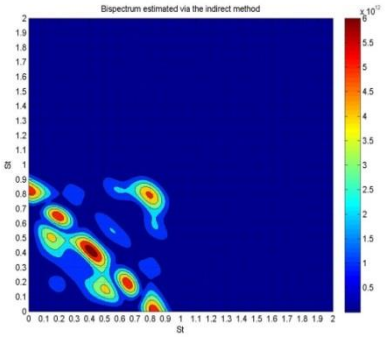

(l) Pre 24

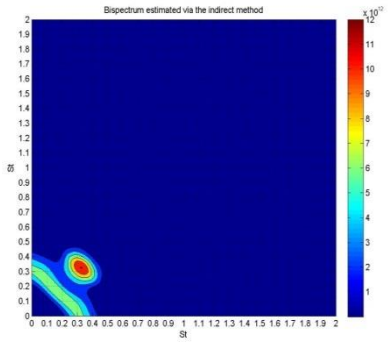

(e) Suc 21

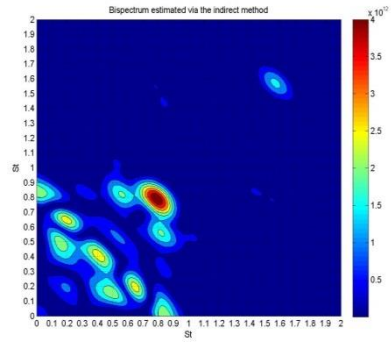

(m) Pre 25

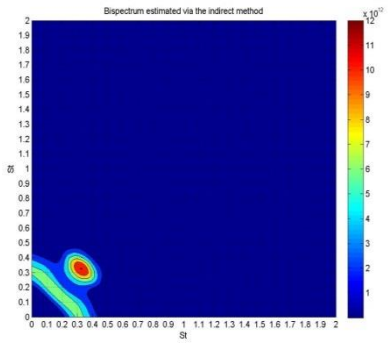

(e) Suc 21

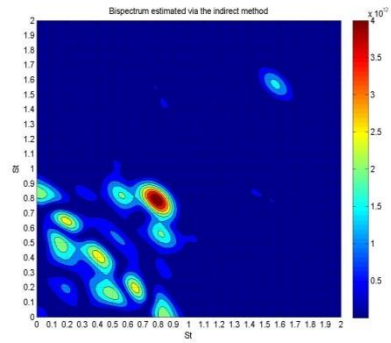

(m) Pre 26

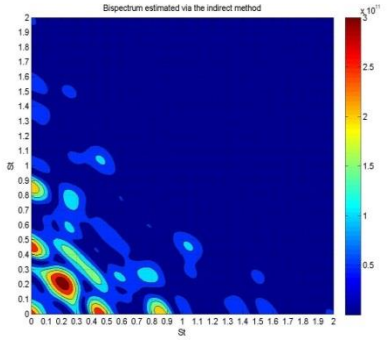

(g) Suc 27

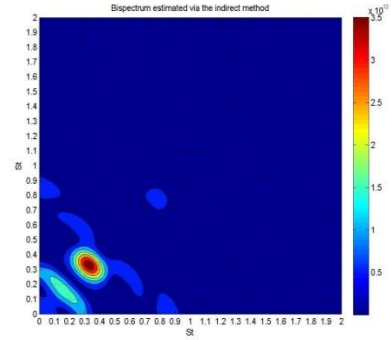

(o) Pre 27

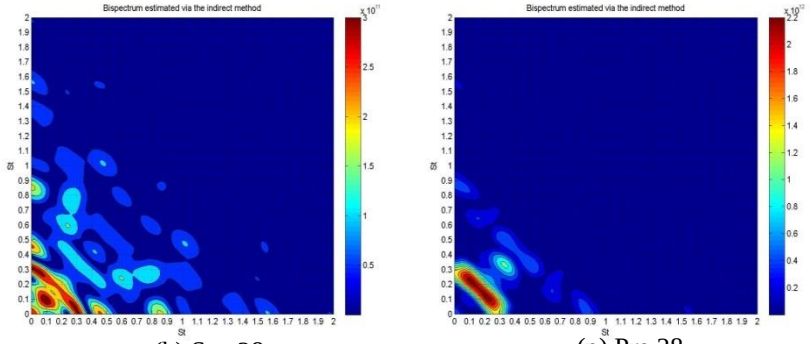

(h) Suc 28 (p) Pre 28

Fig. 7.8 Pressure Bispectrum at pressure side (a) and suction side (b) of impeller at 0.584 Q_{Des}

In the last chapter, it is indicated for the non-linear frequency component around 0.344, the corresponding St in static frame is around 0.6625. At the same time, the absolute St Number for 0.81 was calculated by Eq. (6-7): the number of modes *m*, matching $St_{relative} \approx 0.81$, was 8, and the corresponding $St_{absolute}$ is around 0.335.

The intensity of the fluctuation (St=0.3325 in rotating frame) which changes with the location of monitor at 0.584 Q_{Des}, was drawn in Fig. 7.9. It is indicated that the trend of this amplitude both on the pressure and on suction side matches exactly with the development of the flow separation which inception occurs near the throat of the blade suction. The detail of this flow separation is described as bellow:

The significant amplitudes of this frequency were mainly detected from the pressure monitors on the blade suction side (Fig. 7.9 (a)). The reason for this result is that a flow separation occurs at the throat of blade suction side near shroud while the operating condition falls into the saddle-instability region.

Because the strength of this unsteady pattern is strongest near the shroud cross section and gradually weakens to hub, the pressure amplitude at the corresponding frequency is greatest near the shroud.

At 0.584 Q_{Des}, near the leading edge of the blade suction side, with the fully development of the flow separation, the blockage appears at the inlet of impeller blade channel near shroud. At this cross span position, the separation occupied the whole blade channel as shown in Fig. 7.4 (span=0.95), and this is the reason of the high peak value at St=0.335 near the leading edge of blade pressure side (see Fig. 7.9 (b) shroud point 7).

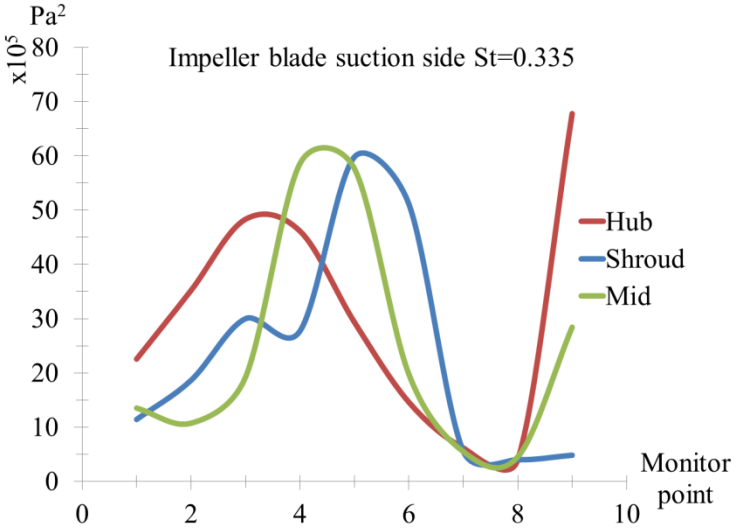

(a) Suction side

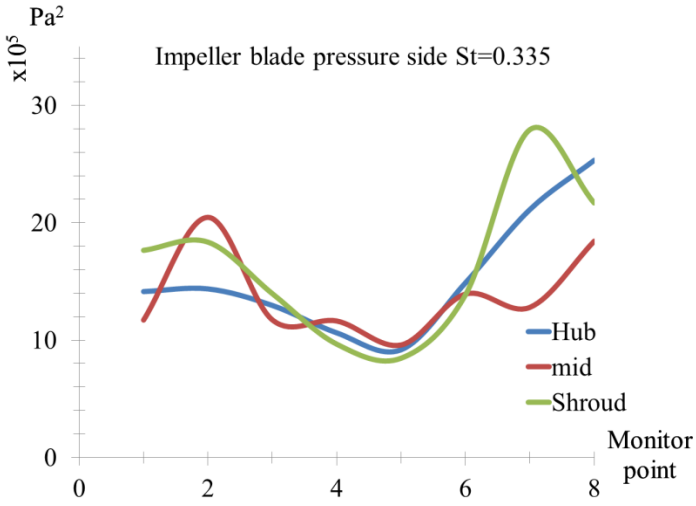

(b) Pressure side

Fig. 7.9 Pressure amplitudes of each monitors at St=0.335 in rotating frame on the impeller blade at 0.584 Q_{Des}

Furthermore, the intensity of the dipole sources in impeller was analyzed. Fig. 7.10 shows the intensity of dipole sources at St=0.335 in the rotating frame and the high pressure regions on the blade suction side were also in a good accord with the occurrence position of the flow separation. Thus, the periodic unsteady pattern at St=0.335 (in the rotating frame) was a small scale of unforced unsteadiness which incepts at the inlet of blade suction side near shroud. At the same time, this acoustic distribution also indicates the effect of the unsteady pattern at St=0.335 (in the rotating frame).

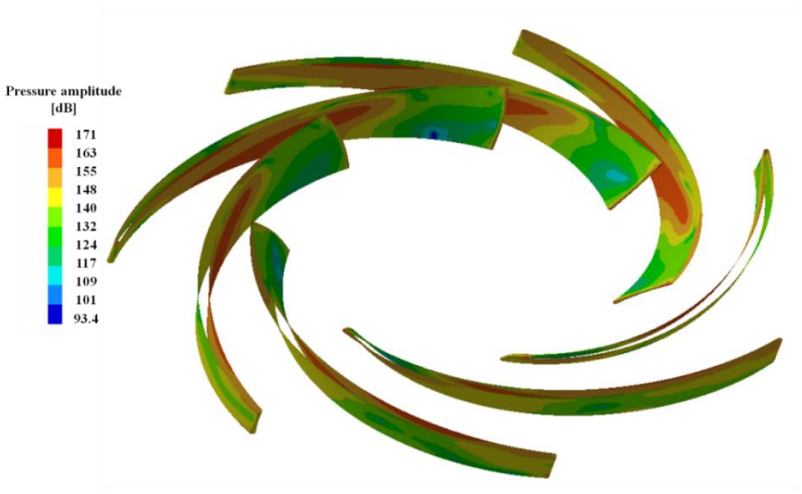

Fig. 7.10 Intensity of dipole source on the impeller blade surface at St=0.335 in rotating frame at 0.584 Q_{Des}

The intensity of the fluctuation (St=0.81 in rotating frame) changing with the different location of monitors at 0.584 Q_{Des}, was drawn in Fig. 7.11. The distribution of the pressure amplitude at this frequency was quite the same on these three different cross span sections. The maximum value of this frequency appeared near the outlet of the impeller. Meanwhile, Fig. 7.4 indicates that this region occurred severe wake-jet pattern at this condition. Thus, the frequency peak at St=0.81 was mainly caused by the wake-jet around the trailing edge of blade. With the propagation to the upstream, the influence of this pattern weakens gradually.

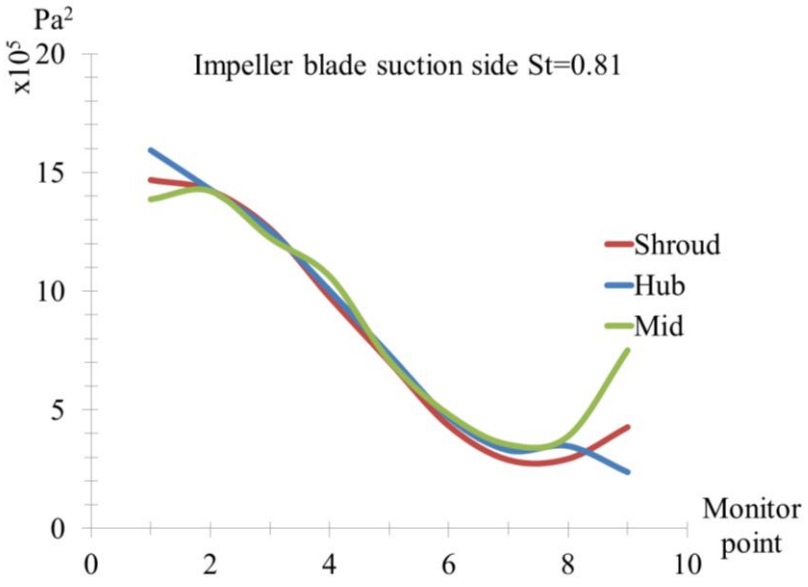

(a) Suction side

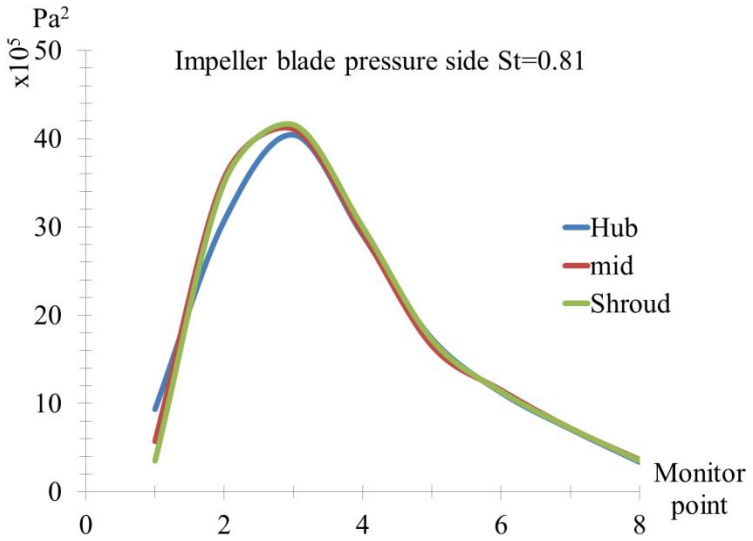

(a) Pressure side

Fig. 7.11 Pressure amplitudes of each monitors at St=0.81 on the impeller blade at 0.584 Q_{Des}

Additionally, the intensity of the diploes sources on this frequency in impeller was analyzed, Fig. 7.12 shows the intensity of dipole sources at St=0.81. In this picture, high pressure region appeared near the trailing edge both on pressure and suction side which was in a good accord with the trend in Fig. 7. 11. And this location is the wake-jet region of the impeller. Thus, wake-jet near the trailing edge of the impeller blade caused a pressure disturbance at St=0.81 in rotating frame. The corresponding absolute St Number was calculated by Eq. (6-7). It is St=0.335 in static frame which agree with one of the main non-linear frequency components in diffuser and m=8. Thus, it could be concluded that the disturbance with St=0.335 in the diffuser may be caused by the wake-jet of impeller.

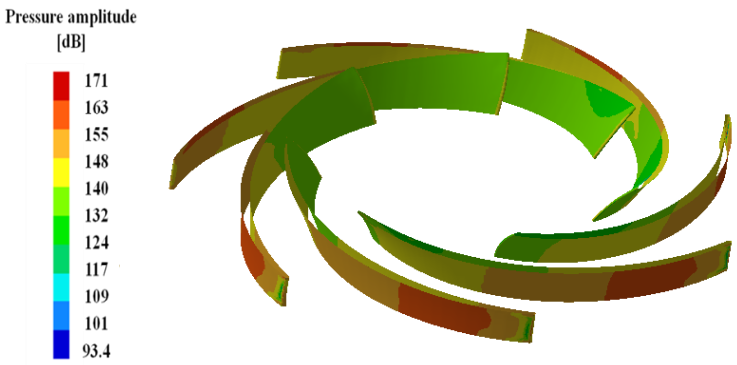

Fig. 7.12 Intensity of dipole source on the impeller blade surface at St=0.81 at 0.584 Q_{Des}

7.1.3 Discussion Unsteady Disturbance at the Inlet of Impeller

For the previous study of centrifugal pump with vaned diffuser, with the reduction of flow rare, recirculation would be found at the inlet of impeller by Peter Hergt et al (Murakami and Heya 1966, Breugelmans and Sen 1982, Barrand, Caignaert et al. 1984). With the further develop of the recirculation, cavitation is easy to occur.

For the test pump, similar frequency distribution has been found on the pressure monitor Suc39 on each leading edge of impeller near shroud. From Fig. 7.6, it could be deduced that there was a periodic disturbance with the frequency smaller than f_{IR} occurs at 0.584 Q_{DES}. By the pressure analysis in frequency domain, it indicated that there were five peaks (St around 1.1, 1.2, 1.3, 1.4 and 1.5) on the leading edge of impeller near shroud at 0.583Q_{Des} as shown in Fig. 7.7 (c).

By the high order analyses as shown in Fig. 7.13, it is indicated that the St around 1.2 is a non-linear frequency component in the leading edge near shroud. Calculated by Eq. (6-7), the absolute St Number for St≈1.2 is 0.1 (7Hz), the corresponding *m* is 9. And the conclusion was agreed with the conjecture from Fig. 7.6.

By the high order analyses as shown in Fig. 7.13, it is indicated that the St around 1.2 was a non-linear frequency component on the leading edge near shroud. Calculated by Eq. (6-7), the absolute St Number for St≈1.2 is 0.1 (7Hz), the corresponding *m* is 9. In addition, the conclusion was agreed with the conjecture from Fig. 7.6.

The intensity of dipole sources at St=1.2 on the impeller blade was showed in Fig. 7.14, the high acoustic pressure regions in this picture highlight the location of this unsteady disturbance. In this condition, on the leading edge of blade, the region impacted by this disturbance was not very large.

With the further reduction of the flow rate, the recirculation at the inlet of impeller would develop, the rotating cavitation may occur which would make a positive slop of *Q-H* curve (Tsujimoto, Kamijo et al. 1993, Hashimoto, Yoshida et al. 1997, Tsujimoto 2001, Friedrichs and Kosyna 2002, Franc, Rebattet et al. 2004, Iga, Nohml et al. 2004) . Meanwhile, in this case, the local dent is found in the *Q-H* curve around 0.4 Q_{Des} which is likely caused by the abrupt change in this flow pattern.

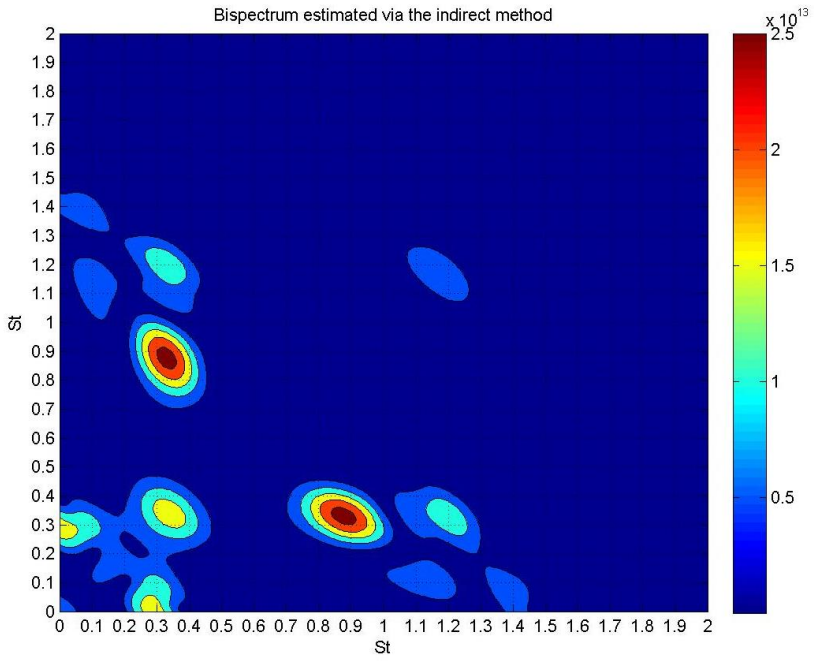

Fig. 7. 13 Pressure Bispectrum at leading edge of impeller blade (Point Suc 29) at 0.584 Q_{Des}

Fig. 7.14 Intensity of dipole sources at St=1.2 in impeller at 0.584 Q_{Des}

7. 2 Unsteady Disturbance in Return Channel

7.2.1 Contributions of Each Component to the Instability of *Q-H* Curve

By the comparison of *Q-H* curve of impeller and whole pump, it is found that the head of impeller was hardly impaired during this instability region (Fig. 7.15), although several kinds of unsteadiness occurred in the impeller bellow this critical flow rate 0.7 Q_{Des}. For the losses of return system as shown in Fig. 7.16, a positive slop appeared around 0.63 Q_{Des} which is before the turning point of the head of whole pump. Thus, in this saddle instability region, the head of the whole pump is likely to be greatly affected by the unsteadiness in the return system.

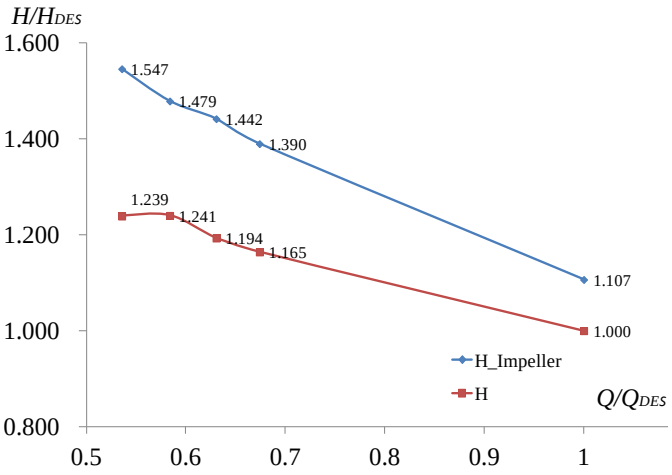

Fig. 7.15 Performance curve of test pump by simulation

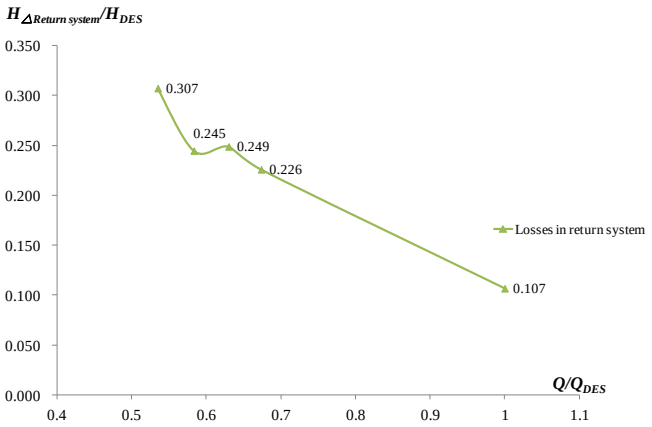

Fig. 7.16 Head losses in return system by simulation

The distributions of C_{pisdv} in the return system at $0.63Q_{Des}$ were presented in one impeller revolution in Fig. 7.17. It could be found that the most intense pressure fluctuation was at the inlet of the diffuser and near the shroud.

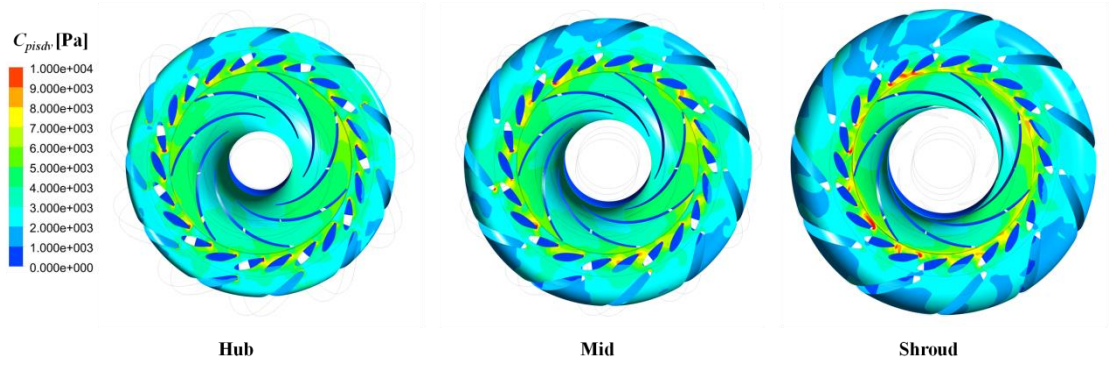

Fig. 7.17 Standard deviations of pressure in return system at 0.63 Q_{Des}

For the frequency analysis of pressure intensity, it is also found that the high pressure regions were mainly located at the inlet of the diffuser near shroud at the main peak frequencies (St=0.335, St=0.6625 and St=1). In addition, the intensity of pressure in return channel at these frequency is far smaller than that in diffuser as shown in Fig. 7.18.

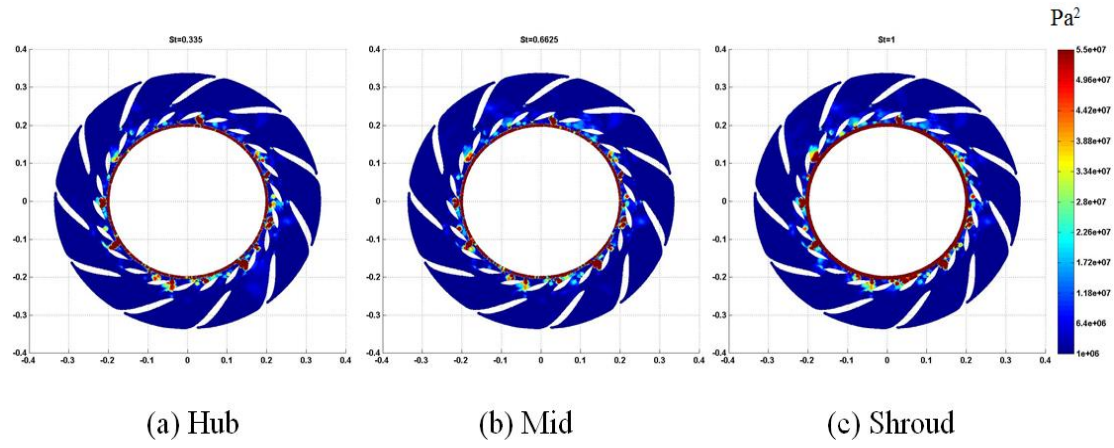

Fig. 7.18 Pressure distribution in return system shroud at St=0.335, St=0.6625 and St=1 at 0.583 Q_{Des}

Therefore, for the instability of *Q-H* curve during 0.45 to 0.7 Q_{Des}, the unsteadiness in diffuser especially at the inlet region of diffuser would play an important role. At the same time, due to its location, the flow in this component would be influenced by the disturbance both from upstream and downstream. As for the

disturbance from upstream, it is discussed in section 7.1 and the disturbance in return channel would be analyzed in this section.

7.2.2 Frequency Analysis of Pressure on the Cross Section at 0.583 Q_{Des}

In order to highlight the distribution of the pressure intensity at different non-linear frequencies in return channel. The colour bar of the pressure amplitude was amplified compared with Fig. 7.18, and the pressure distribution at St=0.335 and St=0.6625 were shown in Fig. 7.19 and 7.20, respectively. The locations of the high pressure regions were quite similar at these two frequencies at this condition. Compared with the corresponding pressure distribution at full load (Fig. 6.4), it could be found that the increase of pressure intensity at St=0.6625 was small, while the locations of the high pressure region are different.

For the full load, the high pressure regions at St=0.6625 mainly located on the suction side near the U shape corner, and was strongest near hub. But at 0.583 Q_{Des}, the location was closer to the diffuser. For the intensity of pressure, it was stronger near shroud than hub.

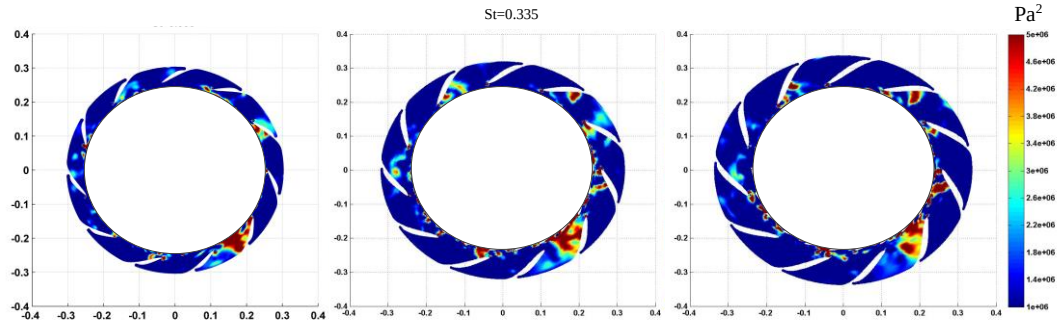

(a) Hub (b) Mid (c) Shroud

Fig. 7.19 Pressure distribution in return system on different crosswise at St=0.335 at 0.583 Q_{Des}

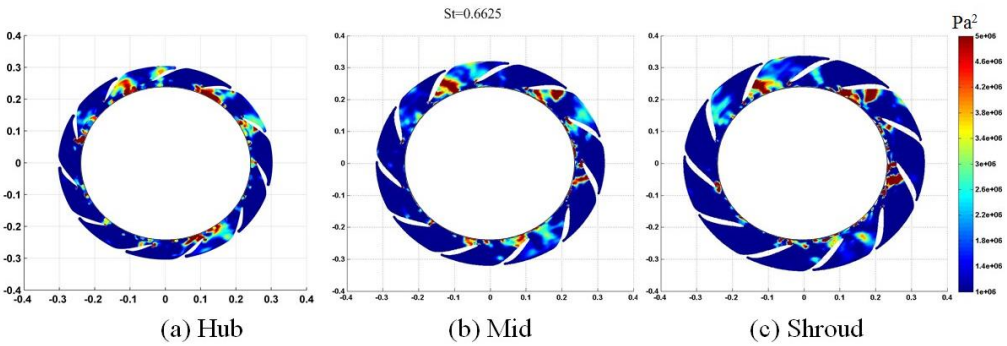

(a) Hub (b) Mid (c) Shroud

Fig. 7.20 Pressure distribution in return system on different crosswise at St=0.6625 at 0.583 Q_{Des}

7.2.3 Leakage between Adjusted Vane and Its Corresponding Stay Vane at 0.583 Q_{Des}

Since the high pressure regions at St=0.335 and 0.6625 were close to the leading edge of stay vane, it is deduced that the flow in the leakage between adjusted vane and the corresponding stay vane would be complex and may contains strong fluctuation of St=0.335 and 0.6625. The leakages of each channel were monitored, and its time wave was shown in Fig. 7.21. Due to the limitation of calculated impeller revolutions, it is difficult to find rotating characters in this time wave. But five cells were found in the peripheral direction of the gap of diffuser and return channel. In the frequency domain, obvious peaks could be found at St=0.335 and St=0.6625 in some channel on the frequency domain as shown in Fig 7.22.

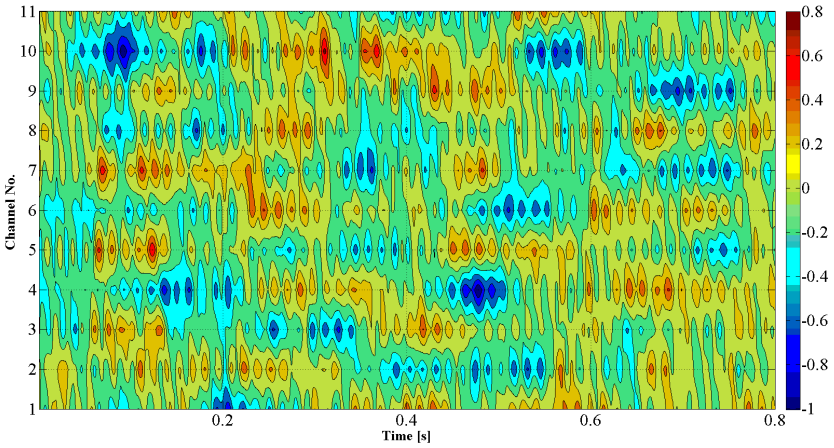

Fig. 7.21 Time wave of the instantaneous leakage of each diffuser channel to the adjacent return vane channel at 0.583 Q_{Des}

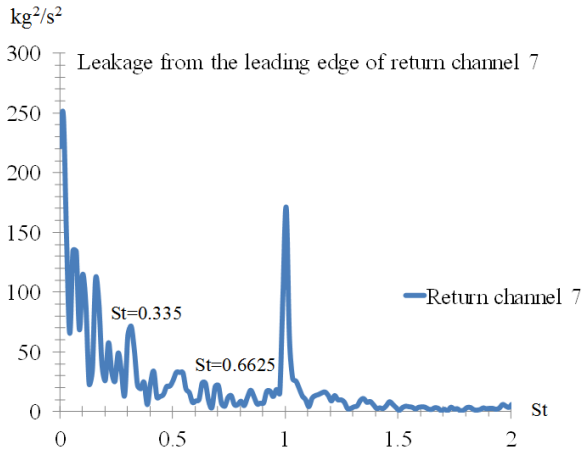

Fig. 7.22 Auto spectrum of leakage from return vane channel 7 at 0.583 Q_{Des}

7.3 Unsteady Disturbance in Diffuser

For the analysis in section 7.2.1, it revealed that the unsteadiness in the diffuser has a great influence on the saddle instability of *Q-H* curve during 0.45 to 0.7 Q_{Des}. Meanwhile, the experimental analysis indicated that the main non-linear frequency components in this unstable region were St=0.335 and 0.6625. The aim of this section is to study the role, which these two unsteady patterns play in the diffuser for the inception and the development of the instability of performance curve.

At full load condition, the unsteady pattern at St=0.6625 on the suction side of stay vane was detected both by experimental and simulation results. The previous experimental and numerical results indicate that this disturbance develops and moves towards to the leading edge of stay vane with the falling flow rate, especially bellow $0.7Q_{Des}$. This means that the fluid in diffuser are increasingly affected by the disturbance of St=0.6625 from return channel with the reduction of flow rate. Furthermore, the analysis in section 7.1 indicates that the flow separation, which occurs at the throat of impeller blade suction side, was periodic with the same frequency of this unsteady pattern.

Additionally, with the reduction of the flow rate, the wake-jet near the trailing edge of impeller blade became more severe and caused a periodic disturbance with St around 0.81 in the rotating frame (St=0.335 in the static frame). Thus, it could be deduced that the non-linear frequency St=0.335 in the diffuser may be caused by the wake-jet of the impeller. The further analysis of the unsteady disturbance in diffuser was conducted in this section.

7.3.1 Pressure Analysis in Diffuser at Part Load

Firstly, the fluid-dynamical unsteadiness in diffuser was highlighted by the time-frequency analysis both in the experimental and numerical data (Fig. 7.23 and 7.24). The wavelet transforms were featured by a quite constant value in time for the impeller passage frequency f_{IR} (St=0.143) and a pulsating values in time for the frequency at St=0.6625 and St=0.335 for all the transducers and monitors positioned in the diffuser blade. A possible explanation for the low BPF amplitude could be the existence of the unsteady pattern that determined a “natural” manipulation of the spectral content, lowering the BPF intensity (Tsujimoto 2001). Moreover, when the BPF was identifiable, it appears to be pulsating as well as the frequencies of the unsteady pattern.

In order to highlight the features of circumferential propagation, the cross-correlation analysis has been carried out for the monitor points on adjacent blade. Figure 7.25 shows the cross spectrum of between the monitor D03 on diffuser vane 6 and 7. Except the peaks at BPF, impeller passage frequency and its harmonic, the peaks at St=0.335 and 0.6625 were detected.

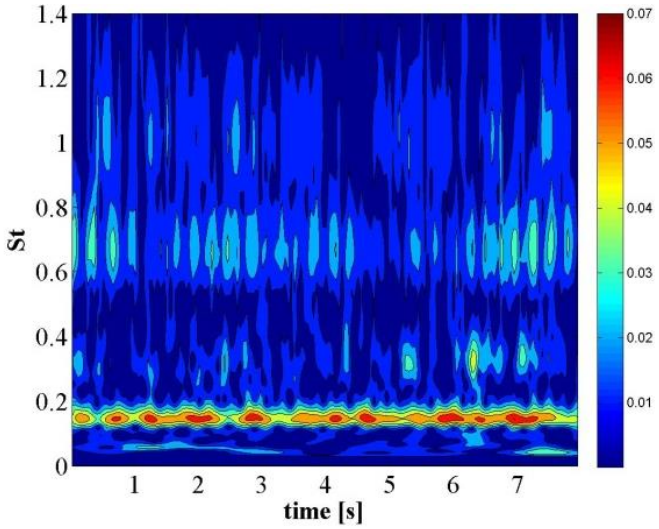

Fig. 7.23 Wavelet magnitude |Wn| of point 4 in the diffuser vane for 0.674 Q_{Des} by experiment

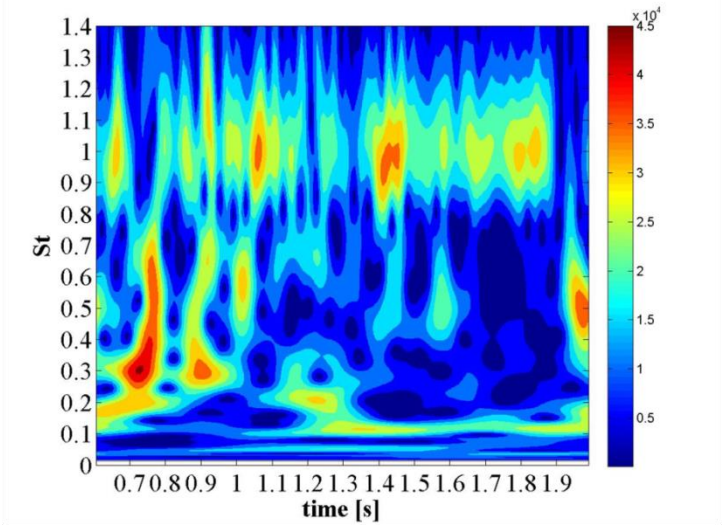

Fig. 7.24 Wavelet magnitude |Wn| of point 4 in the diffuser vane for 0.674 Q_{Des} by simulation

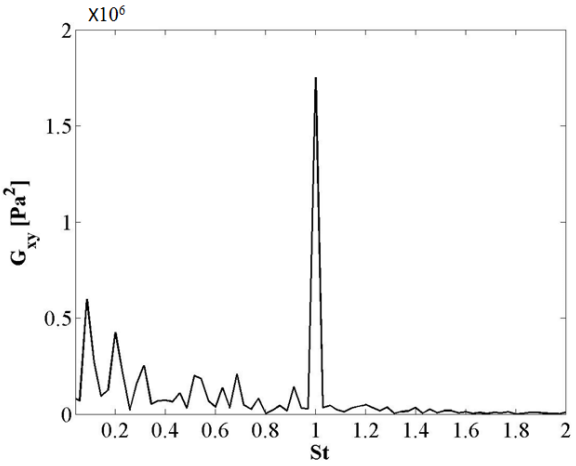

Fig. 7.25 Cross spectrum between P3 on blade 6 and blade 7

7.3.2 Analysis of Velocity in Diffuser at Part Load

At same time, at for 0.674 Q_{Des}, five distinct stall cells can be identified in the diffuser. The progression of a stall cell from one channel to the next was shown in Fig. 7.26. Figure 7.26 shows the separated flow in the channel between vane 1 and vane 2, which induced the stalled flow in the corresponding return channels.

Due to this stalled flow, the pressure in the area between vane 1 and 2 and the corresponding stay vanes rises. Additionally, the flow from the impeller circumvents the stalled vane channel, leading to higher flow velocities and thus lowers pressure in the neighbouring channels. This pressure rise leads to a secondary flow from this area to the neighbouring channel, showing lower pressure due to the higher flow velocity induced by the increased relative vane channel flow rates. In the following phases the flow around the trailing edge of the vanes 2 triggers a flow separation into channel

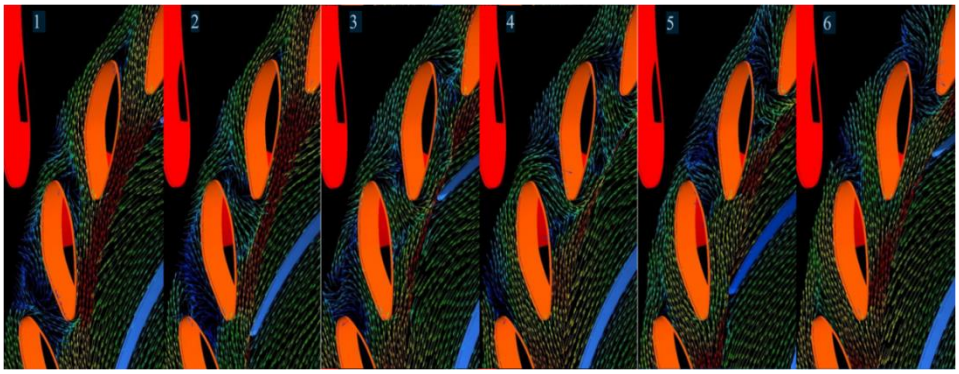

Fig. 7.26 Vector plot sequence in the diffuser channel closer to the shroud for 0.674 Q_{Des}

between vanes 2 and 3, causing the progression of the stall cell into the diffuser.

Meanwhile, in the gap of impeller and diffuser, small vortices are caught sometimes near the leading edge of stay vane pressure side on the cross section near the shroud (Fig. 7.27). With the falling flow rate, this kind of vortices develops, highly non-uniform velocity distribution prevails in the gap and the blockage became to appear.

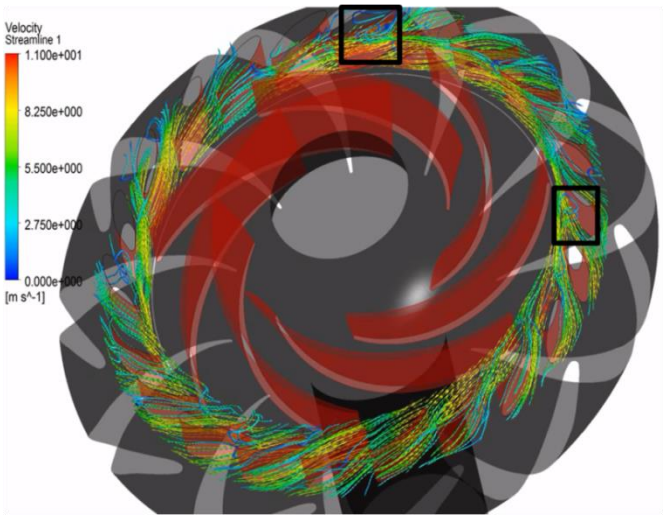

Fig. 7.27 Streamlines in diffuser at 0.674 Q_{Des}

An instantaneous state of the streamlines in diffuser at a certain moment was shown in Fig. 7.28. In this figure, it indicated that the distribution of velocity in the triangle area of the inlet of diffuser near shroud was more severe with the further falling flow rate from 0.674 to 0.583 Q_{Des}. Moreover, the blockage was found at gap between impeller and diffuser near the shroud at 0.583 Q_{Des}.

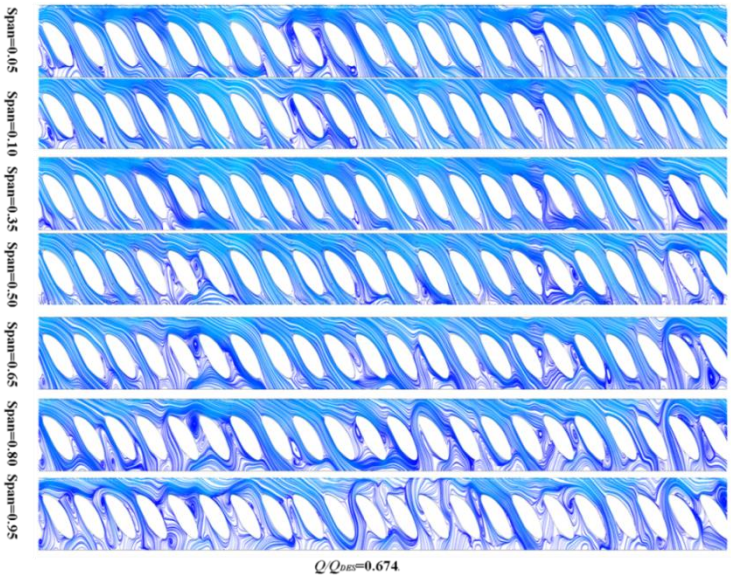

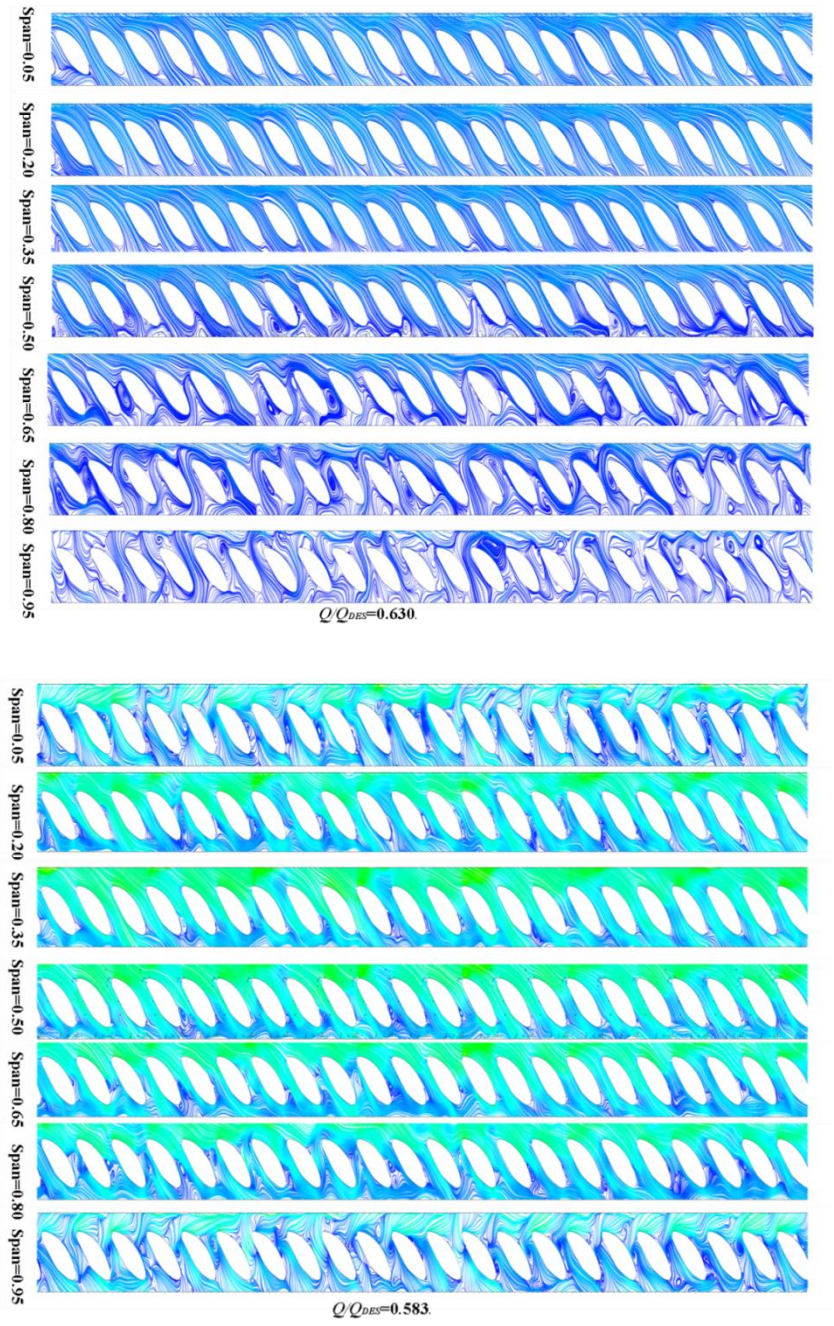

Fig. 7.28 Streamlines in diffuser at 0.674 Q_{Des}, 0.630 Q_{Des} and 0.583 Q_{Des}

The frequency analysis of the velocity in return system highlight the trend of the amplitude of velocity at St=0.335 and 0.6625 in diffuser which get by the experimental results (Fig. 29 and Fig.30). As shown in the pictures, for these two frequencies, it could be found that there were several high amplitude regions in the gap of impeller and diffuser near the hub. Closer to the shroud, these regions became to be smaller and some were disappeared near shroud where the blockage was severe.

Thus, it could concluded that the mixture by the disturbance with St=0.335 and 0.6625 would be increase of the amplitude at these two frequency firstly. However,

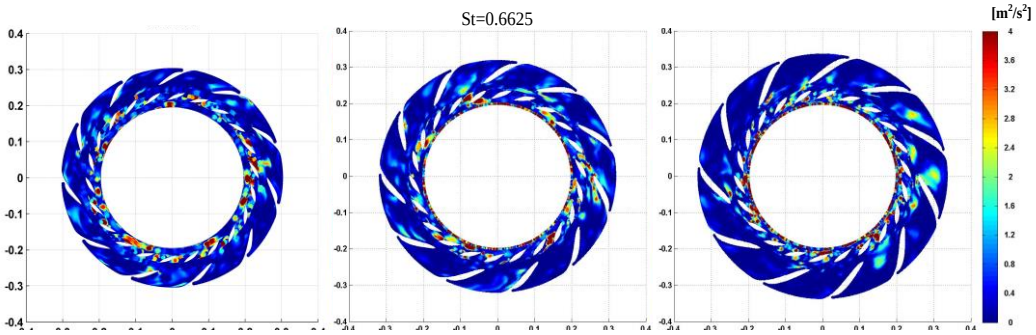

(a) Hub (b) Mid (c) Shroud

Fig. 7.29 Velocity distribution at St=0.6625 on different crosswise spans by simulation 0. 583 Q_{Des}

with the development of the mixture, it would cause blockage in some parts. In the region of blockage, the corresponding amplitudes did not increase but reduced. Meanwhile, it also resulted in the drop of the mean pressure at the exit of the impeller.

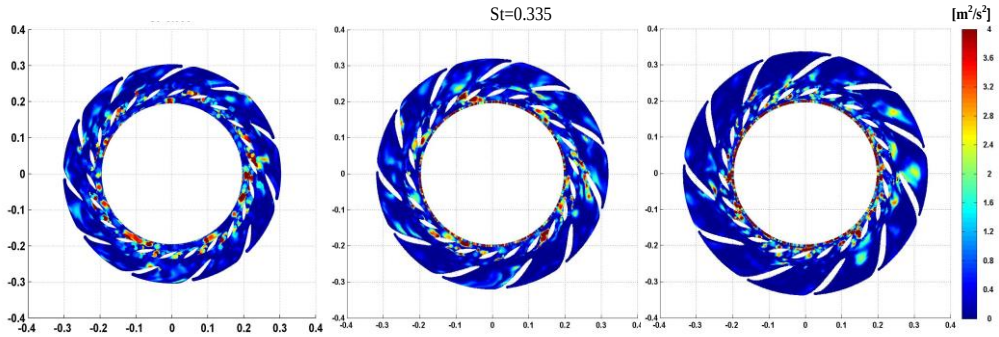

(a) Hub (b) Mid (c) Shroud

Fig. 7.30 Velocity distribution at St=0.335 on different crosswise spans by simulation 0. 583 Q_{Des}

7.3.3 Analysis on the Trend of Amplitude of Pressure at St=1

The pressure at the inlet of diffuser near the shroud was analyzed to highlight the impact of this blockage to pressure fluctuation. The monitor points were set at the middle of inlet of each diffuser vane channel near shroud. The cross-correlation analysis of the monitor points between adjacent vane channels was conducted. In some channels, an interesting result appears as shown in Fig 5.3. It presented the cross spectrum of the monitors in channel 8 and channel 9 at the flow rate of 0.630 Q_{Des} and 0.583 Q_{Des}. Compared with the cross spectrum at 0.630 Q_{Des}, all the amplitudes at impeller passage frequency, St=0.335 and 0.6625 reduce while the intensity of BPF (St=1) increases dramatically at 0.583 Q_{Des}.

Fig. 7.31 indicates the velocity plots near shroud, the flow field in the gap of the impeller and diffuser near shroud was quite uneven. The blockage in this area aggravated the rotor and stator interaction and caused the higher pressure amplitude at BPF. The pressure distributions at BPF validate this conclusion (Fig. 7.32).

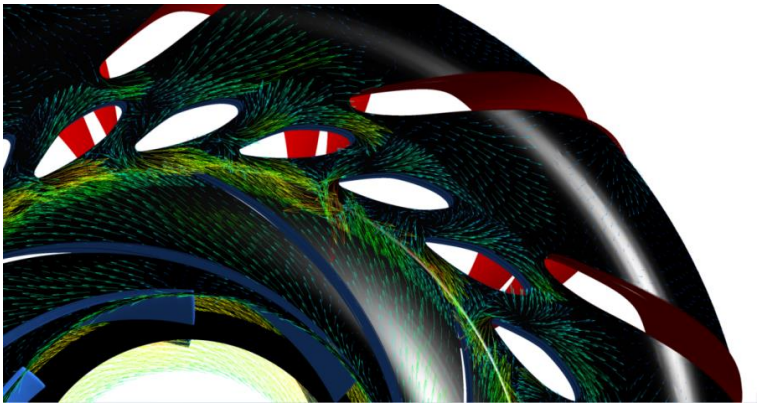

Fig. 7.31 Velocity plots near shroud at 0.583 Q_{Des}

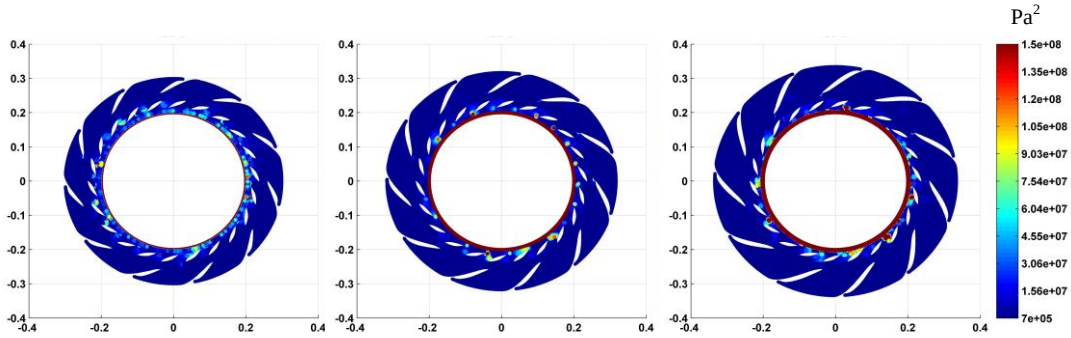

(a) Hub (b) Mid (c) Shroud

Fig. 7.32 Pressure distribution in return system on different crosswise at St=0.1 at 0.584 Q_{Des}

7.4 Conclusions

Through the above analysis, with the reduction of flow rate, the velocity and pressure distribution in impeller, diffuser and return channel were all gradually unstable. And the unsteady disturbances in these components during the saddle instability region 0.45-0.7 Q_{Des} were summarized as bellow.

1. For the impeller, with the falling of the flow rate, there were two main unsteady patterns, which were found near the critical point of 0.6Q_{Des}. The first one was the flow separation that occurs on the suction side of impeller blade. The location of this separation was near the throat of blade and strongest near shroud. It was a kind of periodic disturbance with the frequency at St around 0.335 in the rotating frame and the corresponding absolute St Number was 0.6625 with the mode m=7 in the

static frame. Furthermore, this characteristic frequency agrees with the frequency of the unsteady disturbance that was found in the return channel even at full load condition.

At the same time, the wake-jet pattern around the trailing edge of impeller blade also became more severe with reduction of flow rate. And by the frequency analysis, it indicated that it caused a periodic disturbance with frequency at St around 0.81 in the rotating frame and the corresponding absolute St Number was 0.335 with the mode m=8 in the static frame.

Furthermore, when the flow rate reduces to the critical flow rate of 0.6 Q_{Des}, a recirculation was found at the inlet of impeller near shroud and the frequency is 7Hz.

2. In the return channel, for the unsteady disturbance with St=0.6625, the increase of pressure intensity at St=0.6625 was weak with the reduction of flow rate, while the locations of the high pressure region were closer to the inlet of return channel along the suction side of stay vane. Meanwhile, for the intensity of this pressure, it was stronger near shroud than hub.

Except this disturbance, another disturbance with St=0.335 was found in the return channel, and the location and intensity was quite similar to St=0.6625.

3. In the diffuser, the flow field would be more complex due to the influence from the disturbance from impeller and diffuser. With the falling of flow rate, in diffuser there were local flow separations due to the reduction of flow rate. At the same time, by the frequency analysis, it is indicated that the flow in diffuser was also mainly impacted by the wake-jet of impeller (St=0.335) and the unsteady patterns (St=0.6625) from return channel.

The slop of *Q-H* curve in this saddle instability region was mainly caused by the unsteady flows at the inlet area of the diffuser. When the mode pump operated into the saddle instability region, two different flow separations were mixed in this region. Moreover, the mixture would be increase of the amplitude at St=0.335 and 0.6625 firstly. However, with the development of the mixture, it would cause blockage in most of the gap between impeller and diffuser near shroud at 0.583 Q_{Des}. This blockage would reduce the intensity at St=0.335 and 0.6625 and increase the intensity at BPF.

IV Conclusions

Chapter 8 Conclusions and Perspectives

8.1 Conclusions

For the variable requirements of energy production and consumption, a wide head range is desired for modern pump turbine operation. The reversible pump turbine at pump model could be seen as a centrifugal pump with vaned diffuser. In order to get a wider stable head range, the performance curve instabilities or sudden deviation from the expected smooth performance curves should be avoided.

In the present study, the analyzed pump-turbine is a low-pressure stage of a two stages pump-turbine on pump mode. On the performance curve of the test pump, a hump instability region has been detected bellow design flow rate. between 0.45 to 0.70 Q_{Des}, Whereas below 0.40 Q_{Des} the head increases due to the effect of fully developed inlet recirculation. The stable operation range of the pump is restricted by the saddle instability between 0.45 to 0.70 Q_{Des}. The aim of this investigation was to analyze the characteristics instabilities during the saddle instability region (0.45 to 0.70 Q_{Des}), study the development of the unsteady phenomena, and find the causes of this instability region which could guide the design and optimize the pump.

An Open Turbomachinery Facility (OTF) has been improved to conduct the experimental research about the unsteady flow in the test pump. A program has been written to realize the function of pressure data acquisition and post-analysis based on Labview and Matlab. In this study, the characteristics of dynamic pressure signals in frequency domain and time-frequency domain have been analyzed combined with the higher order spectral analysis method to diagnose the type of the unsteady structure in centrifugal pump with vaned diffuser.

In order to analyze and describe the movement in flow passage between vanes in diffuser and return channel qualitatively, high-speed flow visualization has been performed using Photron FASTCAM PCI digital camera.

In this research, numerical simulation has been carried out both on the flow field and the relative acoustics field. The effect of leakage flow on the fluid flow would not be considered to be negligible in this research. Meanwhile, a leakage system was used to model the leakage inner pump. The distribution of the velocity at the boundary of leakage was set as a boundary condition in the flow field simulation by ANSYS-CFX. The intensity of dipole sources caused by the surface pressure has been predicted by a hybrid method through the ANSYS-CFX and LMS Virtual. Lab Acoustics.

It is found that the leakage system adopted to model the effect of leakage flow in pump was of a reasonable performance. Thus, the simulation of the flow field in this research could be used as some reliable results to help understand the features of the flow in pump at different flow rates. In this study some conclusions from the comparison between experimental and numerical calculation were listed as below.

1. At full load condition:

Through the above analysis, the unsteady flow at full load, which occurs in return channel, includes several periodic fluctuations. Both the forced fluctuation caused by impeller rotating (such as BPF) and the unforced fluctuation at St=0.6625 were obvious. At the same time, some obvious rotating propagation characters were found at frequency St=0.042, St=0.085 and BPF. And the intensity of these unsteady patterns mainly presents to be strongest near hub.

Although several periodic unsteadiness were found at full load, based on the acoustic analysis in diffuser and return channel, it is found that the intensity of dipole sources at BPF plays a critical role in the contribution of the dipole sources at full load.

2. At part load instability region:

With the flow rate falling into the saddle instability region, several types of unsteady flow were found in impeller, diffuser and return channel. And they were summarized as bellow:

In the impeller, two main different flow patterns were found in this flow rate interval. One is the flow separation occurred on the suction side of impeller blade and its location was near the throat of blade and strongest near shroud. It was a kind of periodic disturbance with the frequency at St 0.6625 which agree with the frequency of the unsteady disturbance found in the return channel even at full load condition. The other one was wake-jet of impeller with frequency at St 0.335. Furthermore, when the flow rate reduces to the critical flow rate 0.6 Q_{Des}, recirculation with frequency 7 Hz has been found at the inlet of impeller near shroud.

It is indicated that these disturbances hardly impaired the head of the impeller, but exacerbated the uneven distribution of velocity in the inlet triangle region of diffuser. It plays a remarkable role in the trend of head losses in diffuser.

At the same time, in the return channel, the unsteady disturbance with St=0.6625 still exist, but the growth of pressure intensity of this disturbance was weak with the reduction of flow rate, while the locations of this disturbance were closer to the inlet of return channel along the suction side of stay vane. Meanwhile, for the intensity of this pressure, it was stronger near shroud than hub. And the periodic

unforced unsteadiness at St=0.6625 from return channel also impacted the fluid in diffuser dramatically on this saddle instability of *Q-H* curve. Except this disturbance, another disturbance with St=0.335 has been found in the return channel and its location and intensity were quite similar to St=0.6625.

In diffuser, there were local flow separations due to the reduction of flow rate. At the same time, by the frequency analysis, it is indicated that the flow in diffuser also was markedly impacted by the wake-jet of impeller (St=0.335) and the unsteady patterns (St=0.6625) from return channel. By the experimental results, it has been found that these two frequencies ware the main non-linear frequency component of the unsteady disturbances in diffuser. Meanwhile, the disturbances at these frequencies propagate circumferentially. The one at St=0.6625 has 5 cells which could be found in diffuser at full load and most part load conditions. The other one at St=0.335 has 2 cells and this disturbance only appeared in the first part of the saddle instability region from 0.6 to 0.7 Q_{Des}.

By numerical results, it is indicated that, in diffuser, with reducing of flow rate, two kinds of unsteady patterns at frequency St=0.6625 and St=0.335 mixed in the inlet triangle region of diffuser and caused a blockage at the gap between impeller and diffuser near shroud. At the beginning of this instability region, the recirculation at inlet of diffuser is the exchange of momentum, which means that the head increases. While with the further development of the mixed flow, the interaction of the fluctuation at St=0.6625 and St=0.335 became more severe and lead to more energy loss. That is the reason for the pressure amplitude drop at these two frequencies at 0.584 Q_{Des}. By analogy, the energy loss would increase and bring about the drop of head during the fully development of blockage at the gap. This can explain why the positive slope of *Q-H* curve appears around 0.6 Q_{Des}. Meanwhile, the blockage caused by the mixed flow could be the reason for the drop of the mean variation pressure at the outlet of impeller.

8.2 Perspectives

The research, which has been started in this work, does not finish here. Some aspects have to be studied in-depth, and more other consideration have to be taken into account in the further study.

1. As regards the unsteadiness identified in the diffuser that significantly affected the *Q-H* curve, the techniques for reducing their intensity need to be developed in the future work. Since the unsteadiness mainly impacted by the disturbance at St=0.335 which is caused by the wake-jet of impeller and the other disturbance at St=0.6625

from the return channel, the future research could proceed in two directions to improve these unsteady patterns in the impeller or the return channel.

2. For the experimental investigation, the high-speed visualization in this research was only applied in a quantitative analysis, and the post processing method need to be improved, in order to apply more useful information for the quantitative analysis in the next step.

3. Meanwhile, due to the detection of recirculation at the inlet of the impeller, the development of this recirculation should be studied with the further reducing of the flow rate in the next step both by experimental and numerical study. It would play an important role for the second saddle instability region on the *Q-H* curve.

4. The unsteadiness inner pumps at part load, which we are focused on, changes with the time and maybe develops with the time, due to the limitation in the computing time, resource and model, some features of the unsteadiness were not captured in this study such as the propagation at circumferential direction at St=0.335 and 0.6625. More work need to be done in the future to improve this problem.

5. Last but not the least, the research on the flow-induced noise caused by the unsteadiness was in the beginning. Only the intensity of dipole sources has been considered in this study. With the development of the unsteady flow, more attention should be placed on the effect of the monopole sources and the quadrupole sources.

References

(Mar 3rd 2012). "Energy storage-packing some power." from http://www.economist.com/node/21548495?frsc=dg%7Ca.

Acosta, A. (1958). An experimental study of cavitating inducer. Proceedings of the Second Symposium on Naval Hydrodynamics, 1958.

Akin, O. and D. Rockwell (1994). "Actively controlled radial flow pumping system: manipulation of spectral content of wakes and wake-blade interactions." Journal of Fluids Engineering **116**(3): 528-537.

Barrand, J., et al. (1984). Experimental determination of the reverse flow onset in a centrifugal impeller. Proceedings of the First International Pump Symposium. Texas A&M University.

Bartlett, M. S. (1948). "Smoothing periodograms from time series with continuous spectra." Nature **161**(4096): 686-687.

Bartlett, M. S. (1950). "Periodogram analysis and continuous spectra." Biometrika: 1-16.

Breugelmans, F. and M. Sen (1982). Prerotation and fluid recirculation in the suction pipe of centrifugal pumps. Proc. 11th Int. Pump Symp., Texas A&M Univ.

Cavazzini, G. (2006). Experimental and numerical investigation of the rotor-stator interaction in radial turbomachines, University of Padua. **Doctor Thesis**.

Cavazzini, G. (2013). Rotor-Stator Interaction in Radial Turbomachines, LAP Lambert Academic Publishing.

Cavazzini, G., et al. (2009). "Analysis of the rotor-stator interaction in a radial flow pump." La Houille Blanche(5): 141-151.

Choi, J.-S., et al. (2003). "Experiments on the unsteady flow field and noise generation in a centrifugal pump impeller." Journal of Sound and Vibration **263**(3): 493-514.

Commission, I. E. (1991). Field acceptance tests to determine the hudraulic performance of hydraulic turbines, storage pumps and pump-turbines, International Electrotechnical Commission.

Commission, I. E. (1999). "IEC 60193. Hydraulic turbines, storage pumps and pump-turbines—model acceptance tests." Chap. Dimensional Check of Model and Prototype.

D, F. K. a. T. (1932). "Investigation of the flow conditions in a centrifugal pump." Trans. ASME, Hydraulics **54**: 141-155

Dürrer, B., et al. (2006). Noise Sources In Centrifugal Pumps. Proceedings of the 2nd WSEAS Int. Conference on Applied and Theoretical Mechanics, Venice, Italy.

Dussourd, J. L. (1968). "An investigation of pulsations in the boiler feed system of a central power station." Journal of Fluids Engineering **90**(4): 607-616.

Engelberg, S. (2008). Digital Signal Processing: An Experimental Approach, Springer.

Farge, M. (1992). "Wavelet transforms and their applications to turbulence." Annual Review of Fluid Mechanics **24**(1): 395-458.

Feng, J., et al. (2009). "Unsteady flow visualization at part-load conditions of a radial diffuser pump: by PIV and CFD." Journal of Visualization **12**(1): 65-72.

Feng, J., et al. (2010). "Application of different turbulence models in unsteady flow simulations of a radial diffuser pump." Forschung im Ingenieurwesen **74**(3): 123-133.

Feng, J., et al. (2011). "Investigation of periodically unsteady flow in a radial pump by CFD simulations and LDV measurements." Journal of Turbomachinery **133**(1): 011004.

Fernández Oro, J. M., et al. (2009). "Forced and unforced unsteadiness in an axial turbomachine." Experimental Thermal and Fluid Science **33**(3): 449-459.

Ferrara, G., et al. (2004). "Rotating stall in centrifugal compressor vaneless diffuser: experimental analysis of geometrical parameters influence on phenomenon evolution." International Journal of Rotating Machinery **10**(6): 433-442.

Franc, J.-P., et al. (2004). "An experimental investigation of thermal effects in a cavitating inducer." Journal of Fluids Engineering **126**(5): 716-723.

Friedrichs, J. and G. n. Kosyna (2002). "Rotating cavitation in a centrifugal pump impeller of low specific speed." Journal of fluids engineering **124**(2): 356-362.

Gülich, J. F. (2010). Centrifugal Pumps, Springer.

González, J., et al. (2002). "Numerical simulation of the dynamic effects due to impeller-volute interaction in a centrifugal pump." Journal of Fluids Engineering **124**(2): 348-355.

Guo, S. and Y. Maruta (2005). "Experimental investigations on pressure fluctuations and vibration of the impeller in a centrifugal pump with vaned diffusers." JSME International Journal Series B **48**(1): 136-143.

Hashimoto, T., et al. (1997). "Experimental study on rotating cavitation of rocket propellant pump inducers." Journal of Propulsion and Power **13**(4): 488-494.

Hasmatuchi, V., et al. (2011). Hydrodynamics of a Pump-Turbine at Off-Design Operating Conditions: Numerical Simulation. ASME-JSME-KSME 2011 Joint Fluids Engineering Conference, American Society of Mechanical Engineers.

Hergt, P. and J. Starke (1985). Flow patterns causing instabilities in the performance curves of centrifugal pumps with vaned diffusers. Proceedings of the Second International Pump Symposium.

Hong, S.-S. and S.-H. Kang (2004). "Flow at the centrifugal pump impeller exit with circumferential distortion of the outlet static pressure." Journal of Fluids Engineering **126**(1): 81-86.

Horodko, L. (2006). "Identification of rotating pressure waves in a centrifugal compressor diffuser by means of the wavelet cross-correlation." International Journal of Wavelets, Multiresolution and Information Processing **4**(02): 373-382.

Horodko, L. (2007). Detection of surge precursors in a centrifugal compressor with a wavelet method. Proceedings of the 7th European Conference on Turbomachinery, Fluid Dynamics and Thermodynamics.

Iga, Y., et al. (2004). "Numerical analysis of cavitation instabilities arising in the three-blade cascade." Journal of Fluids Engineering **126**(3): 419-429.

Iino, M., et al. (2003). Numerical Simulation of Hysteresis on Head/Discharge Characteristics of a Centrifugal Pump. ASME/JSME 2003 4th Joint Fluids Summer Engineering Conference, American Society of Mechanical Engineers.

Ishii, Y. (1962). The Two Types of Runaway States of Propeller Turbine under Cavitation. Proceedings of IAHR Symposium, Sendai, Paper No. B-5.

Jacob, T. (2013). Pumped storage in Switzerland-an outlook beyond 2000.

Jeon, W.-H. (2003). "A numerical study on the effects of design parameters on the performance and noise of a centrifugal fan." Journal of Sound and Vibration **265**(1): 221-230.

Johnston, J. and R. Dean (1966). "Losses in vaneless diffusers of centrifugal compressors and pumps: analysis, experiment, and design." Journal of Engineering for Gas Turbines and Power **88**(1): 49-60.

Kotapati-Apparao, R. B., et al. (2003). "Prediction of a prolate spheroid undergoing a pitchup maneuver." AIAA paper **269**: 2003.

Kotapati-Apparao, R. B., et al. (2004). "Prediction of the Flow over an Airfoil at Maximum Lift." AIAA paper **259**: 2004.

Langthjem, M. and N. Olhoff (2004). "A numerical study of flow-induced noise in a two-dimensional centrifugal pump. Part I. Hydrodynamics." Journal of Fluids and Structures **19**(3): 349-368.

Langthjem, M. and N. Olhoff (2004). "A numerical study of flow-induced noise in a two-dimensional centrifugal pump. Part II. Hydroacoustics." Journal of Fluids and Structures **19**(3): 369-386.

Launder, B. E. and D. Spalding (1974). "The numerical computation of turbulent flows." Computer Methods in Applied Mechanics and Engineering **3**(2): 269-289.

Layton, W. and A. Novotný (2010). On Lighthill's acoustic analogy for low Mach number flows. New Directions in Mathematical Fluid Mechanics, Springer**:** 247-279.

Lee, S., et al. (2010). "Prediction and reduction of internal blade-passing frequency noise of the centrifugal fan in a refrigerator." International Journal of Refrigeration **33**(6): 1129-1141.

Levine, J. G. (2007). Pumped Hydroelectric Energy Storage and Spatial Diversity of Wind Resources as Methods of Improving Utilization of Renewable Energy Sources, ProQuest.

Li, Y., et al. (2010). "Experimental and numerical studies on the discrete noise about the cross-flow fan with block-shifted impellers." Applied Acoustics **71**(12): 1142-1155.

Lucius, A. and G. Brenner (2010). "Unsteady CFD simulations of a pump in part load conditions using scale-adaptive simulation." International Journal of Heat and Fluid Flow **31**(6): 1113-1118.

Lucius, A. and G. Brenner (2011). "Numerical simulation and evaluation of velocity fluctuations during rotating stall of a centrifugal pump." Journal of Fluids Engineering **133**(8): 081102.

Majidi, K. (2004). Numerical Study Of Unsteady Flow in A Centrifugal Pump. In ASME Turbo Expo 2004: Power for Land, Sea, and Air. 805-814.

Mitchell, D. P. and A. N. Netravali (1988). Reconstruction Filters in Computer-Graphics. ACM Siggraph Computer Graphics, ACM.

Murakami, M. and Heya N. (1966). "Swirling flow in suction pipe of centrifugal pumps: 1st report, distribution of velocity and energy." Bulletin of JSME **9**(34): 328-337.

Patankar, S. (1980). Numerical heat transfer and fluid flow, CRC Press.

Pavesi, G., et al. (2008). "Time-frequency characterization of rotating instabilities in a centrifugal pump with a vaned diffuser." International Journal of Rotating Machinery **2008**.

Pavesi, G., et al. (2008). "Time–frequency characterization of the unsteady phenomena in a centrifugal pump." International Journal of Heat and Fluid Flow **29**(5): 1527-1540.

Pavesi, G., et al. (2011). Experimental and numerical investigation of unforced unsteadiness in a vaneless radial diffuser. 9th European Conference on Turbomachinery-Fluid Dynamics and Thermodynamics.

Pedersen, N., et al. (2003). "Flow in a centrifugal pump impeller at design and off-design conditions—part I: particle image velocimetry (PIV) and laser Doppler velocimetry (LDV) measurements." Journal of Fluids Engineering **125**(1): 61-72.

Pei, J., et al. (2012). "Investigation of unsteady flow-induced impeller oscillations of a single-blade pump under off-design conditions." Journal of Fluids and Structures **35**: 89-104.

Pei, J., et al. (2012). "Numerical prediction of unsteady pressure field within the whole flow passage of a radial single-blade pump." Journal of Fluids Engineering **134**(10): 101103.

Pei, J., et al. (2013). "Fluid-structure coupling effects on periodically transient flow of a single-blade sewage centrifugal pump." Journal of Mechanical Science and Technology **27**(7): 2015-2023.

PTC19, A. (2004). 5-2004, Flow Measurement, New York: ASMg.

Reynolds, O. (1895). "On the dynamical theory of incompressible viscous fluids and the determination of the criterion." Philosophical Transactions of the Royal Society of London. A: 123-164.

Rodriguez, C., et al. (2007). "Frequencies in the vibration induced by the rotor stator interaction in a centrifugal pump turbine." Journal of Fluids Engineering **129**(11): 1428-1435.

Rzentkowski, G. and S. Zbroja (2000). "Experimental characterization of centrifugal pumps as an acoustic source at the blade-passing frequency." Journal of Fluids and Structures **14**(4): 529-558.

Sano, T., et al. (2000). "'Alternate Blade Stall and Rotating Stall in Vaned Diffuser-Part1: Effects of Impeller/Diffuser Clearance." Japanese, Trans. Jpn. Soc. Mech. Eng., Ser. B **66**: 650.

Sano, T., et al. (2002). "Alternate blade stall and rotating stall in a vaned diffuser." JSME International Journal Series B **45**(4): 810-819.

Sen, M. (1978). "Prerotation in centrifugal pumps." Off-Design Performance of Pumps **1**.

Sigl, J. C. and N. G. Chamoun (1994). "An introduction to bispectral analysis for the electroencephalogram." Journal of clinical monitoring **10**(6): 392-404.

Sinha, M., et al. (2001). "The flow structure during onset and developed states of rotating stall within a vaned diffuser of a centrifugal pump." Journal of Fluids Engineering **123**(3): 490-499.

Sturge, D. and N. Cumpsty (1975). "Two-dimensional method for calculating separated flow in a centrifugal impeller." Journal of Fluids Engineering **97**(4): 581-591.

Timushev, S. (2009). Development and experimental validation of 3D acoustic-vortex numerical procedure for centrifugal pump noise prediction. ASME 2009 Fluids Engineering Division Summer Meeting, American Society of Mechanical Engineers.

Torrence, C. and G. P. Compo (1998). "A practical guide to wavelet analysis." Bulletin of the American Meteorological society **79**(1): 61-78.

Tsujimoto, Y. (2001). "Simple rules for cavitation instabilities in turbomachinery." http://resolver. caltech. edu/cav2001: lecture. 006.

Tsujimoto, Y., et al. (1993). "A theoretical analysis of rotating cavitation in inducers." Journal of Fluids Engineering **115**(1): 135-141.

Wei, Z., et al. (2010). "Numerical simulation of flow in centrifugal pump impeller at off-design conditions [J]." Journal of Drainage and Irrigation Machinery Engineering **1**: 007.

Weik, M. H. (1998). "Communications Standard Dictionary."

White, F. M. (1979). Fluid mechanics, 1994, McGraw-Hill Inc.

Williams, J. F. and D. L. Hawkings (1969). "Sound generation by turbulence and surfaces in arbitrary motion." Philosophical Transactions of the Royal Society of London. Series A, Mathematical and Physical Sciences **264**(1151): 321-342.

Wuibaut, G., et al. (2002). "PIV measurements in the impeller and the vaneless diffuser of a radial flow pump in design and off-design operating conditions." Journal of Fluids Engineering **124**(3): 791-797.

Yang, C.-J. (2012). "Pumped hydroelectric storage." acedido a **20**.

Yang, J., et al. (2013). Numerical characterization of pressure instabilities in a vaned centrifugal pump under partload condition. IOP Conference Series: Materials Science and Engineering, IOP Publishing.

Yang, J., et al. (2014). "Numerical and experimental study on flow-induced noise at blade-passing frequency in centrifugal pumps." Chinese Journal of Mechanical Engineering **27**(3): 606-614.

Zhang, Z. (2010). Rotating stall mechanism and stability control in the pump flows. IOP Conference Series: Earth and Environmental Science, IOP Publishing.

He Y., et al.(2006). "Peak-load regulation and emergency function of weekly adjusted pumped storge station in beijing-tangshan power gird".Power System Technology(19): p. 71-75. (in Chinese)

Yang J., et al.(2001) ."A Model and Arithmetic for the Planning of Pumped-Storage Power Plant". Proceedings of the CSEE(02): 34-37+42. (in Chinese)

Acknowledgements

I would like to express my gratitude to all people who helped me during the writing of this thesis.

My deepest gratitude goes first and foremost to Prof. Giorgio Pavesi and Prof. Shouqi Yuan, my supervisors, for their constant encouragement and guidance. Without their consistent and illuminating instruction, this thesis could not have reached its present form. Professor Giorgio Pavesi not only gives me valuable advices about my Ph.D. study, but also gives me great help during my stay in Padua. At the same time, I am greatly indebted to Prof. Shouqi Yuan's instructive advice both on the research and further work.

Second, I would like to express my heartfelt gratitude to the colleges in the Department of Industrial Engineering of University of Padua in Italy and National Research Center of Pumps of Jiangsu University, China: Prof. Giovanna Cavazzini and JianpingYuan, Doctor Ji Pei, Yin Luo and Jingfeng Zhang, Alberto Benato and Giovanni Venturelli and the other colleges who once offered me valuable courses and advice. I also owe a special debt of gratitude to my friends who I met in both China and Italy.

I would finally like to express my deep gratitude to my beloved parents Mr. Linhai Yang and Mrs. Qinping Jiang, and my boyfriend Dr. Xiaohua Liu, who have always been helping me out of difficulties and supporting me without a word of complaint. I love you. You are the sunshine in my life.

Jun YANG

Feb. 4th, 2015

Biography

Jun YANG

National Research Center of Pumps - Jiangsu University
Xuefu Road 301 - Zhenjiang 212013 – Jiangsu – China
Tel: +86 13852942027
E-mial: jyang.tcpr@gmail.com

Education

2012.10-2015.3 University of Padua, Italy
Department of Industrial Engineering
Doctoral of Energetic (2015/3 graduate)
Double degree with Jiangsu University

2011.9-2014.12 Jiangsu University, China
National Research Center of Pumps
Doctor of Fluid Machinery Engineering (2014/12 graduate)

Doctoral thesis: Flow Patterns Causing Saddle Instablilty in the Performance Curve of a Centrifugal Pump with Vaned Diffuser

2008.9-2011.7 Jiangsu University, China
Research Center of Fluid Machinery Engineering and Technology
Master of Fluid Machinery Engineering (2011/07 graduate)
Master thesis: Numerical Research on the Inner Flow-Induced Noise for Centrifugal Pumps and Its Acoustic Optimization

2004.9-2008.7 **Beijing University of Aeronautic and Astronautic , China**
Department of Energy and Power Engineering
Bachelor of Engineering (2008/07 graduate)
Bachelor thesis: The Numerical Study of Counter-Rotating Fan

Languages

Chinese Native speaker
English Fluent (IELTS 6, CET 6)

Skills and qualifications

Microsoft Office, Originlab, Sigmaplot
ANSYS-CFX, LMS Virtual. Lab Acoustics, Auto CAD, Por/Engineer
Matlab, LabView

The project joined

1. "Cavitation characteristics of hydraulic machinery", State Key Program of National Natural Science Foundation of China (Grant No. 51239005)
2. "Investigations on key energy saving techniques of centrifugal pumps", National Outstanding Young Scientists Founds of China (Grant No. 50825902)
3. "Investigations on key technology of centrifugal pumps with million kilowatts nuclear power", National Science & Technology Pillar Program of China (Grant No. 2011BAF14B04)
4. "Investigations on the mechanism of vibration and noise induced by unsteady flow within centrifugal pump", National Natural Science Foundation of China (Grant No. 50979034)
5. "Investigations on hydraulic vibration characteristics in centrifugal pumps based on cavitating fluid-structure interaction", National Natural Science Foundation of China (Grant No. 51409123)
6. "Investigations on unstable fluid-structure interaction and vibration behavior of centrifugal pumps based on moving boundary LES method", Natural Science Foundation of Jiangsu Province (Grant No. BK20140554)
7. "Research on the rotating stall and the relative flow induced noise within centrifugal pump", Jiangsu Provincial Project for Innovative Postgraduate of China (Grant No. CXZZ13-0673)
8. Project of the University of Padova (Grant No. NCPDA 130025/13).

International conference participated

1. 2009/10 Participated in the 16th Tri-University International Joint Seminar & Symposium 2009 in Mie University, Japan, Reporter
2. 2010/10 Participated in 2010 International Conference on Pumps and Fans in Hangzhou, China, Reporter
3. 2013/9 Participated in the 6th International Conference of Pumps and Fans, Beijing, China, Reporter

Publications

1. **Yang Jun**, Pavesi Giorgio, Cavazzini Giovanna, et al. Experimental characterization of pump-turbine as pump mode at saddle instabilities region[J], ASME Journal of Fluid Engineering, 2015. (SCI)
2. **Yang Jun**, Yuan Shouqi, Yuan Jianping, et al. Numerical and experimental study on flow-induced noise at blade-passing frequency in centrifugal pumps[J], Chinese Journal of Mechanical Engineering, 2014, 27(3): 606-614. (SCI)
3. Yuan Shouqi, **Yang Jun**, Yuan Jianping, et al. Experimental investigation on the flow-induced noise under variable conditions for centrifugal pumps[J], Chinese Journal of Mechanical Engineering, 2012, 25(3): 456-462. (SCI)
4. **Yang Jun**, Yuan Shouqi, Yuan Jianping, et al. The optimization of flow-induced noise under BPF by changing the impeller diameter[C], ASME 2012 Fluids Engineering Division Summer Meeting, July 8-12, 2012, Puerto Rico, USA.
5. **Yang Jun**, Pavesi Giorgio, Cavazzini Giovanna, et al. Numerical characterization of pressure instabilities in a vaned centrifugal pump under partload condition[C], IOP Conference Series: Materials Science and Engineering. IOP Publishing, 2013, 52(2): 022044. (EI)
6. Pavesi Giorgio, **Yang Jun**, Cavazzini Giovanna, et al. Experimental analysis of instability phenomena in a high-head reversible pump-turbine at large partial flow condition[C], accepted to 11th European Turbomachinery Conference, Mar. 23-26, 2015, Madrid, Spain.(EI)
7. **Yang Jun**, Yuan Shouqi, Pei Ji, et al. Overview of rotating stall in centrifugal pump with vaned diffuser [J]. Accepted by Journal of Drainage and Irrigation Machinery Engineering.

Awards and grants

GRUNDFOS-Jiangsu University Innovation Contest, Brass Medal, (2010)
Merit Student –Jiangsu University (2010 and 2011)
Model Student of Academic Records–Jiangsu University (2010 and 2011)
State Scholarship Funded by China Scholarship Council, (2012)